

ABSTRACT

WANG, JIYU. Load Modeling and Control for Providing Grid Services in Distribution System. (Under the direction of Dr. Ning Lu).

Quasi-Static Time-Series (QSTS) power flow simulations have been widely used for feeder modeling in power distribution system planning studies in recent years. A critical step in a QSTS simulation is the selection of nodal load profiles. Researchers have been used one load shape scaling method to model the load profiles so that all the load shapes are same as the feeder load profile. However, in real life each load node will have its unique shape because of different user patterns. In recent years, utilities started to collect end users' smart meter data. This data provides researchers to model the distribution system down to building-level as well as generate a unique load shape for each load node.

With the detailed modeling of distribution system, one available area is to study how to improve the system operation from building-level. Buildings with inherent ability to store head in thermal mass has proved it has the potential to provide grid services. Compared to a residential house, commercial buildings have much larger floor space and therefore much higher capacity for storing energy in the thermal mass. Commercial buildings account for approximately 36% of the electricity consumption in the U.S., of which the heating, ventilation, and air conditioning (HVAC) load consumes about 32%. Furthermore, most modern commercial buildings are equipped with advanced building management systems (BMS) with the capability to monitor and control HVAC systems through wired or wireless communication links, which significantly reduces cost of using commercial HVAC load to serve power systems. Therefore, the HVAC load in commercial buildings is considered as one of the best candidates among various flexible building loads to provide grid services.

In this dissertation, methodologies and approaches have been derived in load modeling and control for providing grid services in distribution system. In the first part of dissertation, a feeder load disaggregation algorithm is developed to use the smart meter data and feeder head information to model the nodal load profiles in distribution system for time-series analysis. This method will generate a unique load shape with their aggregated profile matches the actual feeder information. In the second part of this dissertation, I developed a centralized control algorithm to control the power consumption of the HVAC system in commercial building to provide grid services. Meanwhile, the zonal air temperatures are still within their comfortable range. This algorithm allows the power consumption of the commercial building to follow the desired grid service signal.

© Copyright 2020 by Jiyu Wang

All Rights Reserved

Load Modeling and Control for Providing Grid Services in Distribution System

by
Jiyu Wang

A dissertation submitted to the Graduate Faculty of
North Carolina State University
in partial fulfillment of the
requirements for the degree of
Doctor of Philosophy

Electrical Engineering

Raleigh, North Carolina

2020

APPROVED BY:

Dr. Ning Lu
Committee Chair

Dr. David Lubkeman

Dr. Srdjan Lukic

Dr. Yunan Liu

DEDICATION

To my mother Ying Song, my father Dr. Hongbin Wang

BIOGRAPHY

Jiyu Wang was born in Harbin, Heilongjiang, China. He received his Bachelor of Engineering degree in Electrical Engineering and Automation from China Agricultural University in June 2014 and received his Master of Engineering degree in electrical engineering from North Carolina State University in August 2016. He is currently pursuing the Ph.D. degree in electrical engineering at North Carolina State University, Raleigh, NC. His current research interests include feeder load modeling, control of virtual battery and voltage control for renewable energy integrated distribution system.

ACKNOWLEDGMENTS

I would like to sincerely thank my academic advisor, Dr. Ning Lu, for her continuous support during my Ph.D., for her guidance, patience, and encouragement. I am always inspired by her enthusiasm, perseverance, and conscientiousness for research. The invaluable advice she provided me on research, career development, presentation, technical writing, and many other aspects is a priceless fortune to me. I could not have imagined having a better advisor and she is someone I will forever be thankful to.

My great appreciation and thankfulness also go to my committee members: Dr. David Lubkeman, Dr. Srdjan Lukic and Dr. Yunan Liu, for their precious time, valuable suggestions, and help. Their passion on research always motivated me to devote myself to my research and the exploration to the new areas.

I would also like to thank my mentors and colleagues in Pacific Northwest National Laboratory and National Renewable Energy Laboratory during my internships. I appreciate the internship opportunities and all the guidance you provided me on the research topic. It is a great pleasure to work with all of you.

I am deeply grateful for having many great lab mates in the past few years. I would like to express my sincere thanks to them: Xiangqi Zhu, Xinda Ke, Jiahong Yan, Jian Lu, Weifeng Li, Maziar Vanouni, Gonzague Henri, Ming Liang, Yao Meng, David Mulcahy, Catie McEntee, Asmaa Alrushoud, Fuhong Xie, Mingzhi Zhang, Si Zhang, Rongxing Hu, Lidong Song, Yiyang Li, Victor Paduani and Bei Xu. It has been fortunate to work with them and I was always motivated from our discussions. I would like to thank all my friends, who have made my graduate life full of excitement and fun. We spent countless wonderful time together in Raleigh and I am always grateful for their friendship and support.

I am also grateful for being a student at North Carolina State University. Being a part of the Wolfpack is one of the best decisions in my life. During my time at NC State, I have spent many of my spare time at Carter-Finley Stadium, PNC Arena, Reynolds Coliseum, and Doak Field at Dail Park to watch the NC State football, basketball, baseball, and many other sports. I have a lot of great memories at these games with my wife, Shuchi Liu. I will never forget these memories. The spirit of the Wolfpack has inspired me during tough phases of my research. We are the red and white from NC State. Go Wolfpack!

Finally, I would like to thank my parents, Ying Song and Dr. Hongbin Wang, for their love and support since my birth. They always try their best to support and encourage me to do what I want. Without their constant support, I would never have had a chance to start and finish a Ph.D. Their constant understanding and unconditional love are the greatest fortune in my entire life.

TABLE OF CONTENTS

LIST OF TABLES	viii
LIST OF FIGURES	ix
CHAPTER 1 INTRODUCTION	1
1.1 Work Overview	1
1.2 Feeder Load Modeling for QSTS analysis.....	3
1.3 Control Strategy for HVAC System in Commercial Building	6
CHAPTER 2 FEEDER LOAD DISAGGREGATION ALGORITHM	12
Nomenclature.....	12
2.1 Background	15
2.2 Problem Formulation.....	16
2.2.1 Data Preparation	16
2.2.2 Problem Formulation of FLDA	17
2.3 FLDA-LPS Algorithm	18
2.3.1 Selection of Pivot Points.....	18
2.3.2 Random Load Ratio.....	18
2.3.3 Recursive Matching Algorithm	19
2.3.4 Similarity Index for Load Profile Selection.....	21
2.3.5 Tolerance of the Matching Error	23
2.3.6 Considerations on Load Types	24
2.3.7 FLDA-LPS Result Evaluation Criterion.....	24
2.3.8 FLDA-LPS Algorithm Summary	25
2.4 FLDA-LPA Algorithm.....	26
2.4.1 Allocation based on Distribution Transformer Rating	27
2.4.2 Allocation based on Distribution Transformer Rating	28
2.5 FLDA-LPS Performance Evaluation	28
2.5.1 Simulation Setup.....	29
2.5.2 Selection of the Ratio of Random Load Profiles	30
2.5.3 Selection of Pivot-points	31
2.5.4 Selection of Pivot-points	33
2.5.5 Performance using different Load Profile Database.....	34
2.6 FLDA-LPA Performance Evaluation.....	35
2.7 Power Flow Results Comparison.....	38
2.8 Other FLDA methods	44

2.8.1	With nodal peak load	44
2.8.2	With feeder head peak load	49
2.9	Conclusions	55
CHAPTER 3 CONTROL OF COMMERCIAL BUILDINGS FOR GRID SERVICES.....		57
Nomenclature.....		57
3.1	Commercial HVAC System Modeling.....	59
3.1.1	Multi-Zone Thermal Model.....	61
3.1.2	Supply Fan Model	64
3.1.3	Chiller Model.....	64
3.2	Commercial HVAC System Control Strategy	65
3.2.1	System-level Control	69
3.2.2	Zone-level Control.....	69
3.3	Case Study	74
3.3.1	Baseline Following.....	80
3.3.2	Duck Curve Offsetting.....	85
3.3.3	PV output smoothing	88
3.4	Conclusions.....	91
CHAPTER 4 SUMMARY AND FUTURE WORK.....		93
4.1	Summary of Previous and Current Research.....	93
4.1.1	Feeder Load Disaggregation Algorithm	93
4.1.2	Control of HVAC System in Commercial Building.....	94
4.2	Vision and Plan of Future Work.....	95
4.2.1	Feeder Load Disaggregation Method	95
4.2.2	Control of Commercial HVAC System.....	96
4.2.3	Feeder Impact of Building Demand Response	96
REFERENCES		98

LIST OF TABLES

Table 2.1 LPS results with different number of simulations.....	25
Table 2.2 Weekly matching results	32
Table 2.3 Monthly matching results.....	32
Table 2.4 Yearly matching results.....	33
Table 2.5 Performance comparison.....	34
Table 2.6 Feeder information	49
Table 2.7 Feeder head profile aggregation summary	55
 Table 3.1 MAPE of different machine learning techniques.....	 63
Table 3.2 MAPE with different parameters in random forest.....	64
Table 3.3 HVAC system parameters.....	74
Table 3.4 Parameter of each thermal zone for the building model	76
Table 3.5 Baseline following performance	84
Table 3.6 Comparison of temperature control performance	85
Table 3.7 Duck curve offsetting performance.....	88
Table 3.8 PV smoothing performance.....	89

LIST OF FIGURES

Figure. 1.1 Energy consumption ratio.....	2
Figure. 2.1 Total load consumption for three houses.....	16
Figure. 2.2 Flowchart of using FLDA to do model distribution feeder	17
Figure. 2.3 Pivot points and random load selection.....	18
Figure. 2.4 Pivot points selected using the Target and Reference load profiles	21
Figure. 2.5 A graphical illustration of the Similarity Index calculation	23
Figure. 2.6 Residential house sample load profiles	29
Figure. 2.7 Commercial house sample load profiles.....	30
Figure. 2.8 Performance comparison using different random load ratios.....	31
Figure. 2.9 Performance comparison using two different load profile databases	35
Figure. 2.10 An example load disaggregation result	37
Figure. 2.11 LPA results for different transformer sizes	37
Figure. 2.12 Transformer loading ratios in an example day.	38
Figure. 2.13 Topology of the distribution feeder	39
Figure. 2.14 Voltage difference percentage for three phases.....	40
Figure. 2.15 Boxplot of voltage difference at different time	41
Figure. 2.16 Nodal voltage error distributions.....	42
Figure. 2.17 Graphic user interface of FLDA	43
Figure. 2.18 Graphic user interface of distribution feeder planning tool.....	43
Figure. 2.19 Topology of IEEE-123 test system.....	47
Figure. 2.20 Boxplot of the number of houses calculated for different L_i	47
Figure. 2.21 Aggregated Load shapes obtained for $L_i = 200$ kW	48

Figure. 2.22 Load profile aggregation result at one load node	49
Figure. 2.23 Histogram for number of houses for 100 simulations in one day	54
Figure. 2.24 Boxplot for number of houses in seven days.....	54
Figure. 2.25 Feeder head profile comparison	55
Figure. 3.1 The configuration of a typical HVAC system that serves office buildings.....	61
Figure. 3.2 Illustration of the proposed control	68
Figure. 3.3 Predict and actual temperature comparison for the first example thermal zone	77
Figure. 3.4 Predict and actual temperature comparison for the second example thermal zone...	77
Figure. 3.5 Predict and actual fan power comparison.....	78
Figure. 3.6 Outdoor temperature in °C	80
Figure. 3.7 Boxplot of zonal temperatures for each testing day in the baseline following case..	82
Figure. 3.8 Temperature profiles for 17 zones on day 14 in the baseline following case	83
Figure. 3.9 Offsetting ‘duck curve’ in California	86
Figure. 3.10 Temperatures profiles for 17 zones using the asymptotic allocation on day 14 in the duck curve offsetting case	87
Figure. 3.11 Daily temperature and airflow rate of one example thermal zone	88
Figure. 3.12 Smoothing PV output	90
Figure. 3.13 Duration time distribution of each temperature violation for two methods	91

CHAPTER 1 INTRODUCTION

1.1 Work Overview

Renewable energy resources exist over wide geographical areas and have advantages such as significant energy security, climate change mitigation and economic benefits. With the increasing demand of electricity and the fact that primary energy of many traditional generation resources cannot be refilled in centuries, renewable energy has been developed rapidly around the world. In 2016, the renewable energy in the United States accounted for over 15% of total electricity generation, up from 13.7% in 2015 [1]. Among these renewable energy resources, electricity generated by wind energy and solar photovoltaic (PV) is increasing rapidly.

Nevertheless, the variability and uncertainty of these renewable generation start causing a variety of operational issues on the service quality and reliability of power grid [2-5]. For example, many high-penetration PV systems have occurred many frequent voltage ramping events, over- and under-voltage violations, and frequent operations of utility Volt-Var devices. Therefore, grid services are required to mitigate these problems which are brought by the increasing renewable generation.

Currently, supply-side reserves are mainly used to handle these disadvantages of renewable energy. The disadvantages of this method include reduced generation efficiency and net-carbon benefit. The increasing percentage of renewable energy also limited this service as it is mainly achieved by traditional generation resources. Energy storage system (ESS) is becoming another popular choice to address the uncertainty of renewable generation [6-9]. ESS can store energy for future use and smooth out power fluctuations, which can help to integrate high penetration of renewable energy in grid and provide grid services such as frequency regulation, load following

and spinning reserves [10-13]. Despite these benefits, the high cost of ESS under today's technology still makes it hard to be adopted in all power systems.

Recently, demand-side control becomes an alternative approach to resolve the problems caused by high PV and wind penetration. Demand response (DR) can help to balance power in a simple way. Building loads is one of the most important DR resources because of its large energy consumption. As shown in Figure. 1.1, buildings consume approximately 70% of energy in the United States [14]. Meanwhile, the thermal controllable load (TCL) such as the heating, ventilation, and air conditioning (HVAC) system and water heater, consumes more than 30% of electricity in buildings [15]. When the indoor temperature of a building varies within a narrow range, occupant comfort will not be compromised. Thus, many research activities have been focused on controlling the HVAC system in buildings to provide a variety of grid services, such as frequency regulation and peak load shifting services [16-17].

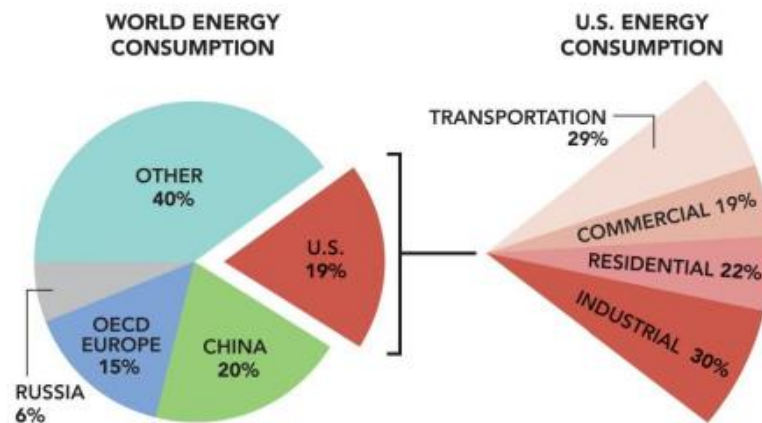


Figure. 1.1 Energy consumption ratio

To integrate building load providing grid services in real world, several studies are required to conduct in order to find how the demand response from building will influence the grid. First, to model the demand response event, time-series analysis becomes necessary because both the impact from grid and building level can be captured. Therefore, quasi-static time-series

(QSTS) analysis [18] was developed to model low-frequency dynamics of distribution systems and to investigate building demand response impacts such as the duration time of indoor temperature out of comfortable range and the power signal following accuracy. In this analysis, modeling the load in a distribution feeder into a model that can be used for QSTS simulation is an important step [19]. Second, after a grid service signal is sent to a building, the building needs to operate its HVAC system so that the power consumption matches the desired signal. For most of residential buildings, it is easier as their HVAC systems only have on/off status, however, for the HVAC system in commercial building, the control strategy needs to be designed. Third, after the feeder modeling method is developed and the single building control strategy is proposed, the DR impacts from building and feeder level will be discussed. For each kind of grid service, we will also study the DR dispatch strategy. In this dissertation, among these three research areas, the studies on distribution feeder load modeling and single building HVAC system power control are my past research work. The last feeder level study will be introduced as future work in Chapter 4. In the following subsections we will introduce the state of art of each research aspect to demonstrate what methodologies are in the existing literatures and what approaches are proposed in my dissertation.

1.2 Feeder Load Modeling for QSTS analysis

QSTS power flow simulations have been widely used for feeder modeling in power distribution system planning studies [18-22] in recent years. It can also be used for renewable energy integration and volt-var control study [23-27]. A critical step in a QSTS simulation is the selection of nodal load profiles. In earlier QSTS studies, researchers use the shape of the feeder-head load profile as a template to populate the nodal loads. The feeder-head load profile is first normalized by its peak load and then scaled up to obtain a nodal load profile according to the rating

of the distribution transformers located at that node [28-30]. Using this method, load nodes on the same feeder will have the same load shape. Therefore, we call this approach the one-load-shape-scaling (OLSS) method.

The OLSS approach has two main drawbacks. First, because all load nodes have the same load shape, there is no diversity in nodal load changes, i.e., all nodal loads will increase and decrease simultaneously, which is far from realistic. Second, because a feeder level load profile carries only load variation characteristics of a large amount of aggregated end use loads, using its shape will fail to represent the load characteristics of the end use load characteristics, making it impossible to model behind-the-meter (BTM) Distributed Energy Resources (DERs).

To improve the OLSS method, Mather [31] and Zhu et al. [32] used a multiple-load-shape-scaling (MLSS) method for allocating typical load profiles in different load classes to each load node. For example, street lighting loads are allocated to a small load node and industrial or commercial loads are allocated to nodes with higher distribution transformer ratings. The load profile of each load class is derived from a group of actual load profiles. Thus, MLSS can allocate several classes of typical load profiles [33]. Although MLSS adds more diversity in nodal load shapes, it cannot resolve the two fundamental drawbacks of OLSS. Because a typical distribution feeder supplies hundreds or thousands of customers, the nodal load profiles can be very different from each other depending on load composition, end use characteristics and total number of customers served, etc. Using only a limited number of typical load profiles is therefore an infeasible solution.

Another disadvantage of OLSS and MLSS is that only the aggregated load profile at each load node is considered so the load profiles of each customer supplied by a node are still unknown to the modelers. In a lot of DER studies, a modeler needs to know building level load profiles so

that impacts of using the BTM DERs (e.g., roof-top photovoltaics (PV), batteries, electric vehicles, controllable loads, etc.) can be modeled when used to provide grid services [34-35].

To address the aforementioned problems, in [36-37], a one-pivot-pair (i.e., peak and valley) based load disaggregation method is proposed by Wang et. al for the first time. Traditional load disaggregation is mainly from building-level to appliance-level and is used for load composition or load forecast propose [38-42]. However, this approach uses a number of pivot points on the feeder-head load profile as references to select load profiles from a load profile database populated by time-series smart meter measurements.

In this work, we extended the one-pivot-pair algorithm to a multiple-pivot-pair based, two-stage feeder load disaggregation algorithm (FLDA). The two stages are the load profile selection (LPS) stage and the load profile allocation (LPA) stage. In the LPS stage, a random load profile selection process is first conducted to produce load diversity. Then, a few pivot pairs are selected from the feeder-head load profile as the matching targets. After that, a matching algorithm is run repetitively such that at each run, the selected load profile provides the best match to the reference load profile at the pivot points while meeting the load composition requirement. In the LPA stage, an allocation algorithm runs repetitively to assign the LPS selected load profiles to each load node. The proposed method is developed and validated using actual utility feeder data and 4302 sets of yearly smart meter data. Three performance criteria are used to measure the performance of the algorithm: accuracy of selecting the total number of load profiles, accuracy of matching load shapes, and accuracy of meeting load composition and total nodal square footage requirements.

There are three main contributions of our work. First, a dynamic reference profile matching method is developed to improve matching accuracy, the success rate for selecting feasible load profiles, and the computational speed of the LPS process. Second, a multiple-pivot-pair matching

algorithm is developed to meet the feeder load disaggregation needs for weekly-, monthly- or yearly feeder-head load profiles. Third, feeder/nodal load compositions and square-footage requirements are accounted for in the load profile selection and allocation processes.

1.3 Control Strategy for HVAC System in Commercial Building

Energy storage systems are promising to resolve operational issues in power systems with high penetration of variable and uncertain renewable generation [43],[44]. Among various energy storage technologies, battery energy storage systems (BESSs) have the best controllability and operational flexibility and therefore can be used for many different grid applications, such as frequency regulation [45],[46], spinning and non-spinning reserves [47], energy balancing [49], [48] critical infrastructure investment deferral [7], and peak shaving [50]. Nevertheless, the cost of using dedicated BESSs for grid services remains high for utilities and third-party service providers at current market rates. Using batteries from plug-in electric vehicles (PEVs) to serve the grid helps to improve economic performance. Control methods have been proposed for using PEVs to provide different grid services, such as voltage and frequency regulation [51] and load flattening [52].

On the other hand, buildings with inherent ability to store heat in thermal mass can vary their power consumption and shift the electric energy consumption to an earlier or later time with little impacts on customers' comfort and convenience. Compared to a residential house, commercial buildings have much larger floor space and therefore much higher capacity for storing energy in the thermal mass [53]. Commercial buildings account for approximately 36% of the electricity consumption in the U.S., of which the heating, ventilation, and air conditioning (HVAC) load consumes about 32% [54]. Furthermore, most modern commercial buildings are equipped with advanced building management systems (BMS) with the capability to monitor and

control HVAC systems through wired or wireless communication links [55], which significantly reduces cost of using commercial HVAC load to serve power systems. There-fore, the HVAC load in commercial buildings is considered as one of the best candidates among various flexible building loads to provide grid services.

Many studies have been dedicated to using flexible commercial HVAC load for grid services, especially through the application of model predictive control (MPC) technique. For example, an economic MPC method is proposed in [56] for optimizing building demand and energy cost under the time-of-use price policy. In [57], the authors present an MPC method to optimize the operation of a variable volume and multi-zone HVAC unit in a mid-size commercial building, using dynamic estimates and predictions of zone loads and temperatures. An MPC framework is proposed in [58] to determine optimal operating strategies of commercial buildings in consideration of energy use, energy expense, peak demand, economic de-mand response revenue, and frequency regulation revenue. In [59], an MPC method is proposed to find the best zone temperature setpoint schedule considering both cost and CO₂ emissions, subject to operator preferences. In [60], the authors propose a temperature control through the application of MPC strategies considering energy efficiency and comfort levels of commercial buildings. An MPC method is proposed for variable air volume HVAC systems in single-zone commercial buildings to provide frequency regulation in [61], assuming cooling and heating power can be directly controlled.

The MPC scheduling and control methods presented in previous studies are developed mainly based on detailed dynamic models while considering operational constraints for individual buildings. Coordination with other resources at the system level has not yet been well addressed. When coordinating flexible building assets with other resources over a large area, it is impractical

for grid operators to incorporate thousands of detailed dynamic building load models into their daily scheduling and dispatch systems. Therefore, simplified models that can capture the aggregated building load flexibility and can easily be scaled up to model a large number of resources are needed. To address this challenge, modeling building loads as virtual batteries (VBs) so that the flexibility of aggregated building loads can be characterized and modeled comparable to the battery charging and discharging process has been proposed in the past few years. A VB model is proposed in [62] to succinctly characterize aggregate power flexibility from building loads. In [63], the authors present a method to identify VB model parameters for commercial buildings. De-mand response flexibility from commercial buildings through setpoint changes is estimated in [64] using EnergyPlus simulation. A two-layer demand response flexibility estimation framework is developed in [65] to quantify power flexibility for different types of commercial buildings. In [66], the authors present an optimization method to construct VB model for commercial HVAC loads. The main advantage of modeling flexible building loads as VBs is that it allows them to be modeled and optimized similar to energy storage systems when formulating the grid operation problems, considering various physical, environmental, and climate constraints. In addition, with proper control, a VB can directly follow grid dispatch and regulation signals similar to an energy storage system.

An actual BESS uses dedicated power conversion systems for charging and discharging control, while the VB controller needs to account for different operational limitations of building loads. Thus, unlike the existing MPC methods that optimize building operation over a look-ahead time horizon, the VB controller will follow real-time signals (without knowing dispatch/regulation signals at future time steps) and will be constrained by user-defined zonal temperature limits. Several existing studies proposed methods for controlling commercial HVAC systems in real-time

to provide grid services. In [67], the authors propose a direct method (through static pressure setpoint) and an indirect method (through zone cooling temperature setpoint) for adjusting the fan power consumption in commercial buildings to provide frequency regulation. In [68], a control method is proposed for single-zone commercial buildings to provide low-frequency ancillary services. A feed-forward architecture is proposed based on a simplified single-zone model to control the fan power consumption to track regulation signals [69]. In [70], the authors introduce a supervisory control in a commercial building to provide frequency regulation service. A demand scheduling and control method was proposed in [71] to use fans in commercial buildings to provide ancillary services based on a single-zone model.

Most of the aforementioned studies use the fans in a commercial HVAC system as flexible demand without considering the chillers. However, because the power consumption of a chiller is normally 4-5 times that of the fans [72], ignoring the flexibility of the chillers is a major disadvantage. In addition, many previous studies in the area focused on frequency regulation with an assumption that the demand response signal is energy neutral. This significantly limits the application of the commercial HVAC systems for providing grid services. Another main shortfall in existing HVAC-based control methods is that most control algorithms are designed based on simplified single-zone models, which cannot accurately represent the thermal dynamics of multi-zone commercial buildings. Lastly, most existing HVAC control methods control thermostat setpoints instead of airflow rates. Because it is the airflow rate settings that determine the HVAC system power consumption and the zonal temperature variations, controlling air flow rates outperforms controlling thermostat setpoints in terms of both accuracy and maintaining zonal temperatures within the desired ranges.

To overcome those issues, in this work, we propose a novel VB charging/discharging control method for a multi-zone variable air volume (VAV) commercial HVAC system. Zonal airflow rates are controlled to adjust the power consumption of the fans and the chiller of an HVAC system without modifying user thermostat settings. The main contributions of this paper are summarized as follows.

- A real-time VB control method is proposed to adjust chiller power consumption in addition to fan power in a VAV commercial HVAC system. Given that the power consumption of chillers is typically 4-5 times of the fans, the proposed control yields much larger operational flexibility from the commercial building loads when providing grid services.
- The VB system does not require energy neutral signals and can provide a wide range of grid services.
- A machine-learning (ML)-based approach is proposed to determine the zonal airflow rate that satisfies the control needs. This approach significantly reduces computational time and complexity, making the developed method suitable for real-time control applications. Note that existing HVAC control approaches are mostly model-based, where simplified, bilinear, physics-based lumped thermal models of a single-zone or a multi-zone commercial HVAC system are used. Our results show that the ML-based method can more accurately capture the building thermal dynamics so that the temperature control performance is significantly improved compared with that of the model-based approach.
- An innovative two-level control architecture is proposed. At the system level, a mixed feedforward and feedback method is proposed to calculate the desired total airflow

rate. At the zonal level, two priority-based algorithms for allocating zonal airflow rates to meet the zonal temperature constraints are proposed and compared.

CHAPTER 2 FEEDER LOAD DISAGGREGATION ALGORITHM

This chapter introduces the methodologies developed for modeling the load of distribution systems in order to do QSTS analysis. First, the background and problem formulation of this study is presented. Then the feeder load disaggregation algorithms (FLDA) are proposed to model the nodal load profiles in QSTS study. Finally, the parameter selection of FLDA is discussed.

Nomenclature

A_i	Average square footage of buildings supplied by node i
$A_{i,k}$	Square footage of building k supplied by node i
A_m	Square footage of the building to be allocated
$\Delta A_{i,m}$	Square footage differential percentage between node i and the building to be allocated
D	Load profile database
D_{LT} (D_R, D_C, D_I)	Load profile database for a load type (residential, commercial and industrial)
D_{LSI}	Load profile set containing all load profiles with the largest similarity index
$D_{selected}$	Load profiles selected by LPS
e	Aggregated percentage error between the actual feeder-head load profile and the profile generated by simulation
f	Flag to check if the load profile can be allocated to the feeder
i	Index of the load node
j	Index of the pivot-point pair
J	Total number of pivot-point pairs

k	Index of the selected load profiles at node i
m	Index of load profiles
N_D	Number of load profiles in load pool D
N_i	Number of load profiles at node i
N_i^{min}, N_i^{max}	Maximum/minimum customers at node i
N_L	Number of load nodes in the feeder
N_{match}	Number of load profiles selected in the shape matching step
N_{random}	Number of load profiles selected in the random selection step
N_T	Matching time duration
N_{feeder}	Total number of selected profiles for the feeder
$N_{selected}$	Number of load profiles selected by LPS
n_{peak}^j , n_{valley}^j	Indices of peak/valley pivot points in X_m
P_{feeder}	Actual feeder-head load profile
\tilde{P}_{feeder}	Generated feeder-head load profile
P_D	Aggregated load profile of D
P_{random}	Aggregated profile for the load profiles selected in the random selection process
P_{random}^{target}	Target peak of P_{random}

P_{match}	Aggregated load profile of load profiles selected in the shape matching process
P_{tar}	Target load profile for shape matching
P_{ref}	Reference load profile
\tilde{P}_{LT} ($\tilde{P}_R, \tilde{P}_C, \tilde{P}_I$)	Aggregated load profile of the selected load profiles that belong to a certain load type (residential, commercial or industrial)
P_m	The m^{th} load profile
\tilde{P}_i	Aggregated load profile at load node i
$P_{i,k}$	Load profile k at load node i
q	Index for the first procedure in LPA
φ_m	Similarity index of load profile m
Ψ	Set contains φ_m for all load profiles
R_i	Maximum loading factor of transformer i
R_{LT} (R_R, R_C, R_I)	Target ratio of a certain load type (residential, commercial or industrial)
R_{random}	Randomization ratio
S_i	Distribution transformer rating at node i
$s(m)$	Decision variable representing whether load profile m is selected or not.
t	Index of time step
$t_{peak}^{pp,j}$	j^{th} pivot-point that requires more load to compensate at this time point
$t_{valley}^{pp,j}$	j^{th} pivot-point that requires less load to compensate at this time point

X_m	Matrix for similarity index calculation
u	Number of iterations in RT-LPM/ RNR-LPM
ε	Acceptable error tolerance

2.1 Background

The goal of FLDA is to help modeling distribution feeder down to building level for detailed QSTS simulation study. A feeder-head load profile is usually known to utility engineers but nodal load profiles on the feeder are not. Thus, in this section, we present a pivot-point based, two-stage feeder load disaggregation algorithm using smart meter data. The two stages are load profile selection (LPS) and load profile allocation (LPA). In the LPS stage, a random load profile selection process is first executed to meet the load diversity requirement. Then, a few pairs of pivot points are selected as the matching targets. After that, a matching algorithm will run repetitively and select one load profile at a time to match the reference load profile at the pivot points while satisfying load composition requirements. In the LPA stage, the LPS selected load profiles are allocated to each load node on the feeder considering distribution transformer loading limits, load composition, and square-footage. The proposed method is developed and validated using actual feeder and smart meter data from a North Carolina service area. Three performance criteria are used to measure the performance of the algorithm: accuracy of selecting the total number of load profiles, accuracy of matching load shapes, and accuracy of meeting load composition and total nodal square footage requirements. Simulation results show that the proposed method provides more accurate feeder simulation results than the existing load profile allocation methods.

2.2 Problem Formulation

2.2.1 Data Preparation

At the feeder-head, the total load consumption of the feeder, the ratings of distribution transformers, and nodal load types (i.e. residential, commercial and industrial) are usually known to utility engineers. In recent years, utilities have installed thousands and millions of smart meters, making it possible for distribution engineers to have access to end use energy consumptions. Define the power measurements from the m^{th} smart meter at time t_n as, $P_m(t_n)$. Let $D_{N_D \times N_T}$ be the load profile database that consists of N_D set of smart meter measurements, each with N_T data points, then we have

$$D_{m,n} = P_m(t_n). \quad (2.1)$$

In this work, 4302 sets of smart meter data with 30-minute data resolution are used to populate D . Thus, for a load profile database D in January, $N_D = 4302$ and $N_T = 2 \times 24 \times 31$. For example, Figure. 2.1 shows the daily house-level load profiles for three example buildings. D can also be further divided into a few sub-groups. In this work, D has two sub-groups: residential (D_R) and commercial (D_C).

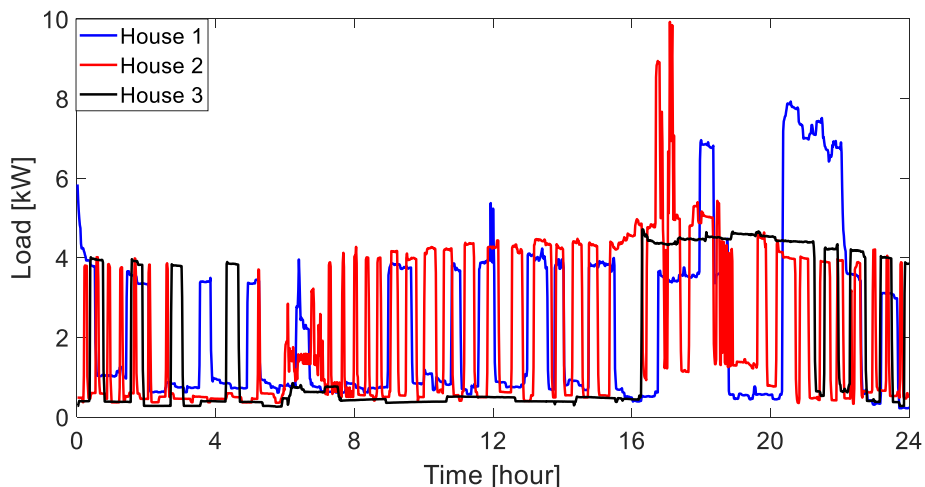


Figure. 2.1 Total load consumption for three houses

2.2.2 Problem Formulation of FLDA

The flowchart of using FLDA to do QSTS or demand response simulation is shown in Figure. 2.2. There are two main steps in FLDA: load profiles selection (FLDA-LPS) and load profile allocation (FLDA-LPA). As shown in Figure. 2.2, in the first step, FLDA-LPS selects N_{feeder} load profiles from D so that the aggregated load, \tilde{P}_{feeder} , matches P_{feeder} . Thus, the objective function of the LPS is

$$\min \sum_{n=1}^{N_T} (|P_{feeder}(t_n) - \tilde{P}_{feeder}(t_n)|). \quad (2.2)$$

$$\tilde{P}_{feeder}(t_n) = \sum_{m=1}^{N_{feeder}} P_m(t_n). \quad (2.3)$$

Then, the FLDA-LPA algorithm will assign the selected N_{feeder} load profiles to each load node so that the following two constraints can be met:

$$\max\{\sum_{k=1}^{N_i} P_{i,k}(t_n)\} \leq S_i * R_i, \quad (2.4)$$

$$N_i^{min} \leq N_i \leq N_i^{max}. \quad (2.5)$$

In the next few subsections, each step illustrated in Figure. 2.2 will be introduced in detail.

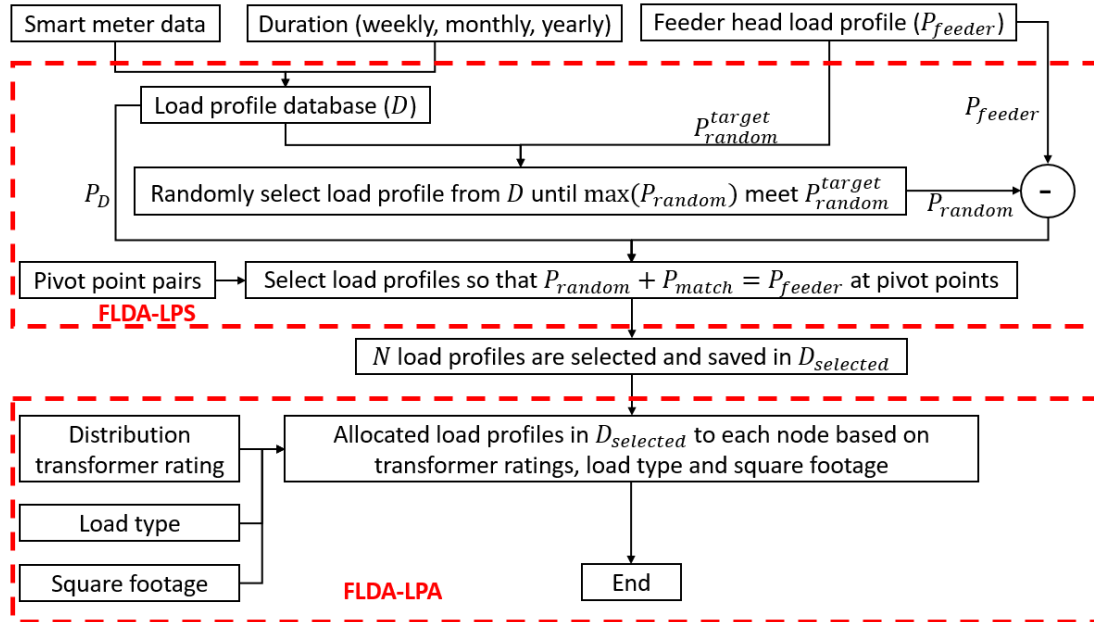


Figure. 2.2 Flowchart of using FLDA to do model distribution feeder

2.3 FLDA-LPS Algorithm

This section presents the FLDA-LPS algorithm.

2.3.1 Selection of Pivot Points

In distribution system studies, it is neither realistic nor necessary to find a perfect match for the entire time series. Therefore, we first simplify (2.2) from minimizing the cumulated error at all points to minimizing the cumulated error at the pivot points. So (2.2) can be reformulated as

$$\min \sum_{j=1}^J (|P_{feeder}(t^{pp,j}) - \tilde{P}_{feeder}(t^{pp,j})|). \quad (2.6)$$

Pivot points are critical points on a load curve that can capture key load shape information. Thus, if one pair of pivot points are selected, they are normally the peak and valley loads together with their corresponding timestamps, as shown in Figure. 2.3. For matching a daily load profile, selecting one pair of pivot points is usually sufficient. However, when matching longer time-series curves, multiple pairs are needed to provide a wider range of match. In the following sections, we compare the impacts when selecting different numbers of pivot pairs on matching accuracy when disaggregating weekly, monthly and yearly time-series load profiles.

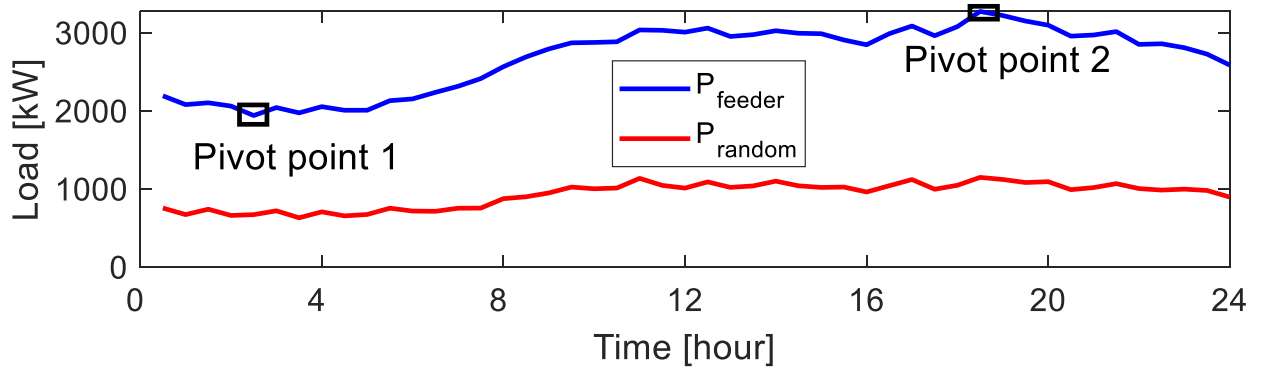


Figure. 2.3 Pivot points and random load selection

2.3.2 Random Load Ratio

If all load profiles are selected to satisfy (2.6), the resulting load profiles tend to have similar load shapes as that of P_{feeder} . However, on an actual distribution feeder, because of the

load diversity, a significant number of loads have distinct load shapes. Therefore, we proposed a random load profile selection process to achieve the targeted level of load diversity.

Define P_{random} as the aggregated load profile for the randomly selected load profiles and P_{match} as the aggregated load profile for the load profiles that are selected to match \tilde{P}_{feeder} and P_{feeder} , we have

$$\tilde{P}_{feeder}(t_n) = P_{random}(t_n) + P_{match}(t_n), \quad (2.7)$$

where

$$P_{random}(t_n) = \sum_{m=1}^{N_{random}} P_m(t_n), \quad (2.8)$$

$$P_{match}(t_n) = \sum_{m=1}^{N_{match}} P_m(t_n). \quad (2.9)$$

To control load diversity, a random load ratio, R_{random} , is introduced to cap the peak of P_{random} using

$$(1 - \varepsilon) \times P_{random}^{target} \leq \max(P_{random}) \leq P_{random}^{target}, \quad (2.10)$$

$$P_{random}^{target} = R_{random} \times \min(P_{feeder}), \quad (2.11)$$

where

$$0 \leq R_{random} \leq 1.$$

Thus, FLDA randomly selects load profiles from D until (2.10) is met and save the N_{random} selected load profiles to $D_{selected}$. By capping the maximum load of P_{random} by the minimum load of P_{feeder} , P_{random} will be guaranteed to be lower than P_{feeder} when $R_{random} \leq 1$. The red curve in Figure. 2.3 shows an example of P_{random} with $R_{random} = 0.5$. The impact of using different R_{random} values on the algorithm performance is discussed in the following section.

2.3.3 Recursive Matching Algorithm

After random load selection, FLDA-LPS will select load profiles from D so that \tilde{P}_{feeder}

can match P_{feeder} . Thus, a recursive target load profile matching (RT-LPM) method is developed.

Calculate an initial target profile as

$$P_{tar}^{(0)}(t_n) = P_{feeder}(t_n) - P_{random}(t_n) \quad (2.12)$$

At each subsequent selection step, $P_m^{(u)}$ is selected from D and put into $D_{selected}$. At the end of the u^{th} selection step, $P_{tar}^{(u+1)}$ is recalculated by

$$P_{tar}^{(u+1)}(t_n) = P_{tar}^{(u)}(t_n) - P_m^{(u)}(t_n). \quad (2.13)$$

A pivot pair can be selected from $P_{tar}^{(u+1)}$ using

$$P_{tar}^{(u)}(t_{peak}^{pp}) = \max(P_{tar}^{(u)}(t_n)), \quad (2.14)$$

$$P_{tar}^{(u)}(t_{valley}^{pp}) = \min(P_{tar}^{(u)}(t_n)). \quad (2.15)$$

Search D to find a load profile $P_m^{(u)}$ with valley and peak at or close to t_{valley}^{pp} and t_{peak}^{pp} .

Extend (2.14) and (2.15) if multiple pivot pairs are needed.

However, using pivot points from P_{tar} for selecting load profiles without considering the load characteristics in D has a major drawback. When a load profile is selected from D to match P_{tar} , statistically, P_{match} with the same or similar load shape as the aggregated load profile of D (See the second subplot of Figure. 2.4) is more likely to be selected. As a result, \tilde{P}_{feeder} may match P_{feeder} well at points adjacent to the pivot points but poorly at points away from the pivot points.

To resolve this issue, we developed a recursive normalized reference load profile matching (RNR-LPM) algorithm to normalize P_{tar} by the aggregated load profile of D using

$$P_{ref}^{(u)}(t_n) = \frac{P_{tar}^{(u)}(t_n)/\max(P_{tar}^{(u)}(t_n))}{P_D(t_n)/\max(P_D(t_n))}, \quad (2.16)$$

where

$$P_D = \sum_{m=1}^{N_D} P_m. \quad (2.17)$$

By doing so, the pivoting points are changing at each matching step so that at the end of the matching process, the aggregated load profile will provide a wider match to the actual feeder load profile. As shown in the third subplot of Figure. 2.4, the pair of pivot points can be calculated as

$$P_{ref}^{(u)}(t_{peak}^{pp}) = \max(P_{ref}^{(u)}(t_n)), \quad (2.18)$$

$$P_{ref}^{(u)}(t_{valley}^{pp}) = \min(P_{ref}^{(u)}(t_n)). \quad (2.19)$$

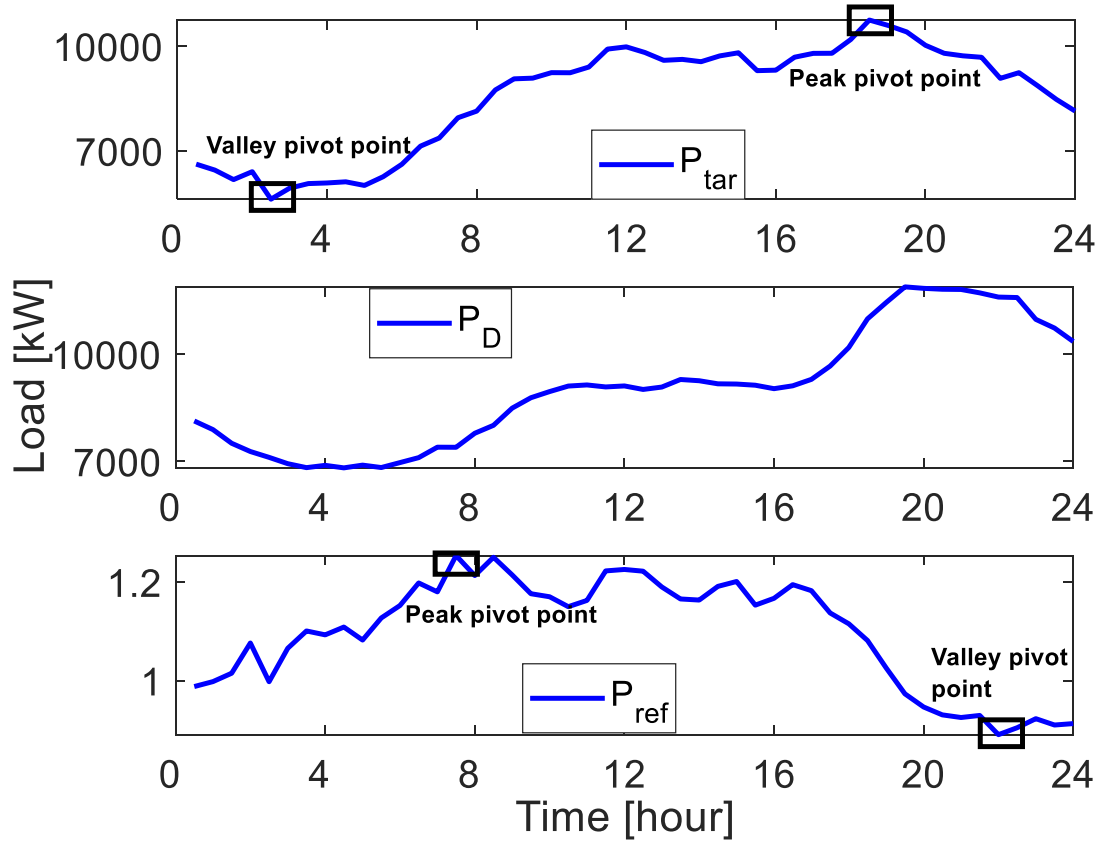


Figure. 2.4 Pivot points selected using the Target and Reference load profiles

2.3.4 Similarity Index for Load Profile Selection

At each matching step, for each load profile in D , form a sorting matrix \mathbf{X} as follows:

$$\mathbf{X}_m = \begin{pmatrix} P_m(t_1) & P_m(t_2) & \dots & P_m(t_{N_T}) \\ t_1 & t_2 & \dots & t_{N_T} \end{pmatrix}. \quad (2.20)$$

Sort \mathbf{X}_m ascendingly by power (i.e., the first row), and find indices n_{peak}^j and n_{valley}^j such that $\mathbf{X}_m(2, n_{peak}^j) = t_{peak}^{pp,j}$ and $\mathbf{X}_m(2, n_{valley}^j) = t_{valley}^{pp,j}$, where $t_{peak}^{pp,j}$ and $t_{valley}^{pp,j}$ are the timestamps of the pivot points on the reference curve at that step, as shown in the third subplot of Figure. 2.4.

Then, calculate the similarity index using

$$\varphi_m = \sum_{j=1}^J (n_{peak}^j - n_{valley}^j). \quad (2.21)$$

Note that a load profile with a larger φ_m tends to have a higher load at $t_{peak}^{pp,j}$ or a lower load at $t_{valley}^{pp,j}$. As shown in Figure. 2.5, the pivot points on the reference profile has t_{peak}^{pp} at 7:30 a.m. and t_{valley}^{pp} at 22:00. After sorting two load profiles ascendingly, we calculate the index of the corresponding load points on the sorted load profile so that φ_1 is calculated as 30 and φ_2 is 46. As observed from the first two subplots in Figure. 2.5, Profile 2, with a higher similarity index, can provide a better matching result than Profile 1.

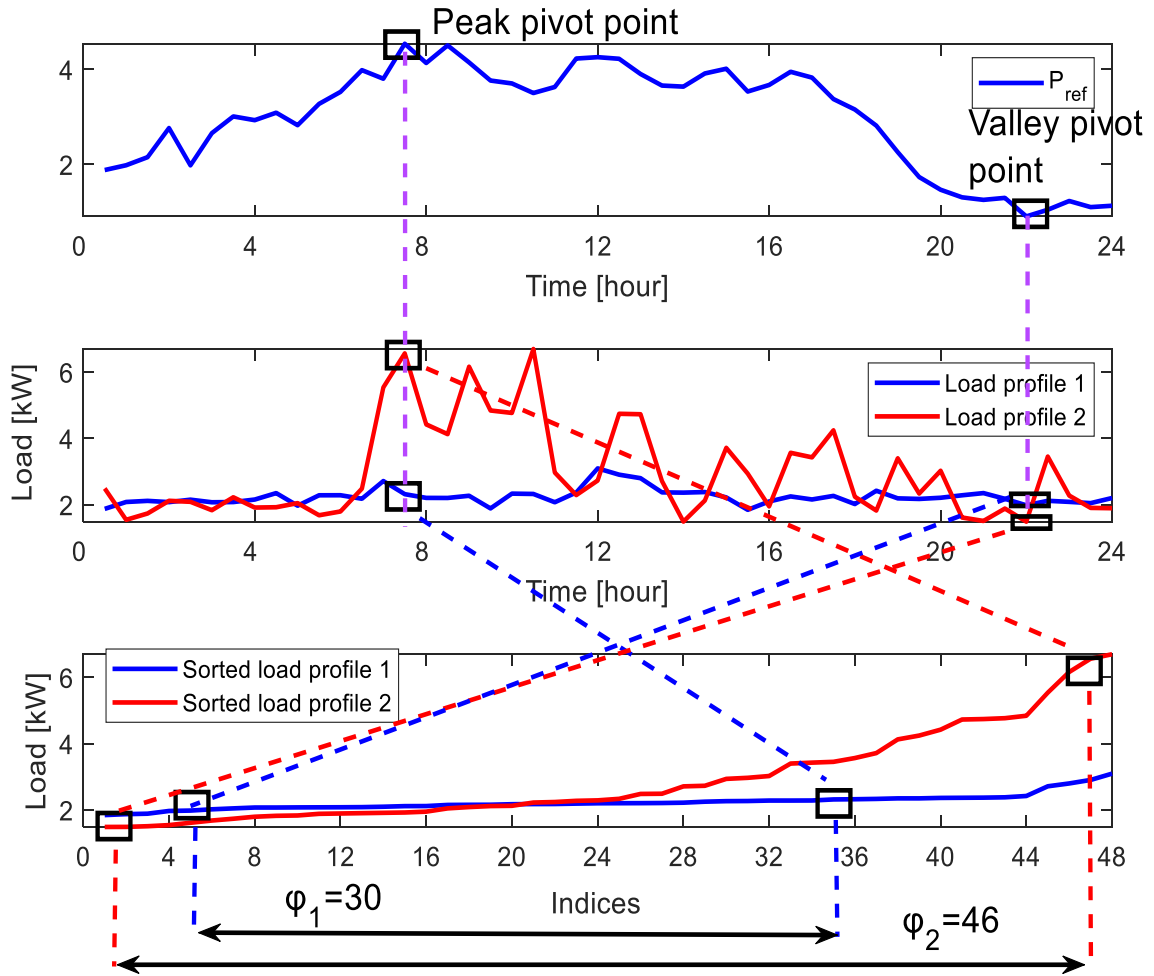


Figure. 2.5 A graphical illustration of the Similarity Index calculation

2.3.5 Tolerance of the Matching Error

Define the tolerance of the matching error as

$$e = \sum_{t=1}^{N_T} \left| \frac{P_{feeder}(t_n) - \bar{P}_{feeder}(t_n)}{P_{feeder}(t_n)} \right|. \quad (2.22)$$

In the recursive process, after a load profile is selected, e should decrease. Thus, if a selected load profile causes e to increase, the load profile will be unselected and will be taken out of D .

2.3.6 Considerations on Load Types

To consider different load types, D can be divided into different load groups. For example, D_R consists of only residential load profiles and D_C consists of only commercial load profiles. Then, instead of selecting load profiles from D , load profiles can be selected from different load groups. The following criteria are used to select load profiles while accounting for different load types:

$$\frac{\sum_{t=1}^{N_T} \tilde{P}_{LT}(t_n)}{\sum_{t=1}^{N_T} \tilde{P}_{feeder}(t_n)} < R_{LT}, \quad (2.23)$$

$$\tilde{P}_{LT} = \tilde{P}_{LT} + P_m, \quad (2.24)$$

$$\frac{\sum_{t=1}^{N_T} \tilde{P}_{LT}(t_n)}{\sum_{t=1}^{N_T} P_{feeder}(t_n)} < R_{LT} * (1 + \varepsilon). \quad (2.25)$$

(2.23) decides which load type to select. If there are more than one load type that satisfies (2.23), FLDA will randomly select a load profile. (2.24) and (2.25) ensure that R_{LT} will not exceed the targeted load composition value by a given error margin, ε .

2.3.7 FLDA-LPS Result Evaluation Criterion

Three criteria are used for evaluating the performance of the FLDA-LPS algorithm: error in matching the feeder-head load shape (ME), error in selecting the total number of load profiles (NE), and error in meeting load composition requirements (LCE). The criteria are calculated by

$$ME = \frac{\sum_{t=1}^{T_D} \left| \frac{P_{feeder}(t) - \tilde{P}_{feeder}(t)}{P_{feeder}(t)} \right|}{T_D}, \quad (2.26)$$

$$NE = \left| \frac{N_{feeder} - \tilde{N}_{feeder}}{N_{feeder}} \right|, \quad (2.27)$$

$$LCE = \left| \frac{\sum_{t=1}^{T_D} \tilde{P}_{LT}(t)}{\sum_{t=1}^{T_D} \tilde{P}_{feeder}(t)} - R_{LT} \right|. \quad (2.28)$$

When using FLDA-LPS for load disaggregation, Monte Carlo simulations are used to identify one set of load disaggregation results that has the smallest deviations in NE from the means. The average results when conducting different number of simulations for a weekly matching case are shown in Table 2.1. It shows that the means of the ME, NE, and LCE obtained from all MC trains become stable when the number of MC trains reaches 100. Therefore, in this work, 100 trails are conducted in the Monte Carlo simulation process in order to identify the best set of load disaggregation results.

Table 2.1 LPS results with different number of simulations

	Number of simulations				
	10	50	100	500	1000
ME (%)	2.34	1.56	1.40	1.41	1.40
NE (%)	6.32	3.24	2.48	2.47	2.50
LCE (%)	0.68	0.59	0.56	0.57	0.57

2.3.8 FLDA-LPS Algorithm Summary

The implementation of the FLDA-LPS algorithm is summarized in Algorithm 1.

Algorithm 1 FLDA-LPS

- 1: Initialize the algorithm. Define the matching duration N_T for P_{feeder} , number of pivot points pairs, energy consumption ratio of each load type (R_R, R_C) and the load profiles in D (e.g., D_R, D_C).
 - 2: Discard all load profiles in D with $\max(P_m) \geq \max(S_i R_i)$.
 - 3: **procedure:** Perform Random Load Profile Selection. At each step, add the selected load profile to $D_{selected}$ and remove the selected load profile from D .
 - 4: **Procedure: RNR-LPM**
 - 5: **repeat**
 - 6: Select D_{LT} based on (2.23).
 - 7: Calculate $P_{ref}^{(u)}$ using (2.16) and find all pivot-points from $P_{ref}^{(u)}$.
 - 8: Calculate φ_m for all load profiles in D_{LT} , $\Psi = [\varphi_1, \varphi_2 \dots \varphi_{N_D}]$.
 - 9: Save all load profiles with $\varphi_m = \max(\Psi)$ in D_{LSI} .
 - 10: Random draw a load profile, P_m , from D_{LSI} .
 - 11: Apply (2.24) and (2.25) to check if the selected load profile P_m can be used. If “yes”, go to the next step; if “no”, remove the load profile from D_{LT} and go to step 8.
 - 12: $\tilde{P}_{feeder} = \tilde{P}_{feeder} + P_m$.
 - 13: Calculate e using (2.22).
 - 14: **if** e increases for the last iteration **then**
 - 15: $\tilde{P}_{feeder} = \tilde{P}_{feeder} - P_m$.
 - 16: Remove this load profile from D_{LT} and go back to step 6.
 - 17: **else**
 - 18: Add the load profile to $D_{selected}$, remove it from D , clear D_{LSI} .
 - 19: **end if**
 - 20: **until** D is empty.
 - 21: **end procedure**
-

In this algorithm, step 2 is to ensure that we will not select a load profile with very high peak load. By using the distribution transformer rating as a constraint, the selected load profile is guaranteed to have a node that it can be put in.

2.4 FLDA-LPA Algorithm

After the load profile selection step is finished, the next step is to allocate the selected load profiles to each load node.

2.4.1 Allocation based on Distribution Transformer Rating

Using (2.4) and (2.5), we can allocate the load profile in $D_{selected}$ to a load node based on the loading factor and the distribution transformer rating at that node. The detailed FLDA-LPA algorithm is illustrated as follows.

Algorithm 2 FLDA-LPA

- 1: Initialize all load node profiles to be $\tilde{P}_i = [0 \ 0 \ 0 \ \dots \ 0]$ (N_T zeros).
- 2: Initialize $i=1$, $q=1$, all N_i to be 0.
- 3: **procedure** ALLOCATE ONE LOAD PROFILE TO EACH LOAD NODE
- 4: **repeat**
- 5: Draw the load profile $P_{i,k}$ with the q^{th} highest peak load in $D_{selected}$.
- 6: **repeat**
- 7: **if** $\max(\tilde{P}_i + P_{i,k}) > S_i R_i$ **then**
- 8: $q = q + 1$.
- 9: **else**
- 10: $\tilde{P}_i = \tilde{P}_i + P_{i,k}$, $N_i = N_i + 1$, $i = i + 1$, $q = 1$.
- 11: Remove this load profile from $D_{selected}$.
- 12: **end if**
- 13: **until** $\max(\tilde{P}_i + P_{i,k}) < S_i R_i$.
- 14: **until** $i > N_L$
- 15: **end procedure**
- 16: **procedure** ALLOCATE OTHER LOAD PROFILES
- 17: $i = 1$, $f = 1$.
- 18: **repeat**
- 19: Draw the load profile $P_{i,k}$ with the highest peak load in $D_{selected}$.
- 20: **repeat**
- 21: **if** $\max(\tilde{P}_i + P_{i,k}) > S_i R_i$ **then**
- 22: $i = i + 1$, $f = f + 1$.
- 23: **else**
- 24: $\tilde{P}_i = \tilde{P}_i + P_{i,k}$, $N_i = N_i + 1$, $i = i + 1$, $f = 1$.
- 25: Remove this load profile from $D_{selected}$.
- 26: **end if**
- 27: **if** $i > N_L$ **then**
- 28: $i = 1$.
- 29: **end if**
- 30: **if** $f > N_L$ **then**
- 31: Discard this load profile and go back to find two or more load profiles in D with the aggregated peak matching the peak of the abandoned load profile. Save the newly selected load profile in $D_{selected}$.

```

32:      $f = 1$ .
33:   end if
34:   until  $\max(\tilde{P}_i + P_{i,k}) < S_i R_i$ 
35:   until  $D_{selected}$  is empty.
36: end procedure

```

In FLDA-LPA, Steps 4-15 guarantee that each load node has at least one load profile; Steps 16-36 allocate the remaining load profiles to each node; f is a flag parameter to record how many nodes the algorithm has tried but with failed allocation. When a load profile cannot be allocated to any load nodes, Steps 30-33 will discard the load profile and go back to find a few smaller loads with an aggregated load peak similar to the peak of the abandoned load profile.

2.4.2 Allocation based on Distribution Transformer Rating

If the load type and building square footage are also used for load profile allocation, in Steps 16-36 of FLDA-LPA, we will only allocate those loads that have the required load type and within the given square footage range to the node. The selection criteria considering square footage are

$$A_i = \frac{\sum_{k=1}^{N_i} A_{i,k}}{N_i}, \quad (2.29)$$

$$\Delta A_{i,m} = \left| \frac{A_i - A_m}{A_m} \right|, \quad (2.30)$$

where A_i is the average square footage per building at node i and $\Delta A_{i,m}$ is the allowable deviation from the average values. The load profile with smaller $\Delta A_{i,m}$ will be allocated at node i .

2.5 FLDA-LPS Performance Evaluation

In this section, we present the simulation setup, the performance criteria and the simulation results.

2.5.1 Simulation Setup

Thirty-minute smart meter data collected from 4302 buildings (including 3785 residential and 517 commercial) are used so D , D_R , and D_c contains 4302, 3785, and 517 sets of load profiles, respectively. The residential and commercial sample load profiles are shown in Figure. 2.6 and Figure. 2.7. Note that we didn't use the actual feeder load profiles given by the utility for evaluating the algorithm performance. Instead, each time, we randomly select 1000 load profiles from the 4302 buildings based on the given load composition requirement; then, we use the aggregated load profile of the 1000 load profiles as the feeder-head load profile. By doing so, the actual load profiles in $D_{selected}$ are known to us, making it possible to compare the FLAD-LPS selected load profiles with the actual ones to quantify NE.

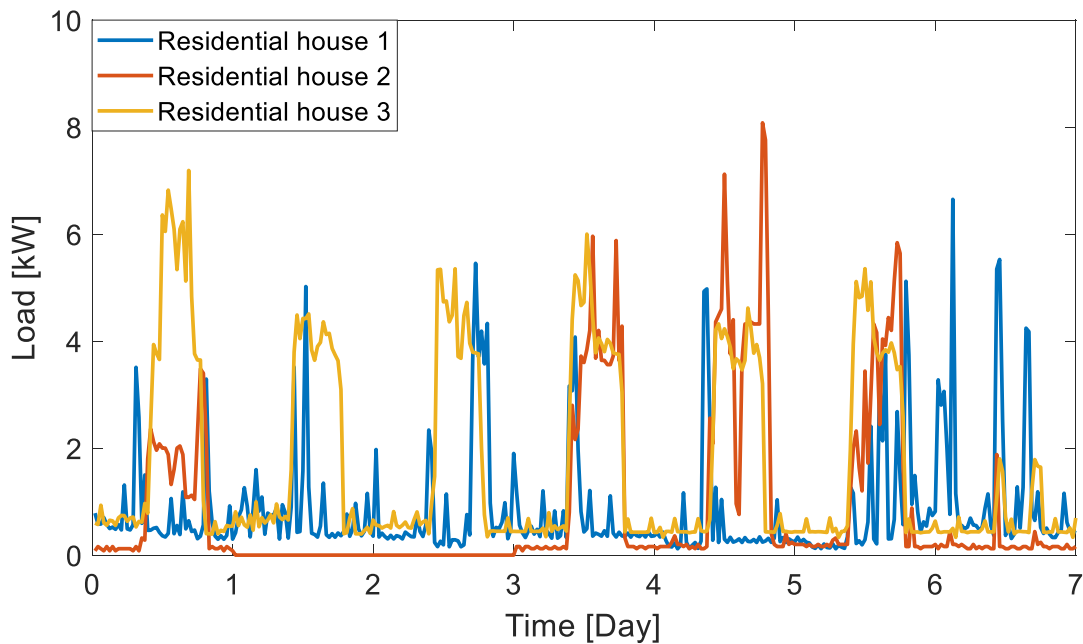


Figure. 2.6 Residential house sample load profiles

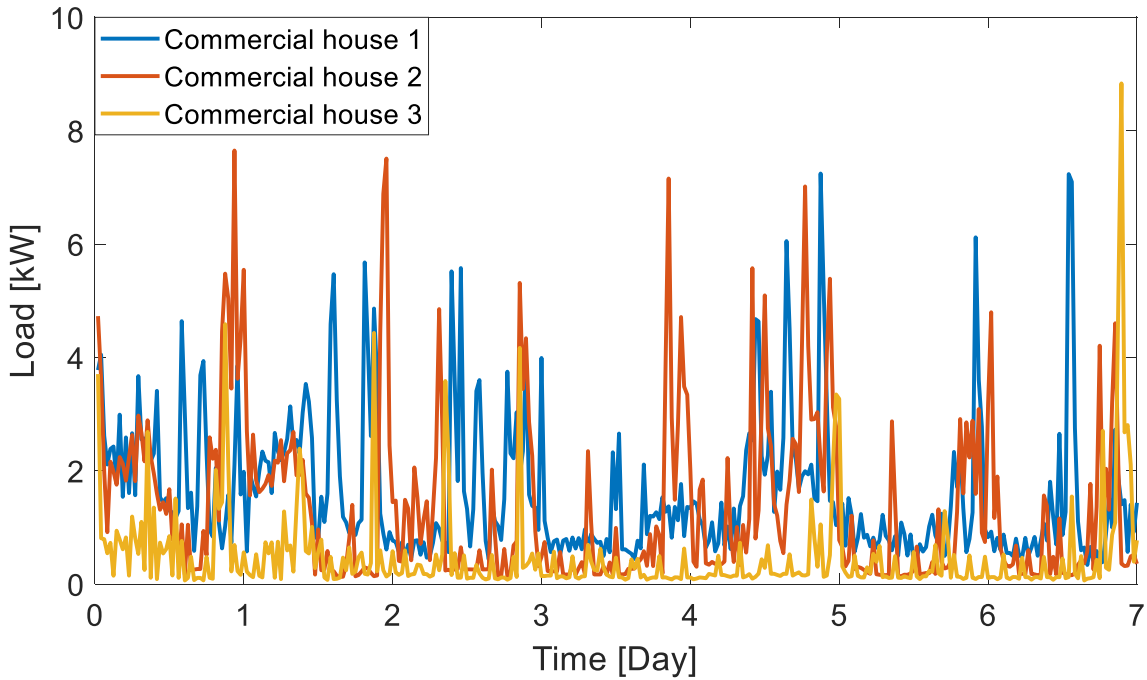


Figure. 2.7 Commercial house sample load profiles

2.5.2 Selection of the Ratio of Random Load Profiles

In the FLDA-LPS random selection procedure, R_{random} controls the level of load diversity. To evaluate the influence of R_{random} on the FLDA-LPS performance, we increase R_{random} from 10% to 100% at a 10% incremental rate and run 100 simulations using 100 weekly feeder-head load profiles for each given R_{random} .

As shown in Figure. 2.8, we observe no obvious performance degradation in ME and LCE when R_{random} varies. This is because R_{random} are selected such that the aggregated randomly selected loads will not exceed the valley of P_{feeder} . Therefore, if the peak-to-valley ratio is high for the given feeder-head load profile, the matching algorithm can always find the load profiles from D to match the difference between \tilde{P}_{random} and P_{feeder} . However, the increase in NE is noticeable. This is because there is an increase in the likelihood to select extreme cases (e.g., tendency to select smaller or larger loads) when the number of randomly selected loads increases. The increase is normally within 3%. Therefore, we conclude that R_{random} can be set to any user

desired values base on load diversity needs without causing significant deterioration in the performance of FLDA-LPS.

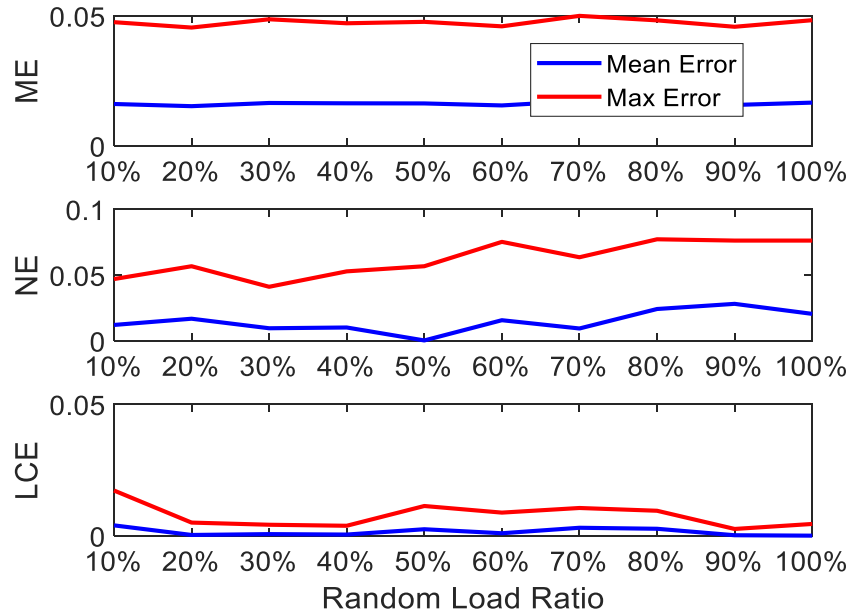


Figure. 2.8 Performance comparison using different random load ratios.

2.5.3 Selection of Pivot-points

In this section, the influence of selecting different numbers of pivot pairs on FLDA-LPS performance is evaluated. Set the random load ratios to be 50% and run each case with a given number of pivot-point pairs 100 times.

The simulation results for weekly, monthly, and yearly matching are summarized in Tables 2.2-2.4, respectively. From the results, it can be observed that at the beginning, the matching accuracy will increase when more pivot pairs are selected. However, once a certain number is passed, the accuracy starts to decrease. These results show that to avoid under- and over- fit, an optimal number of pivot pairs can be selected. In addition, when matching longer duration load profiles, *ME* will increase but *NE* will not change much. In addition, *LCE* will not vary much regardless what the matching period is or how many pivot points are selected. Therefore, when using FLDA-LPS, after the target matching period is fixed, we only need to find the best number

of pivot pairs for minimizing *ME*.

From the results shown in Tables 2.2-2.4, we suggest that

- for weekly matching: select 4-5 pairs of pivot points (i.e., the peak/valley load of 4/5 days);
- for monthly matching: select 16-24 pairs of pivot-points (i.e., the peak/valley loads of 4/5 days in each week);
- for yearly matching, select 36 pairs of pivot-points (i.e., the peak/valley load of 3 weeks in each month).

Table 2.2 Weekly matching results

	Number of Pivot Pairs						
	1	2	3	4	5	6	7
ME (%)	1.70	1.43	1.42	1.21	1.16	1.64	3.00
NE (%)	4.97	2.54	2.55	1.40	0.31	2.05	3.65
LCE (%)	0.59	0.51	0.66	0.56	0.53	0.69	0.71

Table 2.3 Monthly matching results

	Number of Pivot Pairs						
	4	8	12	16	20	24	28
ME (%)	1.83	1.74	1.58	1.54	1.49	1.55	1.61
NE (%)	3.25	3.14	2.85	2.78	2.03	3.12	3.77
LCE (%)	0.57	0.65	0.50	0.54	0.41	0.63	0.56

Table 2.4 Yearly matching results

	Number of Pivot Pairs				
	4	12	24	36	52
ME (%)	3.88	2.64	2.37	2.14	3.61
NE (%)	3.18	3.39	2.36	2.48	3.08
LCE (%)	0.62	0.65	0.68	0.58	0.50

2.5.4 Selection of Pivot-points

The performance of the proposed FLDA-LPS is evaluated for disaggregating a weekly load profile. Method 1 is the FLDA proposed in this dissertation. Method 2 is the random selection method. Step 3 in Algorithm 1 are used to randomly select the load profiles until e in (2.22) reaches its minimum value. Method 3 is choosing pivot points with (2.14) and (2.15) (RT-LPM) instead of using (2.18) and (2.19) (RNR-LPM) for load shape matching procedure. Method 4 is to use a pivot-area method instead of pivot-point for the shape matching procedure. The average energy consumption of three consecutive time steps are calculated and used for the load profile selection. Method 5 is to use an optimization method for load profile selection, which is formulated as,

$$\min \sum_{t=1}^{T_D} |P_{feeder}(t) - \tilde{P}_{feeder}(t)| \quad (2.31a)$$

$$\text{s.t.: } \tilde{P}_{feeder} = \sum_{m=1}^{N_D} (s(m) * P_m), \quad (2.31b)$$

$$s(m) = 0, 1, \quad (2.31c)$$

where $s(m)$ is a decision variable representing whether load profile m is selected or not.

In the comparison, for Method 1 and 2 we use the mean value obtained by Monte Carlo simulations. The random load ratio was selected as 50% and 5 pairs of pivot-points were selected. For Method 5, GAMS is used to solve the problem. Because LCE in FLDA-LPS is consistently small and negligible, it is not selected as a comparison criterion.

As shown in Table 2.5, the performance of FLDA-LPS is the best. Both *ME* and *NE* indices of other methods are worse than FLDA-LPS.

Table 2.5 Performance comparison

	Method				
	FLDA	Random	RT-LPM	Pivot-area	GAMS
ME (%)	1.16	4.68	1.98	2.37	2.39
NE (%)	0.31	16.22	7.06	2.54	6.2

2.5.5 Performance using different Load Profile Database

This sub-section compares the performance of FLDA-LPS when using different load profile databases. In Case 1, a load profile database from the same area (i.e., 4302 load profiles in North Carolina) as the feeder is used. In Case 2, a load profile database of a different area (i.e., 1500 load profiles in Texas) is used [74]. The parameters are chosen to be same for the two cases, i.e., conducting weekly load profile matching using 5 pairs of pivot-points with R_{rd} at 50%.

Run each case 100 times. As shown in Figure. 2.9, as expected, *ME* is much smaller when using the North Carolina database. This is because the load characteristics are different for even the same type of loads in the two areas. This case shows that the expected errors when using load profiles collected from areas with different load patterns.

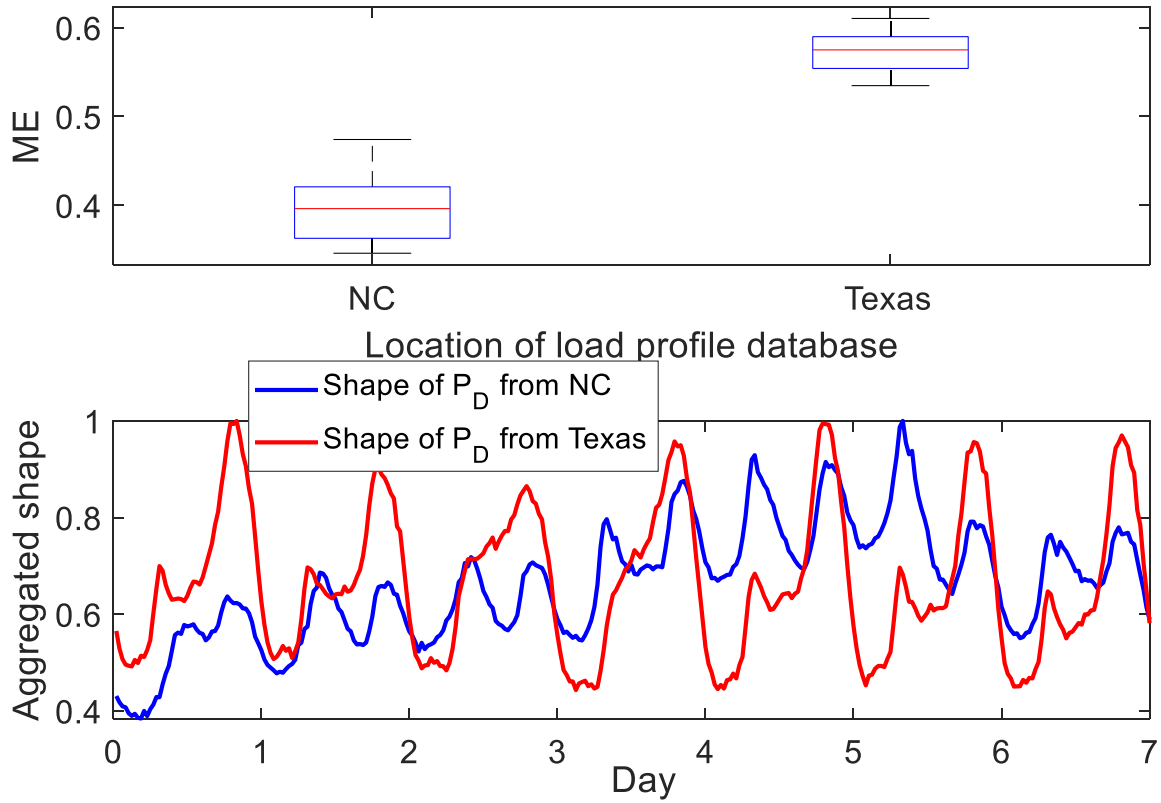


Figure. 2.9 Performance comparison using two different load profile databases

2.6 FLDA-LPA Performance Evaluation

To compare the FLDA-LPA method, we first run FLDA-LPS to select the load profiles by matching the actual, monthly feeder-head load profile of a Duke Energy distribution feeder. Actual ratings of 421 distribution transformers on that feeder are used as an input of FLDA-LPS. Set the peak of the node-level load profile to be less than 80% of the transformer rating. Run FLDA-LPS for 100 times and compare the obtained 100 sets of $D_{selected}$ to select one set of parameters with the minimum ME and $N_{selected}$ closest to the mean. The weighting between the two criteria is 50% for each. Thus, 1295 houses are selected. The results of FLDA-LPA are shown in Figs 2.10-2.12.

As shown in Figure. 2.10, the first subplot shows that the shape of P_{feeder} and \tilde{P}_{feeder} are very close with peaks and valleys closely captured. The second subplot shows some example nodal load profiles has significant load diversity. Even for nodes with the same distribution transformer rating, the shapes of the nodal load profiles are different. This will make the distribution system planning study more realistic than using one or a few typical load profiles.

The transformer maximum loading ratio, the number of buildings allocated to, and the load compositions for different transformer size are shown in Figure. 2.11. The transformer loading levels are within expected range. The number of houses allocated to each node are reasonable. The load compositions are consistent with the expectation of the load composition in the given service area which are verified by Duke Energy customer information data. Note that commercial building loads have a higher chance to be allocated to transformers with higher ratings due to the transformer loading ratio constraints.

Figure. 2.12 shows the distribution transformer loading ratios distribution for 421 transformers in a typical day. The boxplot shows that the proposed load disaggregation method will let different transformers have non-coincident load peaks and valleys, making the study results more realistic.

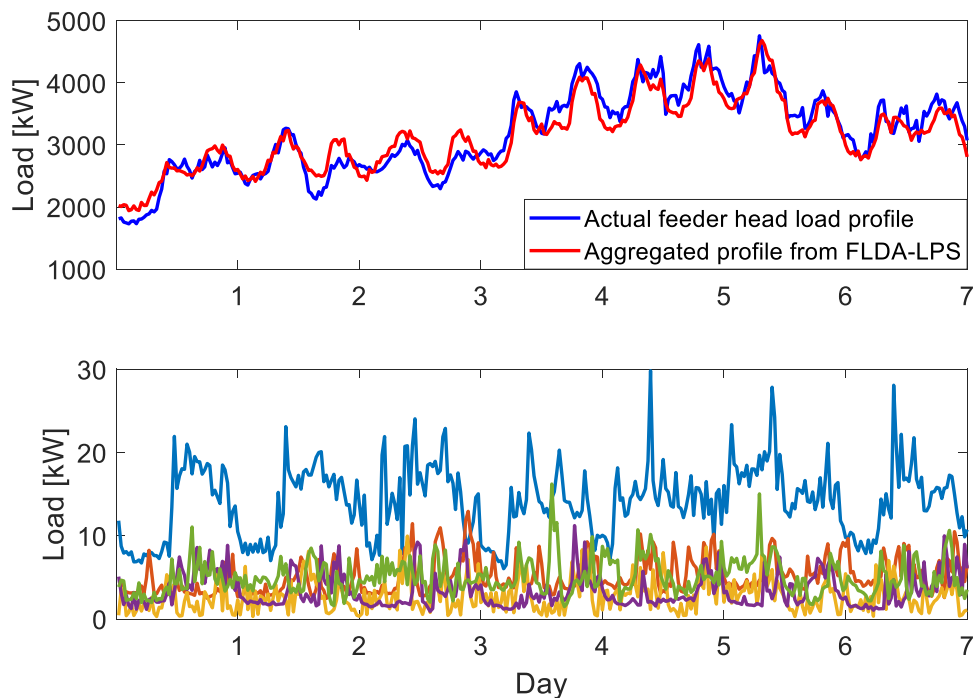


Figure. 2.10 An example load disaggregation result

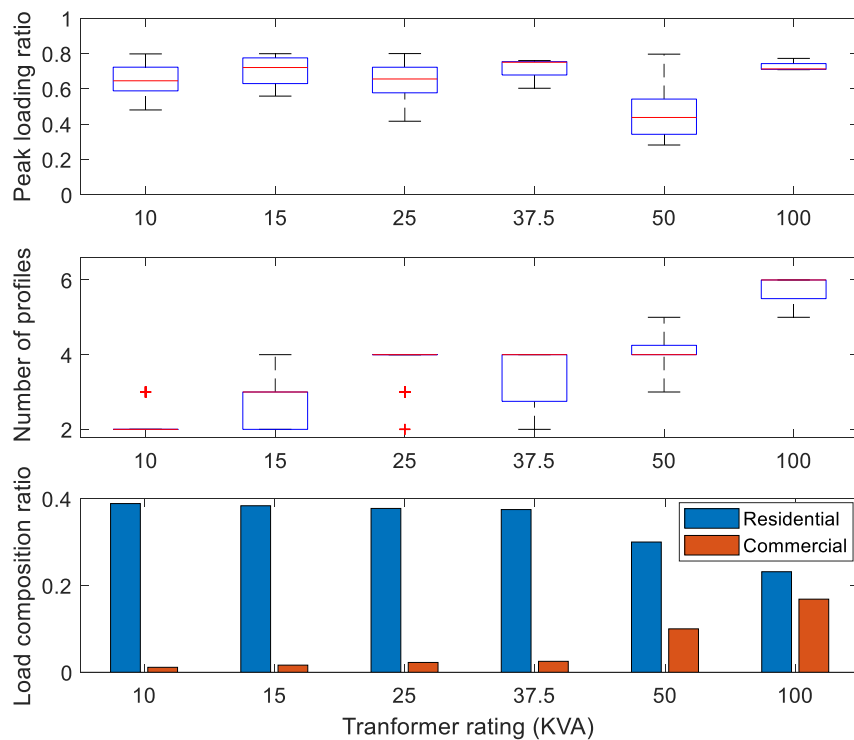


Figure. 2.11 LPA results for different transformer sizes

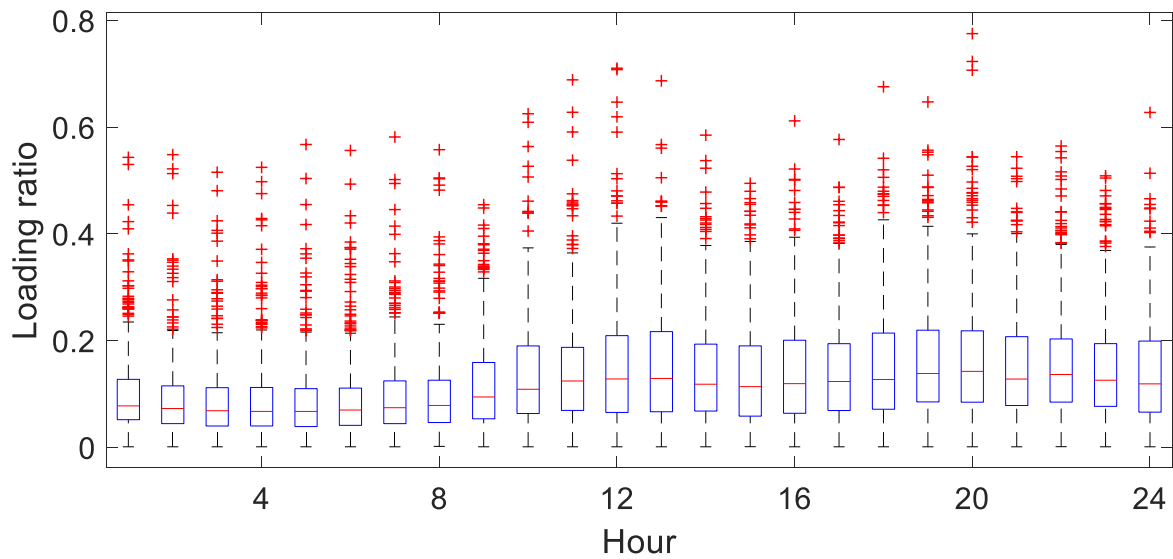


Figure. 2.12 Transformer loading ratios in an example day.

2.7 Power Flow Results Comparison

This subsection presents the power flow results. Voltage profiles from the FLDA method is compared with the OLSS method when running a monthly quasi-static time-series simulation using OpenDSS. Power flow studies are conducted for the three cases so that the voltage errors between the OLSS and the base case are compared with the voltage errors between the FLDA and the base case.

To compare the impact of using different load shapes at each load node on feeder load profile, we disabled all voltage regulators in the feeder during simulation. We run a 31-day simulation with half-hour data resolution. The distribution feeder we used is the same as the one we used in section 2.3.2. The feeder topology is shown in Figure. 2.13. With FLDA, we generated load profiles for each load node, and compared with the case that every node shares the same load shape. After that, 1488 power flow runs are conducted to obtain the voltage profiles at each node for the 31-day period.

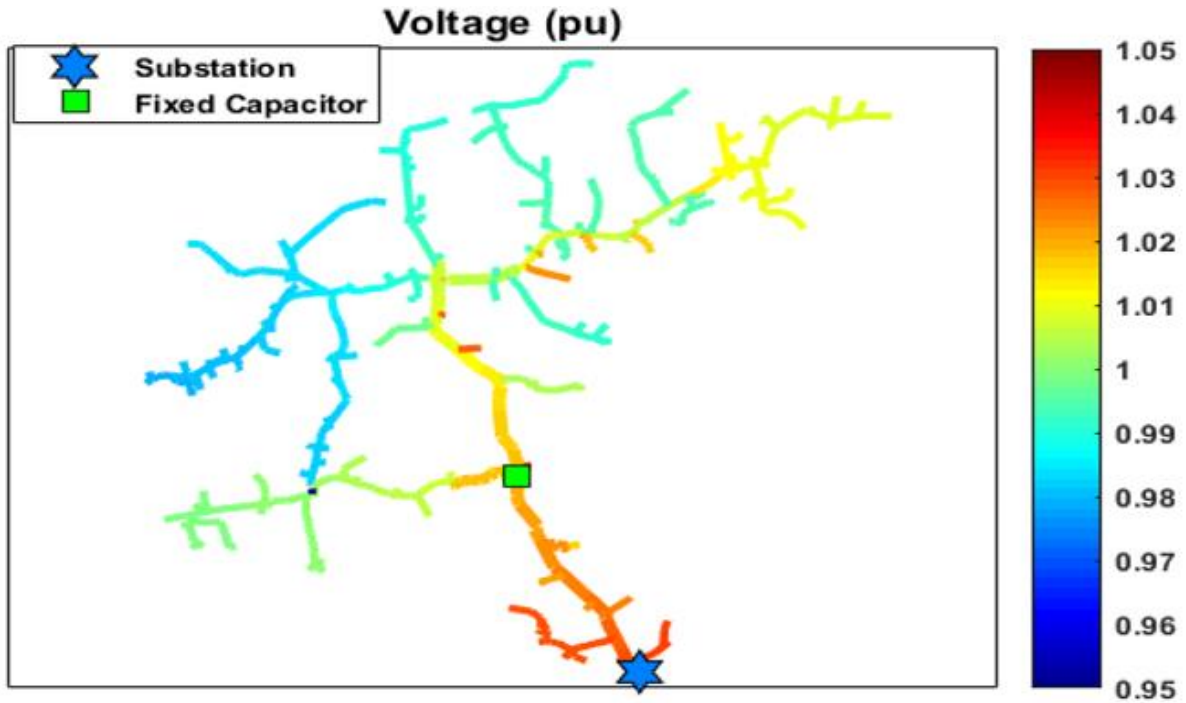


Figure. 2.13 Topology of the distribution feeder

To compare the differences between the simulation results obtained by the two methods, we compared the two load shapes by calculating the average voltage difference percentage for node i , PCT_i , using

$$PCT_i = \frac{\sum_{t=1}^{1488} |V_i^d(t) - V_i^u(t)|}{1488 V_i^d(t)} \times 100\%, \quad (2.32)$$

$$i \in \{1, 2, \dots, N\}$$

where $V_i^d(t)$ and $V_i^u(t)$ are the voltage calculated at node i using FLDA and OLSS method, respectively.

The PCT_i versus the distance from feeder head to each node is plotted in Figure. 2.14. The results show that the average voltage differences are getting larger and larger as the nodes are further away from the feeder head. The largest difference is 78 V on a between the results obtained

by the two methods. The location is at the feeder end of phase B. Phase A has the smallest voltage difference at the feeder end and it is still 24 V.

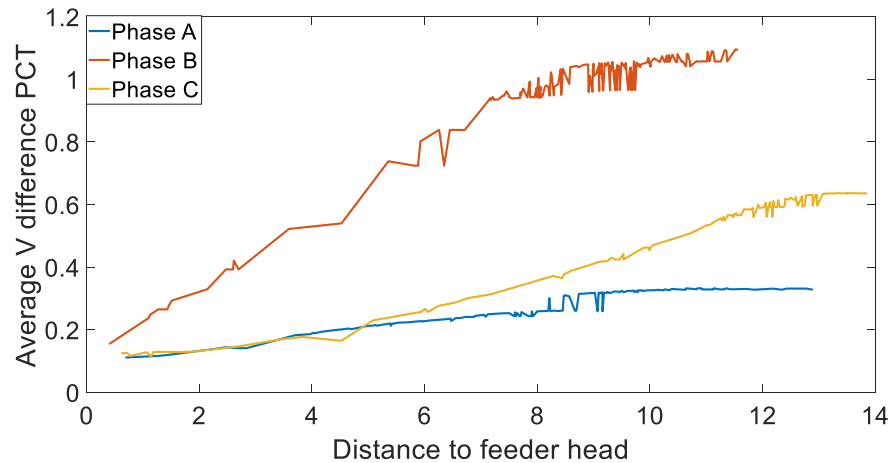


Figure. 2.14 Voltage difference percentage for three phases

Note that the data resolution is 30-minute in this study, so the voltage difference is underrated because the average power variation is much larger for 15-minute data or for data with even smaller resolution. This shows that the voltage difference is at least 3-5 times bigger if minute-by-minute data is used.

Figure. 2.15 is the boxplot showing the distribution of the voltage differences at different time-of-the-day for all nodes. In general, the voltage difference during daytime is larger as the power consumption is higher.

From the preliminary results, we observed that it is important to model each node using realistic load shapes. If the same load shape is applied to each node, the modeling of voltage and power flow will differ from the actual cases, especially for the peak loading conditions and for nodes at feeder end.

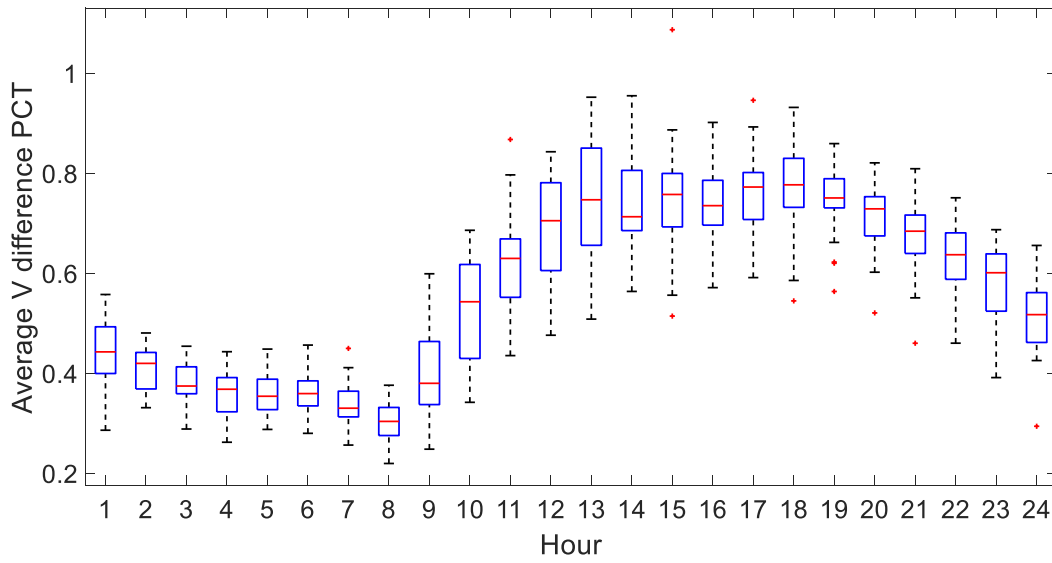


Figure. 2.15 Boxplot of voltage difference at different time

A comparison between using OLSS and FLDA to conduct time-series power flow analysis is shown in Figure. 2.16. In the base case, 1000 load profiles are selected and assigned to each node based on the distribution transformer rating at that node. Then, using the aggregated load profile as the feeder top load profile, we use the proposed method to find load profiles and assign them to each node as the FLDA case. We use the shape of the aggregated load profile to allocate to each node a profile using the OLSS method as the OLSS case. The voltage error boundary results are shown in Figure. 2.16, where the two blue lines are the upper and lower bounds of the voltage errors for all load nodes using the OLSS approach and the two red lines are the upper and lower bounds of the voltage errors when using the FLDA approach. It can be observed that using the FLDA approach, the voltage profile at each node is closer to the actual compared with using the OLSS approach.

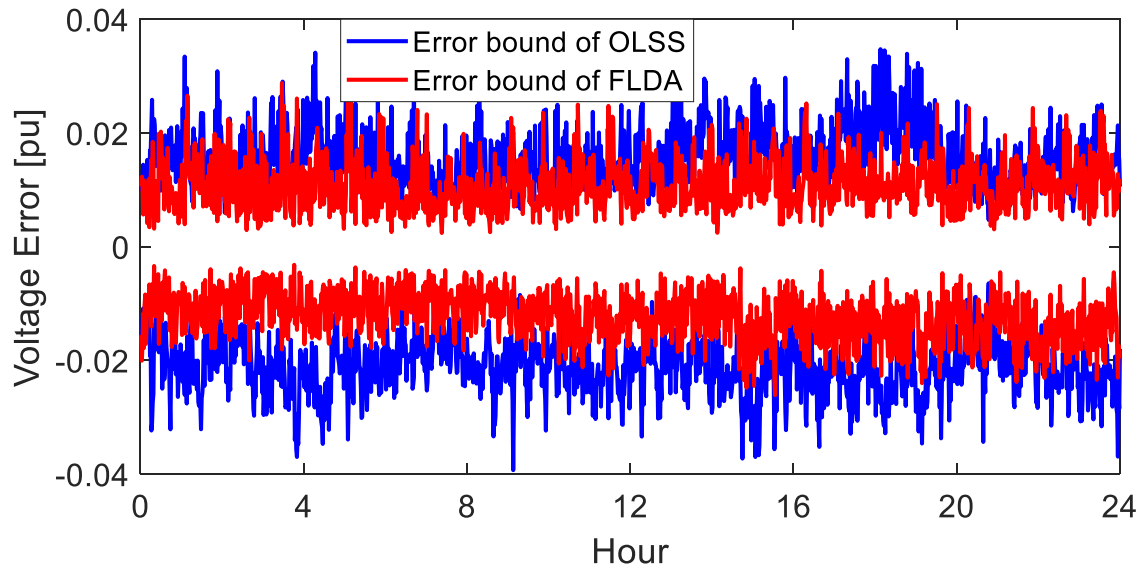


Figure. 2.16 Nodal voltage error distributions

In addition, as shown in Figure. 2.17, the graphic user interface (GUI) tool for FLDA is developed to help users doing this kind of modeling. With this tool, users can simply upload the target feeder head load profile, target ratio of each load type, target random load ratio, feeder node information and the available load pool. Then this tool will generate the load profile of each load node and the location of each house.

After the load profiles of each node are generated, the QSTS power flow analysis can be simulated with another distribution feeder planning tool. The GUI of this tool is shown in Figure. 2.18. Many kinds of studies such as, the impact of demand response, zero net energy (ZNE) house and electric vehicle can be conducted with this tool [73]. User can select the node in this feeder and the load profile and voltage profile will be shown. With this tool users can get a overview that how different cases will influence the daily/weekly/yearly load and voltage profiles.

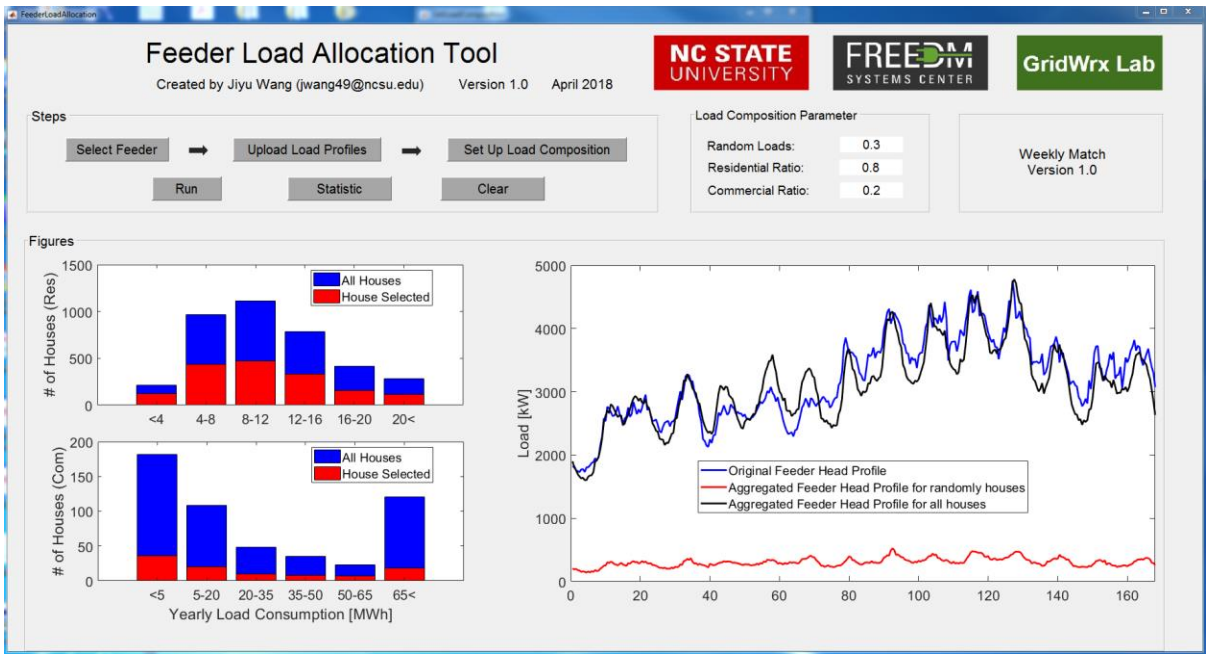


Figure. 2.17 Graphic user interface of FLDA

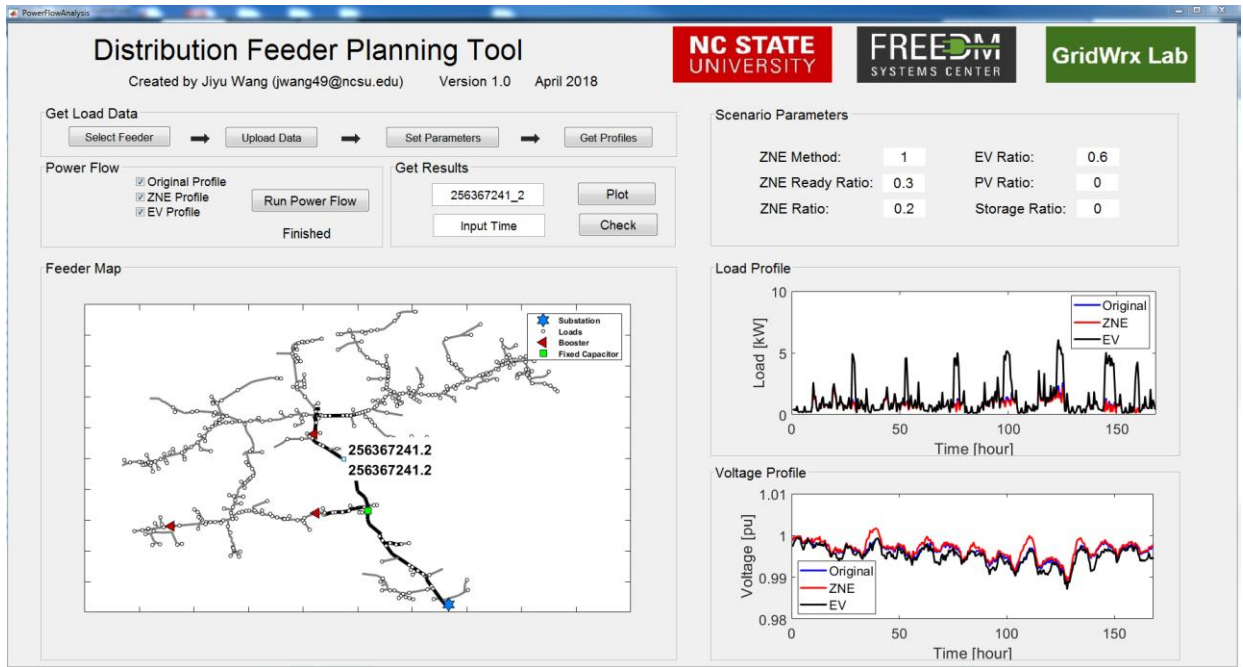


Figure. 2.18 Graphic user interface of distribution feeder planning tool

2.8 Other FLDA methods

The FLDA method introduced above is for the case when feeder head load profile and distribution transformer ratings are available. However, sometimes we may not know all the information. This subsection presents other two feeder load disaggregation algorithms when only partial information is available.

2.8.1 With nodal peak load

For some distribution feeders, we may not have its feeder head load profile. However, the peak load at each load node sometimes are available. For example, for the IEEE-123 test system, the nodal peak loads are provided. To model a group of diversified load profiles at each load node, we developed a FLDA algorithm with nodal peak load (FLDA-NPL). In the IEEE-123 feeder model (as shown in Figure. 2.19), the number of load nodes, N_L , is 91. In the data sheet, the peak load L_i at load node i , is given. Thus, the main goal of this algorithm is to select the load profiles from the load profile database to match peak load, L_i . The load profiles are constructed using the actual load data collected in PECAN Street project [74]. The time resolution of this dataset is 1-minute. The objective function of FLDA-NPL is:

$$1.05 \times L_i \geq \max_{k \in \{1, \dots, N_i\}} \left(\sum_{k=1}^{N_i} P_{i,k} \right) > 0.95 \times L_i \quad (3.33)$$

$$k \in \{1, \dots, N_i\} \quad i \in \{1, \dots, N_L\}$$

N_L : Number of load nodes in the whole feeder

L_i : Peak load at i^{th} load node (Original feeder information)

N_i : Number of houses at node i

$P_{i,k}$: Daily load profile of house k at node i

We randomly select $P_{i,k}$ from our load profile database, which contains 900 1-minute residential load profiles. By aggregating the load profiles until the peak of the aggregated load profile exceeds the given peak load value, we can obtain the number of homes at the node as well as a diversified group of residential loads. The detailed FLDA-NPL algorithm is described in Algorithm 3.

Before applying the results of the FLDA-NPL algorithm on the IEEE-123 bus system, a validation test is conducted to quantify the variability of the results. A Monte Carlo simulation is conducted to estimate the difference in results caused by selecting different load profiles for meeting the same peak load at a load node. We run FLDA-NPL 100 times when L_i is 40 kW, 80 kW, 120 kW, 160 kW, and 200 kW, respectively. Figure. 2.20 shows that the probability distribution of the number of houses for each case. Note that with different values of L_i , the interquartile range is stable approximately between 2 and 3. In our simulation, as the PV integration capacity is determined by the number of houses at each node, the stability of the number of houses is very important. This result demonstrates that with different target values, the number of houses generated in each FLDA-NPL simulation is fairly stable.

Algorithm 3 FLDA-NPL

- 1: Process the load data downloaded from the PECAN Street website and construct two load profile databases for each season—one for workdays and another for the weekend.
 - 2: Select the load profile database, $D_{a,b}$ (a represents the season and b represents weekday/weekend), to use in the LPA based on simulation requirement.
 - 3: For node i , preset its daily load profile to be $P_i=[0\ 0\ 0\ \dots\ 0]$ (all zeros).
 - 4: Randomly draw a load profile, $P_{i,k}$, from $D_{a,b}$, and add it to P_i such that $P_i = P_i + P_{i,k}$.
 - 5: Calculate the aggregated daily peak load value of node i from P_i , $P_i^{peak} = \max[P_i(t)]$, $t = 1, 2 \dots 1440$ minutes.
Check to see if the aggregated peak load, P_i^{peak} , reaches the acceptable error
 - 6: limit based on (3.33). If “yes”, go to step 7; if “no”, go to Step 4. If $P_i^{peak} > 1.05 \times L_i$, discard the data and go to Step 3.
 - 7: Record the number of houses at this load node N_i and the aggregated daily load profile P_i at this load node.
 - 8: Go to step 3 and repeat the process for all the load nodes in this feeder.
-

Aside from the stability of the number of houses, the shape variation of the aggregated load also is very important. If the load shape varies significantly in each simulation, the power flow result will not be representative. Figure. 2.21 shows a comparison of two cases when $L_i = 200$ kW: run FLDA-NPL for 10 times and 100 times. Results show that the aggregated load bears similar load shapes with one load peak occurring in the evening. The lightest load condition occurs in the early morning.

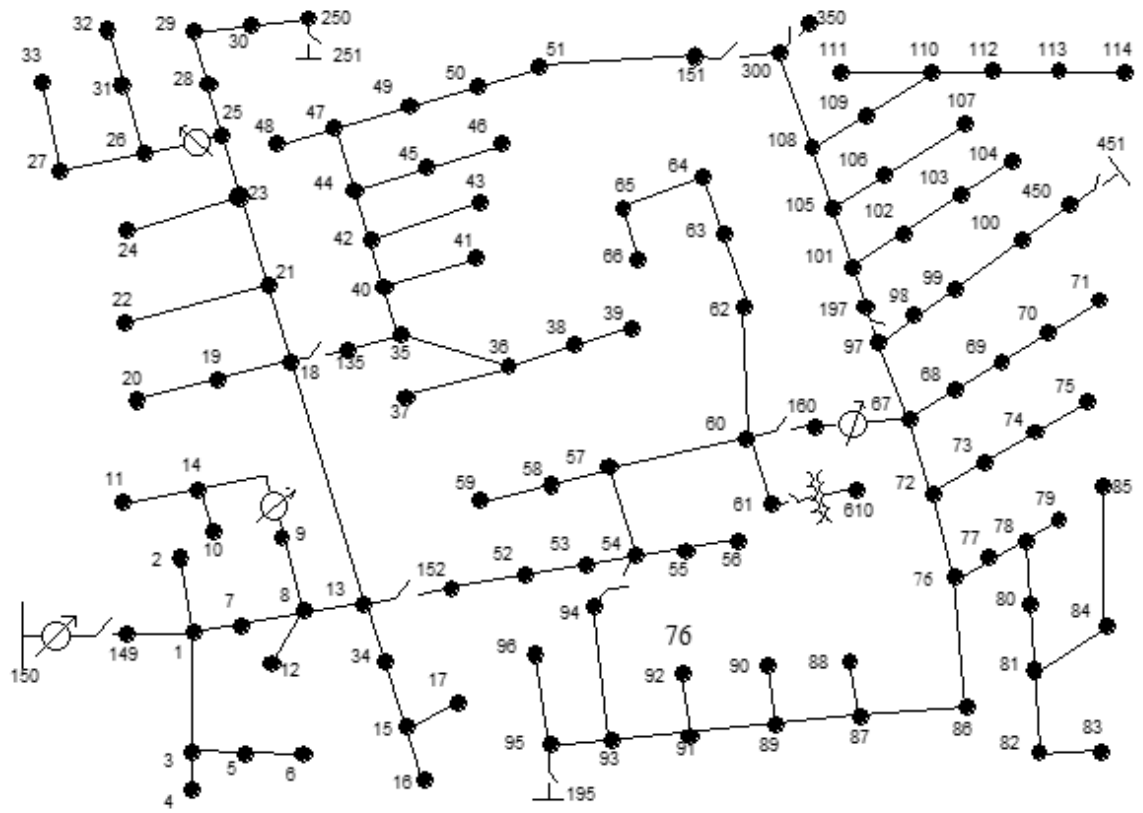


Figure. 2.19 Topology of IEEE-123 test system

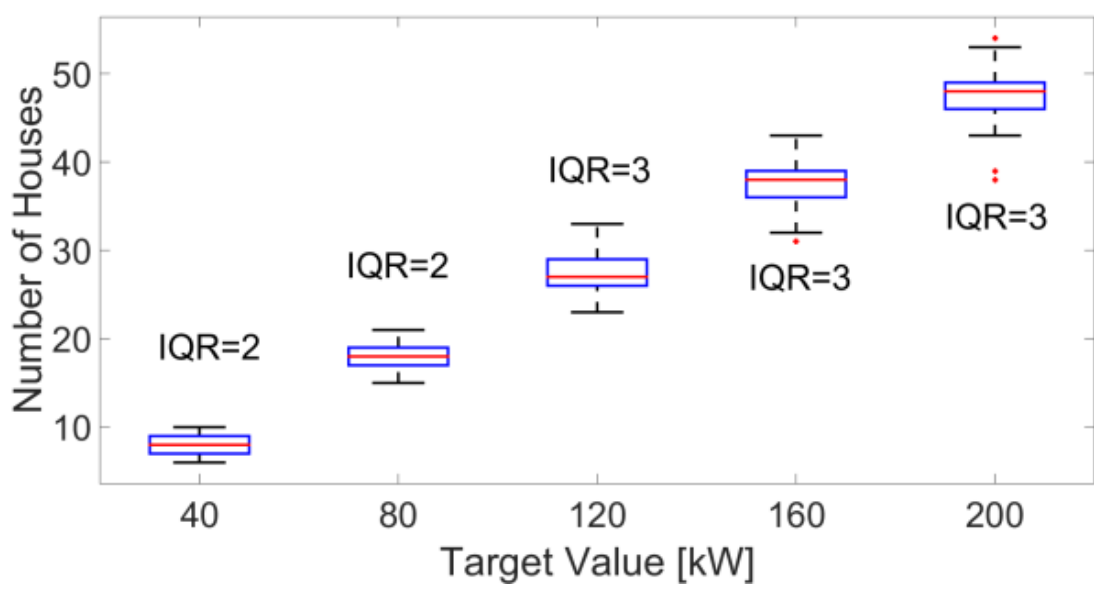


Figure. 2.20 Boxplot of the number of houses calculated for different L_i

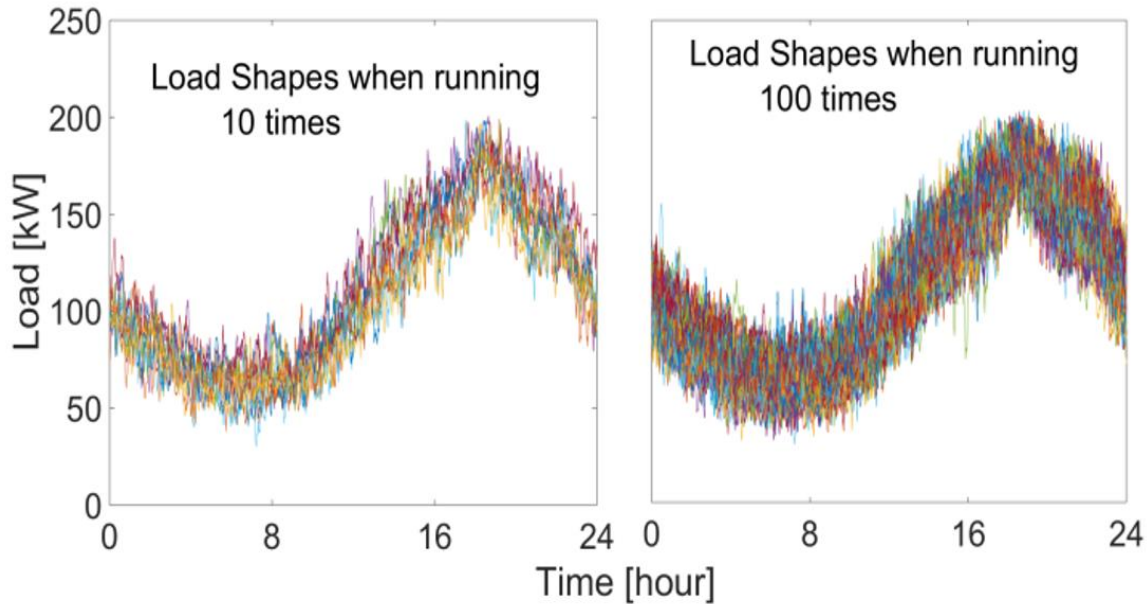


Figure. 2.21 Aggregated Load shapes obtained for $L_i = 200$ kW

Figure. 2.22 shows an example of the aggregated load at one load node. Because the PECAN Street data are minute-by-minute data, the aggregated load reflects load variations and daily load profile changes. This allows us to model the combined impact of PV and load variations so that the voltage variations along the distribution feeder can be modeled in detail. In addition, as we now have the number of homes at each load node, we can integrate roof-top PV per house. This will avoid over- or under-estimates of PV installation capacities along the feeder. It is worthwhile to mention that those additional considerations are important for modeling the correlation among loads in the same geographical areas. A summary of load information for the IEEE-123 bus system is shown in Table 2.6. On average, there are eight houses per load node, and each house will have a proximately 3.6 kW peak loads in this specific case. Note that this information can vary based on which season and type of days selected for conducting the study.

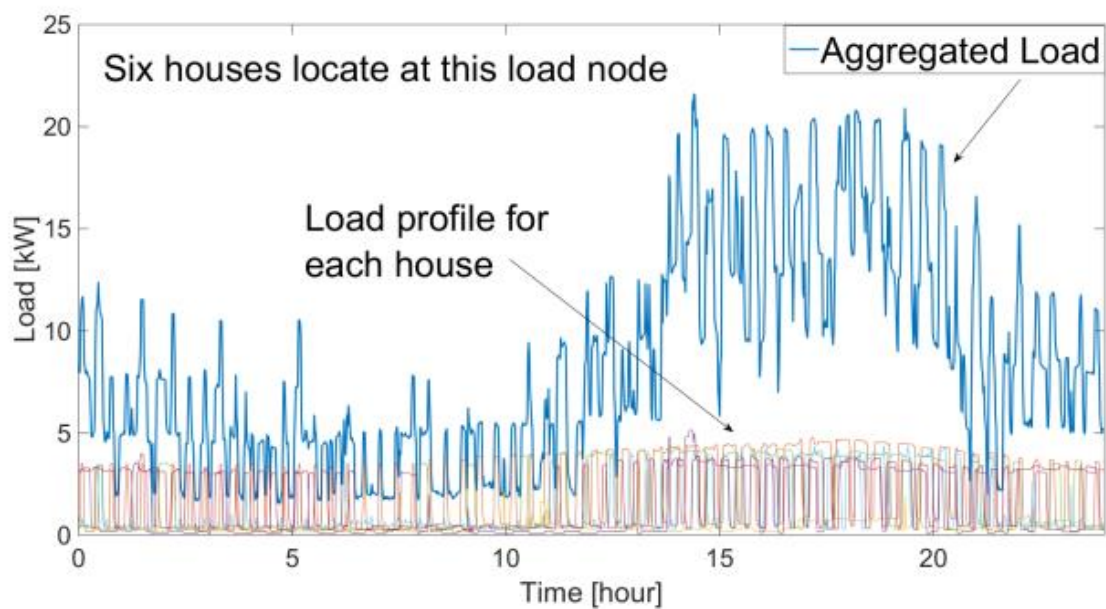


Figure. 2.22 Load profile aggregation result at one load node

Table 2.6 Feeder information

Feeder name	IEEE-123 bus system
Total Number of load nodes	91
Peak load (kW)	2785.7
Total Number of houses	773
Average house/node	8.5
Average kw/house	3.6

2.8.2 With feeder head peak load

Sometimes although the feeder head load profile is not available to researchers, electric utilities may provide the peak and valley load consumption during a period of time at feeder head. This information can be used for feeder load disaggregation as well. Similar to FLDA, in the first

step, we will select the combination of the residential and commercial load profiles that can provide a best match to the feeder head load profiles.

An actual 12.47 kV distribution feeder is used in this study. The feeder has 995 nodes in total, within which, there are 454 load nodes. There are four voltage regulators and one 3-phase shunt capacitor with a capacity of 400 kvar. A set of metered feeder head load profiles are given with one-hour resolution collected from Jan 1st, 2016 to Dec 31st, 2016.

Smart meter data collected from 5000 houses locate in the same state as the distribution feeder located are used to build the load profile database. The data resolution is 30-minute and the data were collected from Sep, 2015 to May, 2017. The loads include both residential and commercial.

A multi-pivot-points matching (MPPM) method is used to find the load profiles from the load profile database so that the aggregated load profile matches the feeder head load profile.

Because the peak load is usually the most important point in the 48 points on the feeder head load profile, the single-pivot-point matching (SPPM) method uses the peak load point, $(P_{feeder}^{peak}, t_{feeder}^{peak})$, as the pivot. The matching criterion are

$$P_{feeder}^{agg}(t = t_{feeder}^{peak}) = \sum_{i=1}^N P_i(t = t_{feeder}^{peak}) \quad (3.34)$$

$$(1 + k) \geq \frac{P_{feeder}^{agg}}{P_{feeder}^{peak}} \geq (1 - k) \quad (3.35)$$

$$\max(\sum_{i=1}^N P_i(t = 1), \dots, \sum_{i=1}^N P_i(t = 48)) = P_{feeder}^{aggpeak} \quad (3.36)$$

$$(1 + k) \geq \frac{P_{feeder}^{agg}(t=t_{feeder}^{peak})}{P_{feeder}^{aggpeak}} \geq (1 - k) \quad (3.37)$$

$$i \in \{1, \dots, N\}$$

where

N : Number of loads in this feeder

P_i : Load profile of house i on the selected day

k : Error bound (a typical value of k is 0.001)

$P_{feeder}^{aggpeak}$: Peak of the simulated feeder head load profile

P_{feeder}^{agg} : Aggregated load profile

P_{feeder}^{peak} : Peak of the actual feeder head load

t_{feeder}^{peak} : Load peaking time of the actual feeder head load

Note that criterion (3.36) and (3.37) are used to guarantee the simulated feeder head profile is peaked at t_{feeder}^{peak} . For a non-peak pivot point, the matching criterion are simply

$$P_{feeder}^{agg}(t_{feeder}^j) = \sum_{i=1}^N P_i(t = t_{feeder}^j) \quad (3.38)$$

$$(1 + k) \geq \frac{P_{feeder}^{agg}}{P_{feeder}^j} \geq (1 - k) \quad (3.39)$$

A match is not reached if $\frac{P_{feeder}^{agg}}{P_{feeder}^j} > (1 + k)$.

The aggregation algorithm for the MPPM method is shown in Algorithm 4.

By aggregating the load profiles until the error between the peak of the aggregated load profile and metered data reaches the acceptable limit, we can obtain the number of houses in this feeder as well as a diversified group of loads.

Algorithm 4 MPPM Algorithm

- 1: Construct a load profile database using 5000 smart meter data collected in the same geographical area as the distribution feeder located.
 - 2: Select the pivot feeder head load profile to match. For example, we selected the metered feeder head load profile in the j^{th} day to be the target load profile to match.
 - 3: Select m pivot points on the pivot load profile for matching and one of the pivot point is the peak load of the day. So we have m pairs of non- peak pivot points $(P_{feeder}^j, t_{feeder}^j)$ with $j \in \{1, \dots, m\}$ and one peak load point $(P_{feeder}^{peak}, t_{feeder}^{peak})$.
 - 4: Match the peak load point using (3.34)-(3.37).
for $i = 1: 5000$
 Randomly select $(P_{load}^i, t_{feeder}^j)$ from the load database.
 Use (3.34)-(3.37) to check the match. If a match is reached, keep all the load profiles and end the iteration. If a match is not reached, repeat the process.
end
 - 5: Check to see if the other non-peak load pivot points matches using (3.38)-(3.39). If “yes”, end the process. If “no”, repeat Step 4.
-

A few rules reflecting the feeder characteristics are set to guarantee that a good match can be achieved. This requires a statistic analysis of the typical distribution feeder in the area. For example, a maximum number of large load rule is in placed to limit the number of large load (defined by $P_{largeload}^{Lowlim} \leq P_{largeload}^i \leq P_{largeload}^{Highlim}$) being selected to $N_{largeload}^{Max}$. This rule selects large houses based on the number of large load nodes on the feeder to make sure only a limited number of large loads are selected and can be placed to those nodes.

On the feeder we selected for illustrate the method in this paper, there is only one load node with a distribution transformer capacity greater than 25 kVA. Thus, we set $20 \leq P_{largeload}^j \leq 25$ and $N_{largeload} = 1$. For the other loads, we let $P_{load}^j \leq 20$. Thus, we only select one house that has a maximum power between 20-25 kW. This constraint is used to make sure that that the aggregated energy consumption for each load node is smaller than the distribution transformer rating.

After each valid matching, a group of load profiles is obtained, so we need to estimate which group of profiles can provide a best overall match. We ran the algorithm 100 times for matching a daily feeder head load profile. The number of houses selected at each run is summarized in Figure. 2.23. The mean number is 551, the maximum number 649 and the minimum number is 455. Although the number of houses varies in each iteration, extreme conditions where too many small or large houses are selected can be excluded.

Figure. 2.24 shows the boxplot of the simulation results when we select 7 daily profiles and for each profile, we run the algorithm for 100 to receive 100 successful matching load groups. For most of the days, the mean number of loads selected is 551. The actual number of loads on the feeder is 590. The difference is approximately 6%. This difference can be further reduced if we limit the number of big loads being selected. Note that because the load database consists of house in the general area but not exactly the load supplied by this particular distribution feeder, it is impossible to achieve 100% match.

The next step is to decide which load groups provide a better match for all seven daily load profiles. The average error, AE , and the average absolute error, AAE , are calculated as

$$AE = \frac{\sum_{day=1}^7 \left(\sum_{t=1}^{24} \frac{P_{feeder}^{actual}(day,t) - P_{feeder}^{agg}(day,t)}{P_{feeder}^{actual}(t)} \right)}{7 \times 24} \quad (3.40)$$

$$AAE = \frac{\sum_{day=1}^7 \left(\sum_{t=1}^{24} \frac{|P_{feeder}^{actual}(day,t) - P_{feeder}^{agg}(day,t)|}{P_{feeder}^{actual}(t)} \right)}{7 \times 24} \quad (3.41)$$

All load groups resulting a total number of loads between 540 and 560 are selected. Their aggregated load profiles are compared with the other six daily profiles. The load group with the lowest AE and AAE values are selected. This load group consists of 552 houses and the

aggregated load profile in one week is plotted in Figure. 2.25. The matching day is Day 5 with 3 pivot points, and it can be observed that the two profiles in that day has the best match. In other days although sometimes there will be a difference but the overall weekly shape is the same. Table 2.7 summarizes the comparison results with the actual feeder head loads in seven days.

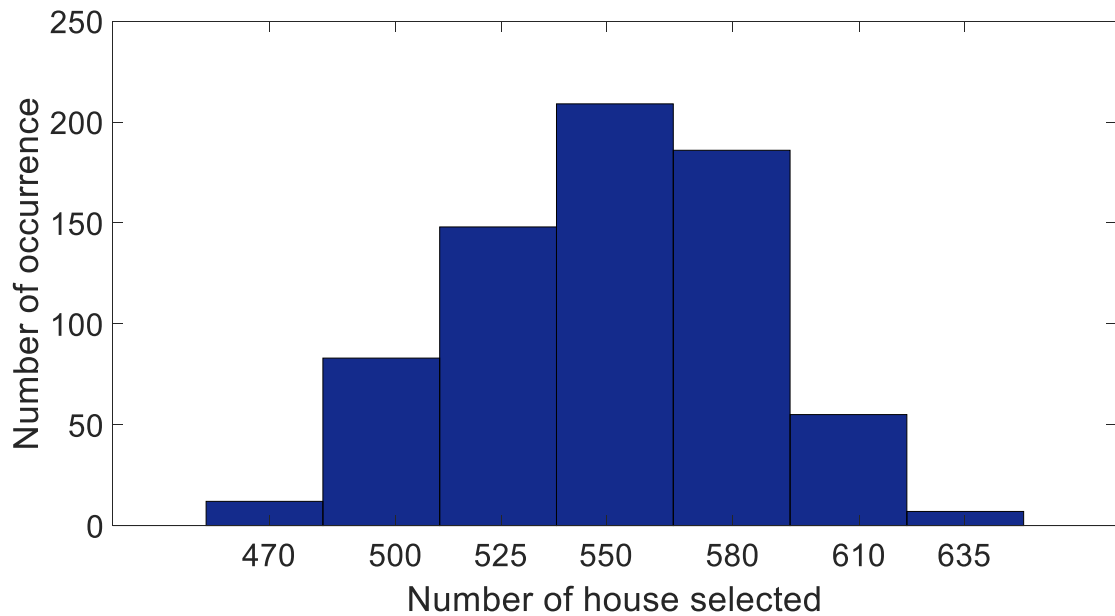


Figure. 2.23 Histogram for number of houses for 100 simulations in one day

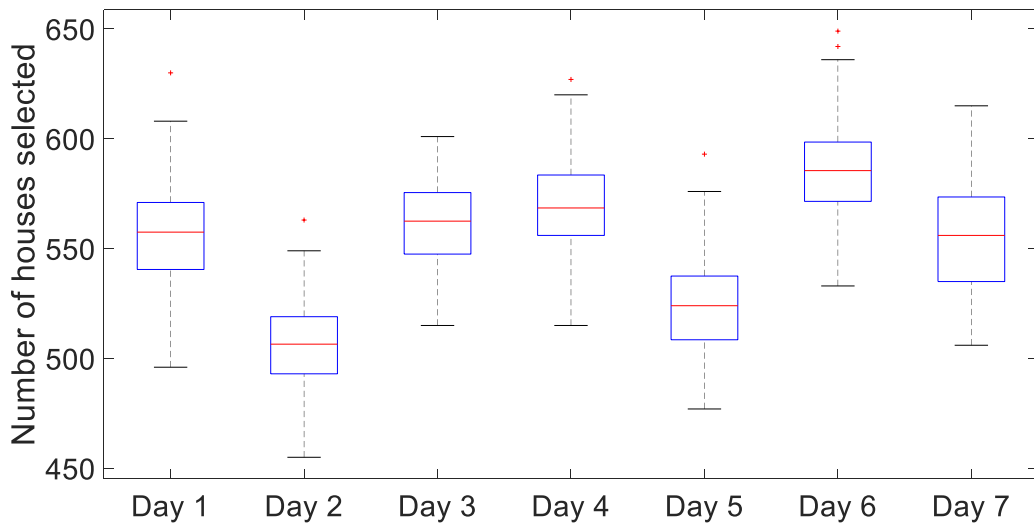


Figure. 2.24 Boxplot for number of houses in seven days

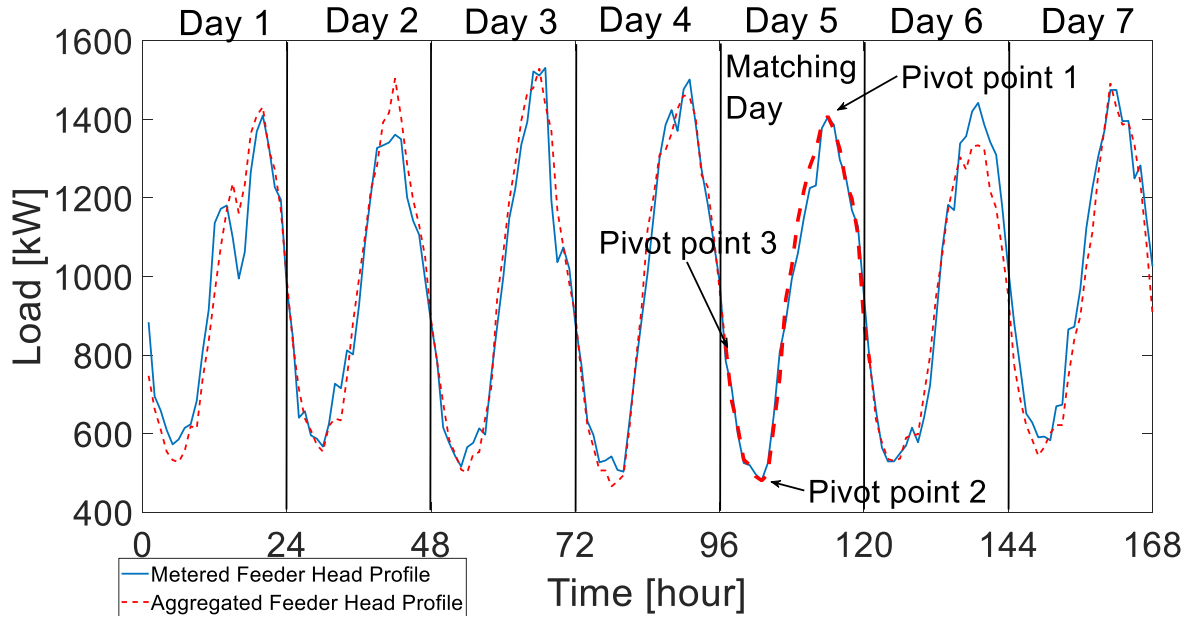


Figure. 2.25 Feeder head profile comparison

Table 2.7 Feeder head profile aggregation summary

Average Error	0.88%
Average Absolute Error	5.21%
Peak Load	1406.2 kW
Peak load Error	0.094%
Total Number of houses	552

After selecting these buildings, the next step is to allocate them down to each load node.

This part the algorithm is the same as FLDA-LPA.

2.9 Conclusions

In order to conduct distribution system quasi-static time-series analysis in an accurate way, one key aspect is modeling the load in distribution feeder more realistic. In this section, we proposed a feeder load disaggregation algorithm to use house-level smart meter data and information from actual feeder generating a unique load profile for each load node. Moreover, this

algorithm ensures the aggregated load profile of all the nodes in feeder matches the actual metered feeder head load profile. If the load type ratio or square footage information are available, they will be taken into account by the algorithm as well. This helps the modeling closer to what the feeder is in real life. Additionally, from the result we can get which house should locate at which load node, which helps doing the demand response or distributed renewable energy integration study. This algorithm enables the study of quasi-static time-series analysis and other load related distribution feeder analysis becomes more realistic. Simulations are conducted to discuss the parameter selection for the algorithm and compared with the results generated by using other methods. The simulation results also proved that comparing with the ongoing approach, this method produces more realistic voltage and power flow results for the distribution feeder. The results have demonstrated the effectiveness and capability of this feeder load disaggregation algorithm.

CHAPTER 3 CONTROL OF COMMERCIAL BUILDINGS FOR GRID SERVICES

This chapter introduces the study on utilizing the HVAC system in commercial building to provide grid services. First, the model of commercial HVAC systems is described. Then the detailed centralized control strategy is presented. Finally, the performance of the proposed control method is evaluated through simulation.

Nomenclature

C_i	Thermal capacitance of the i^{th} HVAC zone (J/°C).
COP	Coefficient of performance.
c_p	Specific heat of air (J/kg/°C).
δ	Air recirculation ratio.
δm_i	Step size used to adjust airflow rate in zone i in the asymptotic allocation method (kg/s).
Δm	Mismatch between the total airflow rate and the desired value (kg/s).
η	Sensible heat ratio.
i	Index of an HVAC zone.
J_i	A set that contains all adjacent zones of zone i .
\dot{m}_i	Airflow rate of zone i .
\dot{m}_{tot}	Total airflow rate of an HVAC system (kg/s).
\hat{m}_{tot}	Desired total airflow rate of an HVAC system (kg/s).
$\overline{m}_i, \underline{m}_i$	Maximum and minimum airflow rate of zone i , respectively (kg/s).

$\overline{m}_i^S, \underline{m}_i^S$	Static maximum and minimum airflow rates of zone i constrained by damper operating ranges and ventilation requirements, respectively (kg/s).
$\overline{m}_i^t, \underline{m}_i^t$	Maximum and minimum airflow rates of zone i constrained by desired temperature ranges, respectively (kg/s).
N	Number of HVAC zones in a commercial building.
n_i	Number of steps of the static airflow operating range of zone i in the asymptotic allocation method.
P_{base}	Baseline power consumption of an HVAC system (W).
P_{dev}	Power deviation signals for an HVAC system (W).
$P_{chiller}$	Chiller power consumption (W).
P_{fan}	Fan power consumption (W).
P_{tot}	Actual power consumption of an HVAC system (W).
\hat{P}_{tot}	Desired power consumption of an HVAC system (W).
q_{ij}	Heat exchange between HVAC zones i and j (W).
R_i	Thermal resistance of the i^{th} HVAC zone ($^{\circ}\text{C}/\text{W}$).
σ	A reserve margin in percentage applied to limits of allowable airflow rate.
t	Index of a time step.
θ_c	Cooling coil discharge air temperature ($^{\circ}\text{C}$).
θ_i^+, θ_i^-	Temperature upper and lower limits of zone i , respectively ($^{\circ}\text{C}$).
θ_{out}	Outdoor air temperature ($^{\circ}\text{C}$).
θ_i	Temperature of zone i ($^{\circ}\text{C}$).

θ_{ret}	Air temperature in the return air duct (°C).
s_i	A flag indicating a control status of the airflow rate in zone i (1: adjustable; 0: not adjustable).
w_i	External disturbances from solar and occupancy in the i^{th} HVAC zone (W).

3.1 Commercial HVAC System Modeling

Commercial buildings can be categorized based on their principal building activities, include office, retail, warehouse, education, hotel, healthcare, grocery, restaurant, bank, and others. In this work, we study a typical HVAC system that serves office buildings which represent the most important building type, accounting for about one fifth of total floor space and building in the U.S. [75]. The configuration of the studied system is shown in Figure. 3.1, which consists of following components:

- 1) Variable air volume (VAV) terminals. VAV terminals adjust amount of the cooling/heating energy supplied to each thermal zone, based on the control signal from thermal zone controllers. Dampers and valves in the reheating coil are used to adjust cooling/heating energy.
- 2) Zone controllers. Zone controllers monitor zone temperature and generate the command for the opening of damper and valves based on the deviation of zone temperature from set points. The detailed control sequence is elaborated in the following subsection.
- 3) One air handling unit (AHU). The AHU generates and conveys the conditioned air. It consists of one cooling coil, one supply fan and one mixing box. The cooling coil is controlled to maintain the temperature of the air leaving the coil at a set point. The supply fan is used to circulate the air between the AHU and individual thermal zone. The speed of the supply fan

is modulated to maintain the static pressure in the duct at a set point. The mixing box is used to intake fresh air from ambient environment via outdoor air damper. In this study, we assume that the mixing box is controlled to maintain a constant outdoor air flow rate.

- 4) One chiller & one boiler. The chiller provides chilled water to cooling coils, and the boiler provides hot water to reheating coils. The chilled and hot water is circulated by dedicated pumps. In this work, we assume all the pumps are at constant-speed and thus their operation is not sensitive to the control action in the thermal zone.

As a part of a BMS, an HVAC zone controller is used to monitor and control the zonal temperature. Commands for adjusting dampers are issued to maintain zonal temperatures around setpoints. Specifically, a zonal temperature is fed back to a proportional-integral (PI) controller to calculate the desired zonal airflow rate. Another PI controller is used to adjust the opening of the damper and thereby control the airflow rate at a VAV terminal. It should be noted that airflow rates affect not only thermal comfort but also indoor air quality. Typically, a minimum zonal airflow rate is set at each VAV terminal to meet the ventilation requirement.

Please note that only the cooling mode is considered in this work. Nevertheless, the developed model and proposed control strategy can also be applied to HVAC systems in heating mode. Since the boiler, reheating coil, and hot water pumps are usually not involved in the cooling mode, equations associated with these components are omitted in this work. The following subsections elaborate how major components of the studied system are modeled.

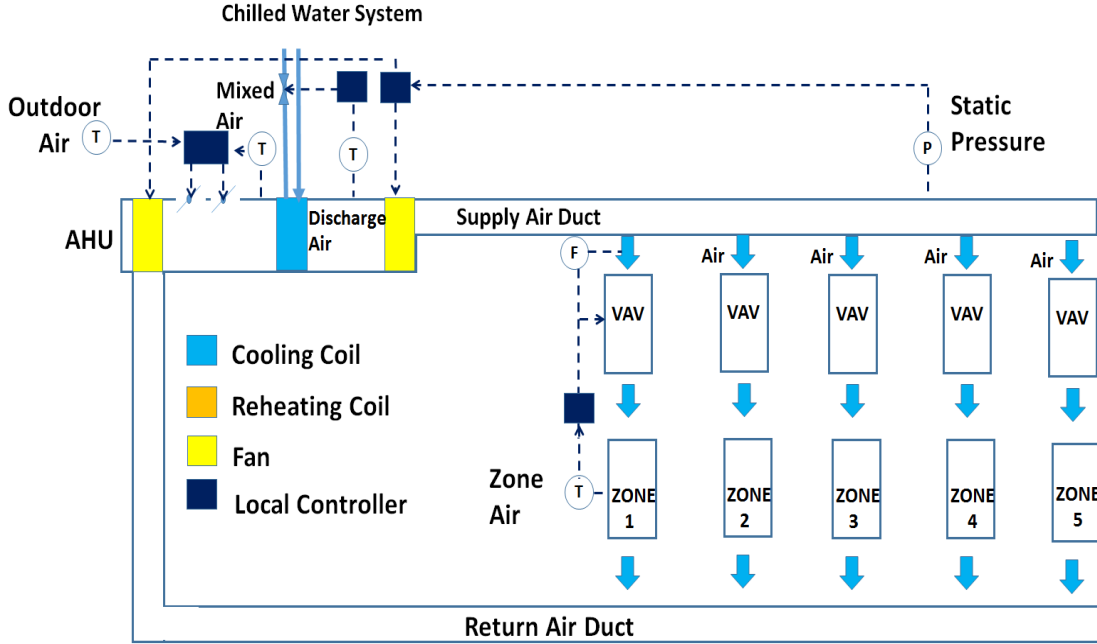


Figure. 3.1 The configuration of a typical HVAC system that serves office buildings

3.1.1 Multi-Zone Thermal Model

A first-order model [76] is used to describe zonal thermal dynamics:

$$C_i \frac{d\theta_i(t)}{dt} = \frac{\theta_{out}(t) - \theta_i(t)}{R_i} + c_p \dot{m}_i(t) (\theta_c - \theta_i(t)) + w_i(t) + \sum_{j \in J} q_{ij}(t), \quad (3.1)$$

where R_i and C_i are the thermal resistance and thermal capacitance of this zone, respectively; θ_i is the zone indoor temperature; θ_{out} is the outdoor temperature; θ_c is the temperature of cooling coil discharge air; $\dot{m}_i(t)$ is the support airflow mass flow rate of this zone; c_p is the specific heat of air; $w_i(t)$ is the external disturbances from solar and occupancy. J_i is the set of thermal zones directly exchanging heat with thermal zone i , and q_{ij} is the heat exchange between thermal zone i and j . However, it is hard to measure the value of C_i and R_i in practice, so a discrete, linear, data-driven model is used to calculate the temperature at next time step as,

$$\theta_i(t+1) = a_1^i \theta_i(t) + a_2^i \theta_{out} + a_3^i \dot{m}_i(t) (\theta_c - \theta_i(t)) + a_4^i + \sum_{j \in J} a_{ad,j}^i \theta_j(t), \quad (3.2)$$

where t is the current time step, and coefficients a_1^i , a_2^i , a_3^i and a_4^i can be obtained through linear regression. In particular, a_1^i captures impacts of the impact of its own temperature. a_2^i captures impacts of outdoor temperature on temperature of zone i , a_3^i captures thermal influence of cooling coil, a_4^i is used to represent external disturbances, $a_{ad,j}^i$ captures thermal influence of thermal zone j on zone i .

Such a bilinear physics-based multi-zone model is more accurate than a single-zone model, but the impacts of those input variables on zonal thermal dynamics still cannot be fully represented. Therefore, in this paper, we developed a machine learning based (ML-based) approach to capture the interactions among the input variables through extensive offline training instead of using a simplified thermal model such as (3.3).

$$\dot{m}_i(t) = f_i \left(\theta_i(t+1), \theta_i(t), \theta_{out}(t), \theta_c, \theta_j(t) \right), \forall j \in J_i \quad (3.3)$$

This function is convenient for estimating zonal airflow rate limits that maintain zonal air temperature within the desired ranges. These airflow rate limits are then used in the proposed priority-based algorithms to determine zonal airflow rates to track the desired charging and discharging power.

Among various ML methods, the ensemble method has been widely used for classification and regression. The main idea of this method is to aggregate multiple weighted models to obtain a combined one with improved performance in prediction [77],[78]. Four ML techniques with the ensemble method were selected and evaluated for training the function in (3.3) in this work. Monthly HVAC simulation data from July was used to test the performance of each ML technique with both 15-minute and 5-minute time intervals to meet the need in different use cases presented in Section IV. The k-fold cross-validation is used to assess the results generated by different ML

models. In each test, 80% of the data are randomly drawn from the pool to train the model and the remaining 20% are used for testing. Twenty tests are performed to calculate the mean absolute percentage errors (MAPEs) in predicting zonal airflow rates for each ML model. It has been found that the random forest model consistently outperforms the other ML models, and therefore it is selected in the proposed control. As an example, the results with a 15-minute time interval are provided in Table 3.1. To determine the number of decision trees and the maximum depth of the random forest model, extensive tests were performed. It was found that the best results were achieved with a maximum depth equal to 10 and a number of decision trees equal to 100 for both time intervals. As an example, the MAPE using different numbers of trees and maximum depth for the 15-minute time interval dataset is provided in Table 3.2. Therefore, the random forest method and these parameter settings are used in the case studies in this paper. Note that noise and missing data can be dealt with using methods developed in [79] and [80].

Table 3.1 MAPE of different machine learning techniques

	AdaBoost	Random Forest	Gradient Boost	Extra Trees
MAPE	6.67	4.36	4.45	5.69

Table 3.2 MAPE with different parameters in random forest

		Number of trees					
		2	20	50	100	500	1000
Max Depth	2	11.43	10.48	9.57	8.97	8.97	8.97
	5	7.93	7.56	6.21	5.20	5.20	5.20
	10	7.26	6.54	5.40	4.37	4.36	4.36
	15	7.25	6.54	5.39	4.37	4.36	4.36
	20	7.25	6.53	5.39	4.37	4.36	4.36

3.1.2 Supply Fan Model

In a commercial HVAC system, fan load is one part of the commercial HVAC system that can be controlled. Although a pump will consume some power, it usually has constant speed that leads to constant power. The power consumption of fan is related with the total airflow rate of the whole HVAC system, $\dot{m}_{tot}(t)$. We can use another data-driven model to express its power consumption as [81],[82]

$$P_{fan}(t) = c_3 * (\dot{m}_{tot}(t))^3 + c_2 * (\dot{m}_{tot}(t))^2 + c_1 * (\dot{m}_{tot}(t))^1 + c_0, \quad (3.4)$$

where c_0 , c_1 , c_2 , and c_3 can be derived from realistic measurement data of power and airflow rate and $\dot{m}_{tot}(t)$ is the summation of the airflow rate in each thermal zone, which can be represented as,

$$\dot{m}_{tot}(t) = \sum_{i=1}^N \dot{m}_i(t), \quad (3.5)$$

where $\dot{m}_i(t)$ is the airflow rate of each thermal zone.

3.1.3 Chiller Model

Besides fan, chiller load is another part of the commercial HVAC system that can be

controlled. The power consumption of the chiller can be described as [83]

$$P_{chiller} = \frac{c_p * \dot{m}_{tot}(t) * (\theta_{ret}(t) - \theta_c)}{\eta * COP}, \quad (3.6)$$

where COP is the coefficient performance of chiller and η is the sensible heat ratio of cooling coil. θ_{ret} is the mixed air temperature, which is the temperature after return air mixing with outdoor air. θ_{ret} can be calculated as

$$\theta_{ret}(t) = \delta * \frac{\sum_{i=1}^N (\dot{m}_i(t) * \theta_i(t))}{\sum_{i=1}^N (\dot{m}_i(t))} + (1 - \delta) * \theta_{out}, \quad (3.7)$$

where δ is the indoor air fraction. In practice, the air recirculation ratio may vary with time of a day and season of a year, depending on the setting of the air-side economizer [84] and ventilation control [85]. Nevertheless, it can be assumed to be constant in real-time control applications. Note that δ is less than 1 to make sure there is enough oxygen in building.

The total power consumption of the studied system is the summation of fan power and chiller power,

$$P_{tot}(t) = P_{fan}(t) + P_{chiller}(t). \quad (3.8)$$

Using the data-driven model allows the BMS controller to use historical data to update the model parameters in (3.2)-(3.8) without deriving the physical parameters of the building. Because the model parameters can be tuned by actual building energy consumption, the accuracy of the model for calculating the airflow rates with respect to power changes can be significantly improved compared with the model-based approach.

3.2 Commercial HVAC System Control Strategy

Existing BMS and zonal controllers are designed to meet occupants' comfort requirements without considering the needs from the grid. As described in the previous section, the amount of cooling energy supplied to each thermal zone is adjusted by zone controllers to maintain the zone

temperature around the set point. To do so, within each zone controller, the zone temperature is used as the input to calculate the volumetric flow rate of the supply air entering each zone with a proportional-integral (PI) controller. The desired volumetric flow rate can be used as a set point for another PI controller to determine the opening of the damper in corresponding VAV terminal. In addition, for each VAV terminal, there is a lower bound for the damper opening to meet the ventilation requirement. Therefore, they cannot directly take the desired power consumption as an input to provide grid services in real-time. This section proposes a centralized zonal airflow rate control method to follow grid signals while maintaining zonal air temperature within desired ranges.

Note that although the HVAC power consumption can be adjusted through changing zonal temperature setpoints, it is well-known that the change in temperature setpoints cannot be directly mapped to the change in the total HVAC power consumption because of uncertainties in temperature sensor accuracy and placement, random thermal events, current in-door and outdoor temperatures, and heat exchange rates. In addition, there can be significant time delays in thermostat-based HVAC power regulation and the payback phenomena can also significantly influence subsequent control accuracy.

The proposed method consists of two parts: a system-level control and a zone-level control, as illustrated in Figure. 3.2.

- At the system level, a mixed feedforward and feedback method is used to generate the desired power consumption from fans and chillers in a commercial HVAC system (\hat{P}_{tot}). This desired power consumption, outdoor air temperature, and the returned air temperature at the previous time step are used to estimate the desired total airflow rate based on fan and chiller models.

- At the zone level, an ML-based method is used to more accurately estimate zonal airflow rate limits considering zonal temperature constraints. Two priority-based control algorithms are then proposed to distribute the total airflow rate to individual zones. These obtained zonal airflow rates are sent to existing controllers at VAV terminals for adjusting damper opening.

The proposed control method can be an add-on to an existing BMS, in which security issues have been reasonably considered in system design, especially for the ones with demand response capability. The proposed method is used for determining zonal airflow rate setpoints, leveraging existing sensors and communication buses in the BMS. No upgrade to the security system is required.

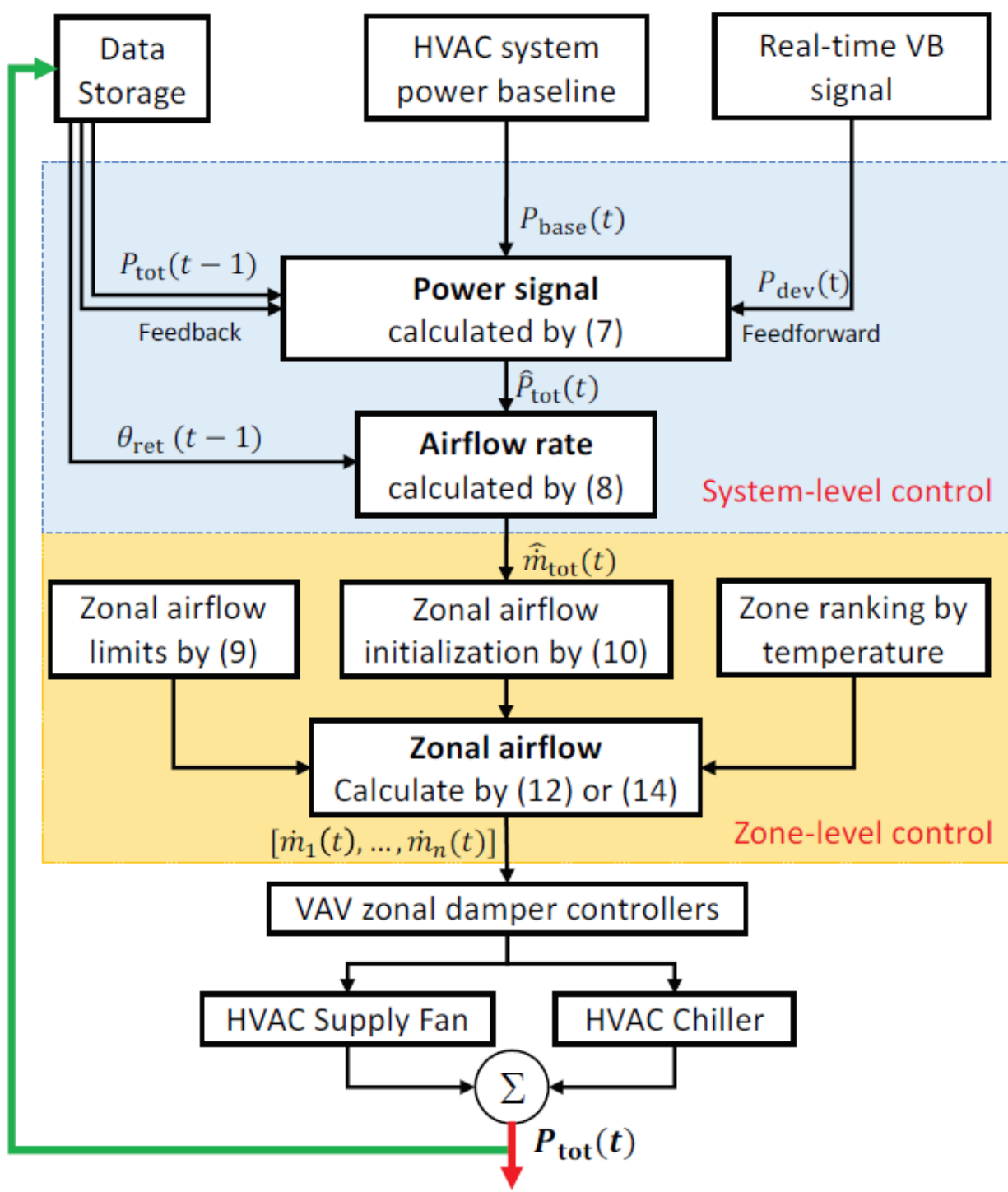


Figure. 3.2 Illustration of the proposed control

3.2.1 System-level Control

The system-level control receives real-time charging and discharging signals, which is the desired power deviation from a predetermined baseline—the power that would be consumed by fans and chillers without responding to grid signals. To improve the power tracking performance, a mixed feedforward and feedback control is used to estimate the desired total power consumption, as shown in (3.9):

$$\hat{P}_{tot}(t) = P_{base}(t) + P_{dev}(t) + [\hat{P}_{tot}(t-1) - P_{tot}(t-1)], \quad (3.9)$$

where $P_{base}(t)$ is the baseline power, $P_{dev}(t)$ is the feedforward signal that is added to the baseline power, and $\hat{P}_{tot}(t-1) - P_{tot}(t-1)$ calculates the power tracking error at the previous time step and is used as a feedback signal to calibrate the desired total power consumption from fans and chillers.

Based on the fan and chiller models described in (3.4)–(3.8), the desired total airflow rate cannot be calculated according to the desired total power consumption without knowing zonal airflow rates. In practice, the returned mixed air temperature can be approximated well by its value at the previous time step for real-time control, because zonal air temperatures change slowly within a small range during that time. Therefore, the desired total power consumption is reduced to a cubic function of the desired total airflow rate as shown in (3.10), which can be readily solved.

$$\begin{aligned} \hat{P}_{tot}(t) = c_3 * (\hat{m}_{tot}(t))^3 + c_2 * (\hat{m}_{tot}(t))^2 + c_1 * (\hat{m}_{tot}(t))^1 + c_0 \\ + \frac{c_p * \hat{m}_{tot}(t)}{\eta * COP} [\theta_{ret}(t) - \theta_c]. \end{aligned} \quad (3.10)$$

3.2.2 Zone-level Control

The zone-level control is used to distribute the desired total airflow rate produced at the system level to individual zones, considering damper operating limits, ventilation requirements, and desired zonal air temperature ranges. The main idea of the proposed zone-level control is to

initialize the zonal airflow rates to values at the previous time step, and then iteratively select a zone, adjust its airflow rate, and compare the total airflow rate with the desired value until the desired value is met or all zones are at their airflow limits. The detailed calculation is presented as follows.

1) *Zonal airflow limits*: When initializing and adjusting zonal airflow rates, the operating limits need to be respected. The zonal airflow rate limits depend on damper operating limits, ventilation requirements, and desired zonal air temperature ranges.

- Damper operating limits and ventilation requirements lead to a static airflow operating range for each zone, which can be expressed as $[\underline{m}_i^S, \overline{m}_i^S]$.
- The zonal airflow rates are also constrained by desired zonal temperature ranges, given the measured air temperatures in this zone and adjacent zones and outdoor temperature at the current time step. The resulting operating range is denoted as $[\underline{m}_i^t, \overline{m}_i^t]$, which generally varies from one time step to another. The lower and upper bounds can be estimated using the ML model described in Section 3.1 by setting $\theta_i(t+1)$ to the upper (θ_i^+) and lower (θ_i^-) bounds of the desired zonal temperature, respectively, assuming the HVAC system is operated in cooling mode.

Once these two ranges are obtained, one can readily generate their intersection with boundaries expressed as

$$\overline{m}_i(t) = \max\left(\min\left(\overline{m}_i^S(t), (1 - \sigma)\overline{m}_i^t(t)\right), \underline{m}_i^S(t)\right), \quad (3.11(a))$$

$$\underline{m}_i(t) = \min\left(\max\left(\underline{m}_i^S(t), (1 + \sigma)\underline{m}_i^t(t)\right), \overline{m}_i^S(t)\right), \quad (3.11(b))$$

where a reserve margin σ between 0 and 1 is introduced to narrow the airflow operating range and thereby compensate forecasting errors. These zonal airflow rate limits are updated at each time step.

2) *Initialization*: At each time step, zonal airflow rates are initialized to values at the previous time step. In cases when these airflow rates exceed the calculated operating limits at the current time step, initial values are set to their limits, as expressed in (3.12):

$$\dot{m}_i(t) = \begin{cases} \bar{m}_i(t), & \text{if } \dot{m}_i(t-1) > \bar{m}_i(t) \\ \underline{m}_i(t), & \text{if } \dot{m}_i(t-1) < \underline{m}_i(t) \\ \dot{m}_i(t-1), & \text{otherwise} \end{cases} \quad (3.12)$$

3) *Zone ranking*: When selecting zones for increasing (or decreasing) airflow rates, a zone with higher temperature has a higher priority for increasing airflow rate, assuming the HVAC system is operated in cooling mode. Therefore, a priority list is constructed by ordering all zones according to the measured air temperatures from high to low. Each zone is selected according to its order on the priority list.

4) *Iterative adjustment of zonal airflow rates*: At each iteration, the mismatch between the total airflow rate and the desired value is first updated:

$$\Delta m(t) = \hat{m}_{tot}(t) - \sum_i \dot{m}_i(t). \quad (3.13)$$

The airflow rate needs to be increased or decreased for a zone, depending on the sign of the mismatch. It should be noted that the airflow rate is updated only for one zone each time. Two allocation algorithms are proposed using different adjustment magnitudes, which are described as follows.

- *One-step allocation*: In this method, zones on the priority list are selected one by one to increase or decrease airflow rate up to the operating limits to offset the mismatch in (3.13).

In other words, we fully use the flexible operating range of a zone before moving to the

next zone on the priority list. The airflow rate of the selected zone at the current iteration is updated according to (3.14):

$$\dot{m}_i(t) = \begin{cases} \min(\overline{m}_i(t), \dot{m}_i(t) + \Delta m(t)), & \text{if } \Delta m(t) \geq 0, \\ \max(\underline{m}_i(t), \dot{m}_i(t) + \Delta m(t)), & \text{if } \Delta m(t) < 0. \end{cases} \quad (3.14)$$

- Asymptotic allocation: In this method, zones on the priority list are selected one by one to gradually increase or decrease airflow rate to offset the mismatch in (3.13). This method avoids to use all flexibility of a zone at once before exploring other zones and aims to use flexibility from all zones equally. To do so, the static operating range of zone i is divided into n_i steps, and the adjustment step size for each zone is calculated as

$$\delta m_i = \frac{\overline{m}_i^S - \underline{m}_i^S}{n_i}. \quad (3.15)$$

The airflow rate of the selected zone at the current iteration is updated according to (3.16):

$$\dot{m}_i(t) = \begin{cases} \min(\dot{m}_i(t) + \delta m_i, \dot{m}_i(t) + \Delta m(t), \overline{m}_i(t)), & \text{if } \Delta m(t) \geq 0, \\ \max(\dot{m}_i(t) - \delta m_i, \dot{m}_i(t) + \Delta m(t), \underline{m}_i(t)), & \text{if } \Delta m(t) < 0. \end{cases} \quad (3.16)$$

To facilitate the zonal airflow update and determine the termination of iterations, a flag is introduced for each zone, which indicates the control status, with 1 for adjustable and 0 for not adjustable:

$$s_i = \begin{cases} 1, & \text{if } \underline{m}_i(t) < \dot{m}_i(t) < \overline{m}_i(t), \\ 0, & \text{otherwise.} \end{cases} \quad (3.17)$$

The number of steps can be selected based on desired resolution level in balancing the contribution of different zones to a change in total airflow rate. Increasing n_i improves the resolution but requires more iterations to converge. When n_i is set to 1, the asymptotic allocation degenerates to the one-step allocation.

The zone-level control algorithms with the one-step and asymptotic allocation methods are provided in Algorithm 5 and Algorithm 6, respectively.

Algorithm 5 One-step Zonal Airflow Allocation

- 1: Estimate $\overline{m}_i(t)$ and $\underline{m}_i(t)$ using (3.11).
 - 2: **for** $i = 1$ to N **do**
 - 3: Initialize $\dot{m}_i(t)$ using (3.12).
 - 4: **end for**
 - 5: Sort zones by measured temperature from high to low, with an updated index denoted by i .
 - 6: **for** $i = 1$ to N **do**
 - 7: Update the total airflow mismatch using (3.13).
 - 8: Update the airflow rate of zone i using (3.14).
 - 9: **end for**
-

Algorithm 6 Asymptotic Zonal Airflow Allocation

- 1: Estimate $\overline{m}_i(t)$ and $\underline{m}_i(t)$ using (3.11).
 - 2: **for** $i = 1$ to N **do**
 - 3: Initialize $\dot{m}_i(t)$ using (3.12).
 - 4: **end for**
 - 5: Sort zones by measured temperature from high to low, with an updated index denoted by i .
 - 6: Initialize $s_i = 1$ for $i = 1, 2, \dots, N$.
 - 7: **while** ($\Delta m(t) \neq 0$ & $\sum_i s_i > 0$) **do**
 - 8: **for** $i = 1$ to N **do**
 - 9: **if** $s_i = 1$ **then**
 - 10: Update the total airflow mismatch using (3.13).
 - 11: Update the airflow rate of zone i using (3.16).
 - 12: Update the flag of zone i using (3.17).
 - 13: **end if**
 - 14: **end for**
 - 15: **end while**
-

Remark 1: The one-step allocation method is simple and fast, but may lead to sudden zonal airflow changes and increased fluctuations of zonal temperature. This control is more appropriate for HVAC zones with no occupants, such as storage zones and equipment rooms. The asymptotic allocation method is more complicated but can more evenly distribute airflow changes to

individual zones, leading to smoother zonal airflow rates and temperature profiles. It also helps maintain all zones active, leading to more flexibility for future use and thereby improve temperature control.

Remark 2: Different actions can be taken when a component failure is detected.

- If there is a failure on a fan or chiller, the HVAC system stops working whether or not grid services are considered. Grid signals are completely ignored in this case.
- If there is a failure on a zone controller, the zone is excluded from the control for grid services. The flexibility from other HVAC zones is used to follow the desired power consumption as closely as possible.

3.3 Case Study

In this work, a medium-size office building with 17 zones at the Pacific Northwest National Laboratory (PNNL) campus was used to illustrate and validate the proposed real-time control method. The EnergyPlus model was developed using the building design document. The proposed real-time control method was implemented in Python. We set $n_i = 10$ in the asymptotic allocation algorithm in this study. A co-simulation engine called Building Controls Virtual Test Bed [86] was used to link the Python-based controller and the building model in EnergyPlus for information exchange at each time step. Table 3.3 lists the HVAC system parameters, including desired zonal temperature ranges, cooling coil discharge air temperature, air recirculation ratio, etc.

Table 3.3 HVAC system parameters

Working period	θ_i^+	θ_i^-	θ_c	σ	η	COP
6 a.m.-5 p.m.	21.9	20.3	13	0.7	0.9	6.16

In order to test the performance of the ML model, we compared the performance result in case study with the performance by using zone thermal dynamics in (3.2). One set of example model parameters from linear regression result for one zone are $a_1^1 = 0.832$, $a_2^1 = 0.0195$, $a_3^1 = 0.1907$, $a_4^1 = 0.7758$, $a_5^1 = 0.019$ and $a_6^1 = 0.13$ [87]. It can be observed that the summation of a_1^1 , a_5^1 and a_6^1 is around 1, which matches the common expectation. The detailed parameters of all these thermal zones are shown in Table 3.4. Figure. 3.3 and Figure. 3.4 shows the comparison between the actual measured temperature in one zone and the predicted temperature by using this model with these parameters.

Table 3.4 Parameter of each thermal zone for the building model

Zone	a_1	a_2	a_3	a_4	a_5	a_6
1	0.9633	0.08645	0.154402	0.80693	0.0067	0
2	0.920572	0.029061	0.135918	0.285843	0.049428	0
3	0.969451	0.014212	0.388857	0.676835	0.000549	0
4	0.966500	0.09065	0.98632	0.590177	2.02E-13	0
5	0.513100	0.08065	0.95363	0.623685	8.55E-15	0.47
6	0.916244	0.095465	0.85955	0.92126	0.05875	0
7	0.831911	0.010091	0.520014	0.98656	2.79E-15	0.138089
8	0.5122	0.011969	0.521557	0.959562	0.289287	0.180713
9	0.964696	0.019524	0.190711	0.775793	0.005304	0
10	0.871656	0.036579	0.091322	0.306946	0.098344	0
11	0.654003	0.010471	0.828254	0.951945	0.00532	0.315125
12	0.95321	0.01055	0.36595	0.653956	0.0153	6.63E-13
13	0.96232	0.017282	0.721214	0.692906	0.03202	1.23E-12
14	0.912037	0.045658	0.841216	0.023006	0.057963	0
15	0.691934	0.055362	0.203115	0.00568	0.03272	0.245345
16	0.895201	0.047183	0.736001	1.43E-09	2.67E-10	0.074799
17	0.96896	0.029051	0.611848	0.442113	4.17E-14	0

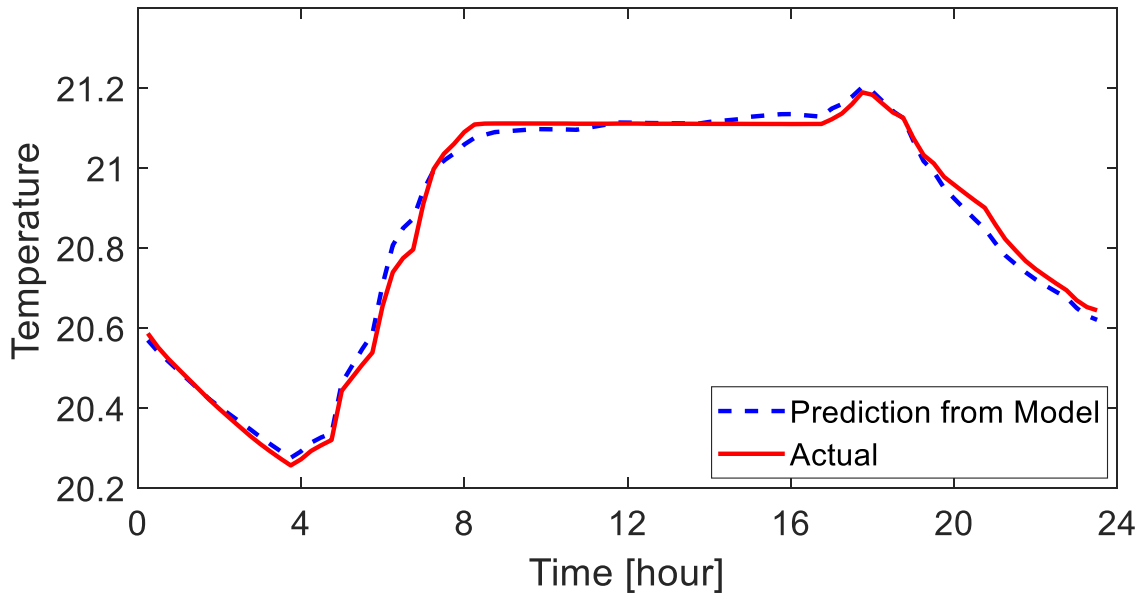


Figure. 3.3 Predict and actual temperature comparison for the first example thermal zone

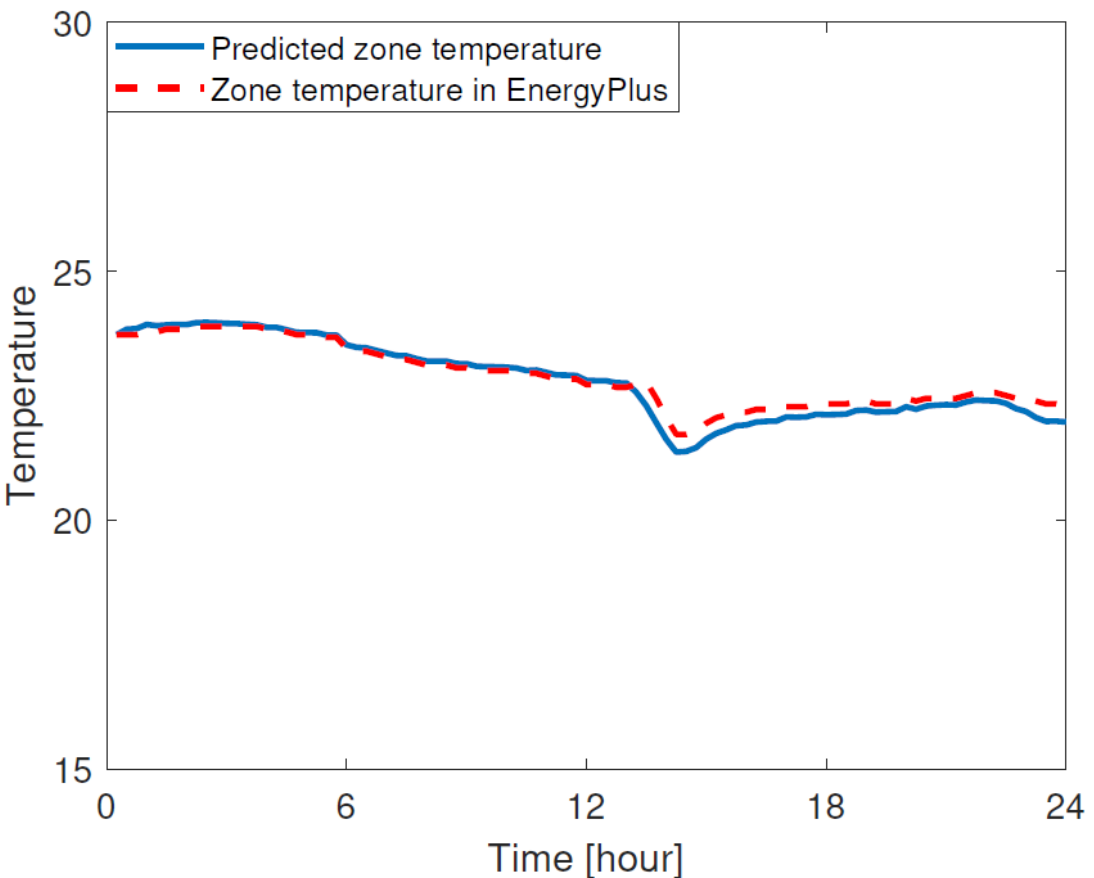


Figure. 3.4 Predict and actual temperature comparison for the second example thermal zone

According to the data we have, it shows that this model performs best when the time interval is 15 minutes. Therefore, the simulation time resolution in this work is chosen to be 15-minute. By using the airflow rate and the corresponding fan power, the regressed coefficient for (3.4) are $c_1 = 0.00747$, $c_2 = -0.00921$, $c_3 = 0.13056$ and $c_4 = 0.00158$. Figure. 3.5 shows the comparison between measured fan power and predicted fan power using (3.4) and identified fan model parameters. It can be shown that the predicted fan power is a good approximation of the measured fan power.

The VAV box in each zone can control its air volume rate, so the corresponding maximum and minimum \dot{m}^i are measured as well. Note that because of the fresh air requirement [88], \dot{m}_{min}^i cannot be zero. \dot{m}_{max}^i is designed based on thermal zone characteristics when constructing the building HVAC system. These two zone parameters are considered as constraints when VAV is been controlled.

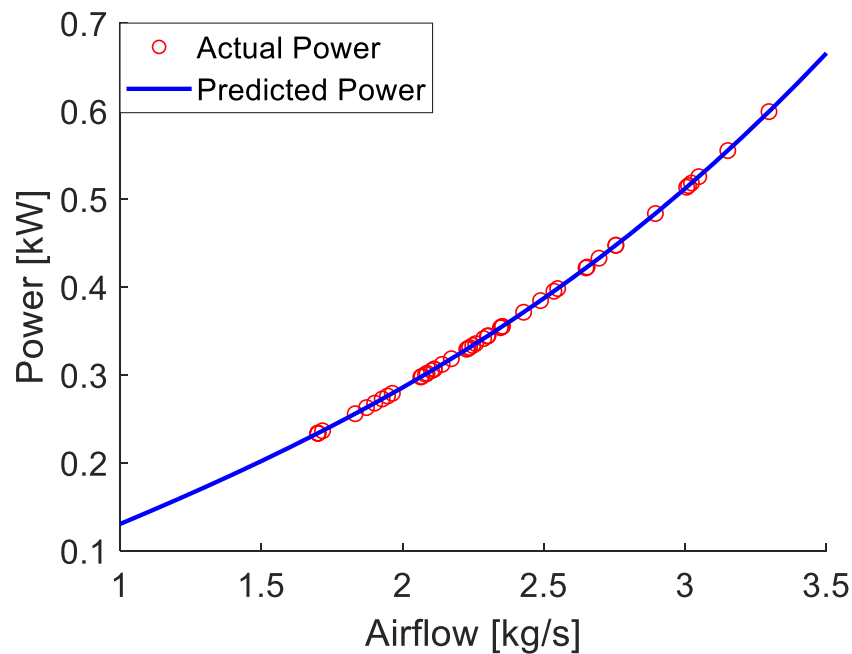


Figure. 3.5 Predict and actual fan power comparison

Three use cases are considered, including i) baseline following, ii) duck curve offsetting, and iii) PV output smoothing. The baseline is the power that would be consumed by fans and chillers without responding to grid signals. In the VB-based scheduling and control framework described in Section I, the baseline power together with the VB flexibility are submitted to system operators for resource coordination at the scheduling stage and generate and broadcast grid signals based on balancing and/or ramping needs in real time. Based on different VB resources [89], grid operator will assign each VB a signal to follow. The proposed real-time control is used for commercial HVAC systems to follow grid signals they receive. To illustrate and validate the proposed control, the two representative grid signals in the last two cases were generated as examples of how system operators could use flexible commercial HVAC load to serve the grid. Because the flexibility captured by VB models is used for system operators to coordinate different resources and determine demand response (DR) signals, with proper controls, the reference power can be followed within reasonable accuracy while meeting the temperature constraints.

The proposed control methods were tested for the use cases over 23 workdays in a typical August. The simulation time step is 15-minute for the first two and 5-minute for the last one. The results were evaluated and compared using four key statistic performance metrics:

- MAPE in tracking power signal,
- Time in percentage with power tracking error less than 5%,
- Time in percentage when zonal temperatures are out of desired ranges,
- Maximum temperature violation ($^{\circ}\text{C}$).

The first two measure the performance in tracking the desired power signal, and the last two measure the performance in zonal temperature control.

3.3.1 Baseline Following

In real-time, an HVAC system needs to follow the submitted baseline as closely as possible when there is no DR signal sent by the system operator. Once a DR signal is received, it will move up and down against the baseline to respond. Thus, following a baseline operation allows the DR response to be measurable. In this paper, the HVAC system power consumption profile for the next day is first generated by simulating the building operation in EnergyPlus with the default control setpoints using the next day temperature forecast as inputs. Then, the forecasting errors are modeled by a random forecast error that is 5% of the baseline (a uniform distribution is used). The baseline is obtained by adding the random forecasting error to the simulate HVAC power consumption profile. The outdoor temperature for an example day is shown in Figure. 3.6 The building operation was simulated again with the co-simulation engine using the baseline as the reference power of the proposed real-time control. Simulation results on baseline power tracking and zonal temperature control were collected and analyzed, which are presented as follows.

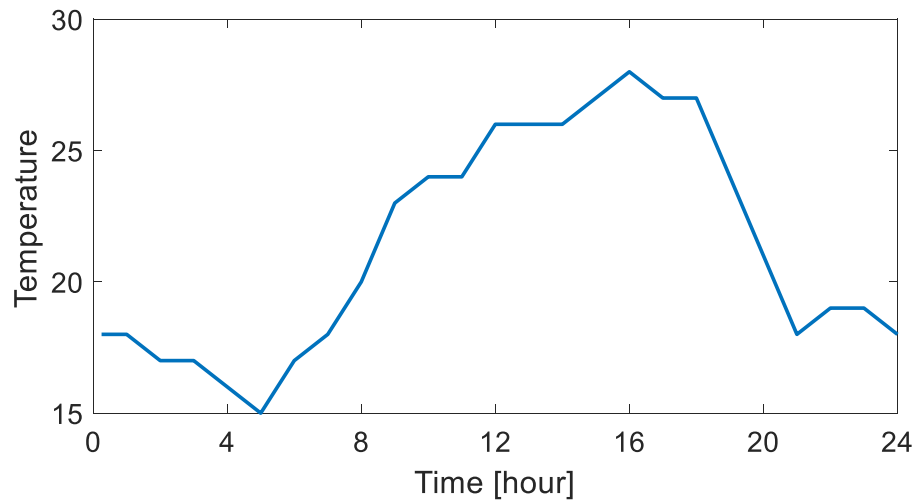
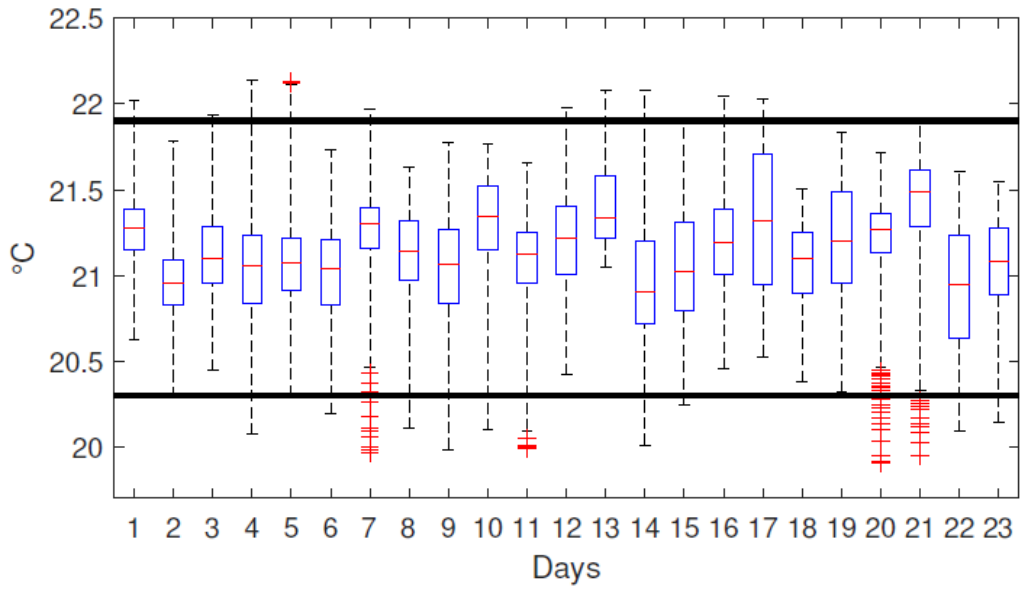


Figure. 3.6 Outdoor temperature in °C

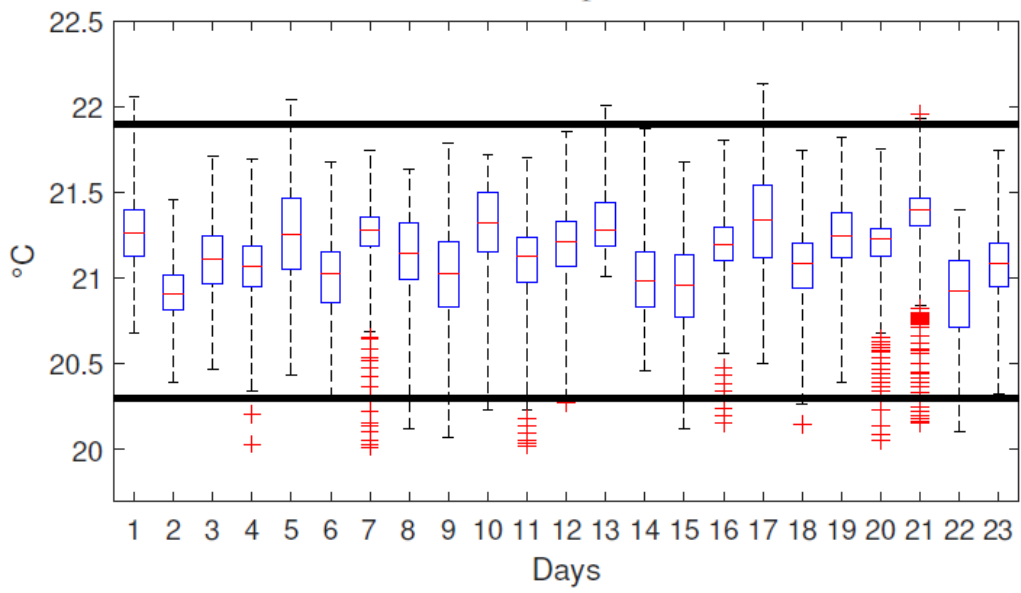
1) *Performance of the proposed control:* The zonal temperature distribution for both one-step and asymptotic allocation methods is shown in Figure. 3.7, where the desired temperature range is

indicated by the two black horizontal lines. As can be seen, the proposed control well maintains zonal temperature within the desired range most of the time. Some outliers exceeding the desired temperature deadband are mainly due to errors in estimating zonal airflow limits to meet the desired temperature range. Default HVAC controllers cannot always maintain all zonal temperatures within the desired deadband all the time either. Such small violations are acceptable in practical applications. The 17 zonal air temperature profiles on day 14 are plotted in Figure. 3.8, where the desired temperature range is indicated by the two black horizontal lines. More oscillations can be observed with the one-step allocation method, because the method may cause sudden changes in airflow rates. On the other hand, the asymptotic allocation method results in smoother temperature profiles and less violation of the desired temperature.

The key statistical performance metrics are provided in Table 3.5. The results show that the baseline power profile can be well tracked with both allocation methods, with an MAPE of less than 1.5% and for more than 98% of the time with a tracking error of less than 5%. The performance difference in power tracking between these two allocation methods is very small because they mainly affect zonal temperature control. As for zonal temperatures, the proposed control with both allocation methods well maintains the temperature within the desired ranges, with a small violation for less than 1% of the time. In particular, the asymptotic allocation helps to reduce the frequency and magnitude of violations.

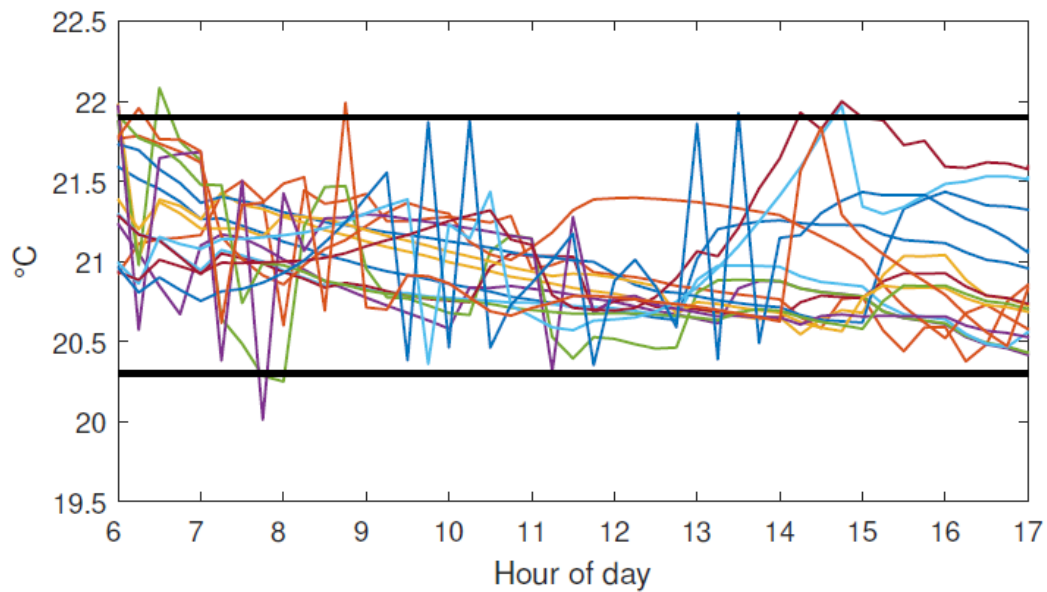


(a) One-step

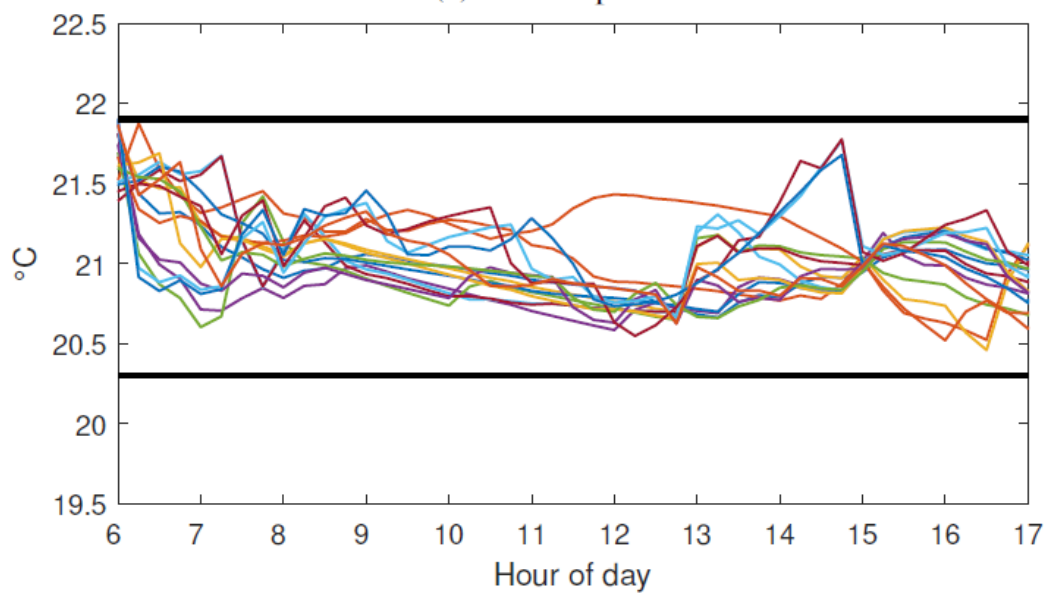


(b) Asymptotic

Figure. 3.7 Boxplot of zonal temperatures for each testing day in the baseline following case



(a) One-step



(b) Asymptotic

Figure. 3.8 Temperature profiles for 17 zones on day 14 in the baseline following case

Table 3.5 Baseline following performance

Performance Metric		One-step	Asymptotic
Power tracking	MAPE	1.25%	1.42%
	Time with <5% error (%)	98.39%	98.11%
Temp. control	Time with violation (%)	0.79%	0.51%
	Max violation (°C)	0.395	0.284

2) *Comparison of ML-based and physics-based thermal models:* This paper proposes to estimate zonal airflow rate limits in a multi-zone commercial building using ML techniques, instead of using popular physics-based thermal models in many existing studies. Baseline following results were also generated using two popular physics-based thermal models. ML-based and physics-based thermal models are used to estimate operating ranges of zonal airflow rates, which only affect zonal temperatures. Therefore, only performance in temperature control is compared for different airflow rate limit estimation methods, including

- the proposed ML-based estimation method,
- estimation method based on the thermal model with inter-zone coupling (as described by (3.2)),
- estimation method based on the thermal model without inter-zone coupling (similar to the model in (3.2) except the last term on the right-hand side is excluded).

Comparison results using the asymptotic allocation method are shown in Table 3.6. Compared to the two physics-based methods, the temperature control performance is much improved using the ML-based estimation method, with the temperature violation time reduced by more than 80% and the maximum violation reduced by 32-45%.

Table 3.6 Comparison of temperature control performance

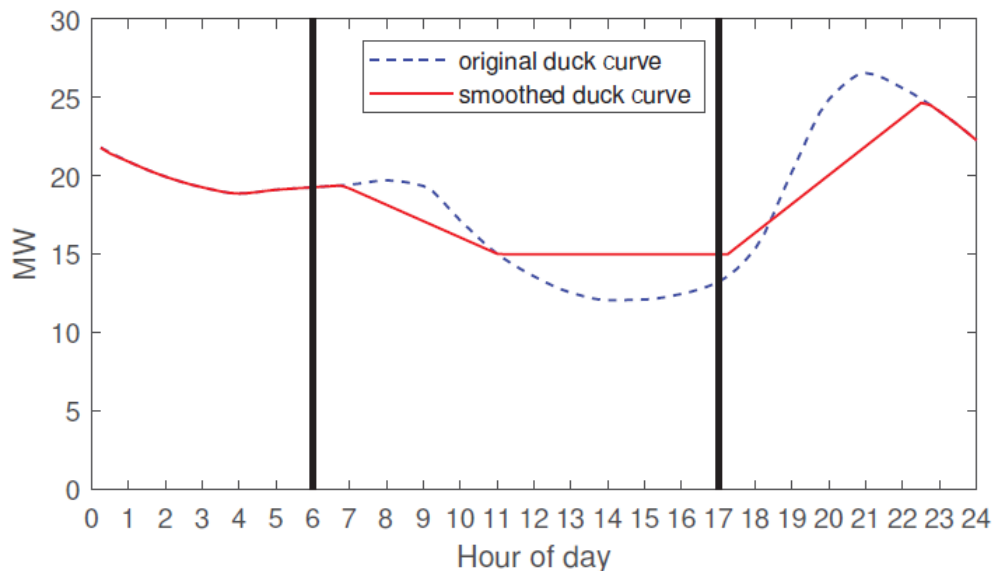
	ML-based	Physics-based	
		w/ coupling	w/o coupling
Time with violation (%)	0.51%	3.18%	4.46%
Max violation (°C)	0.284	0.420	0.521

3.3.2 Duck Curve Offsetting

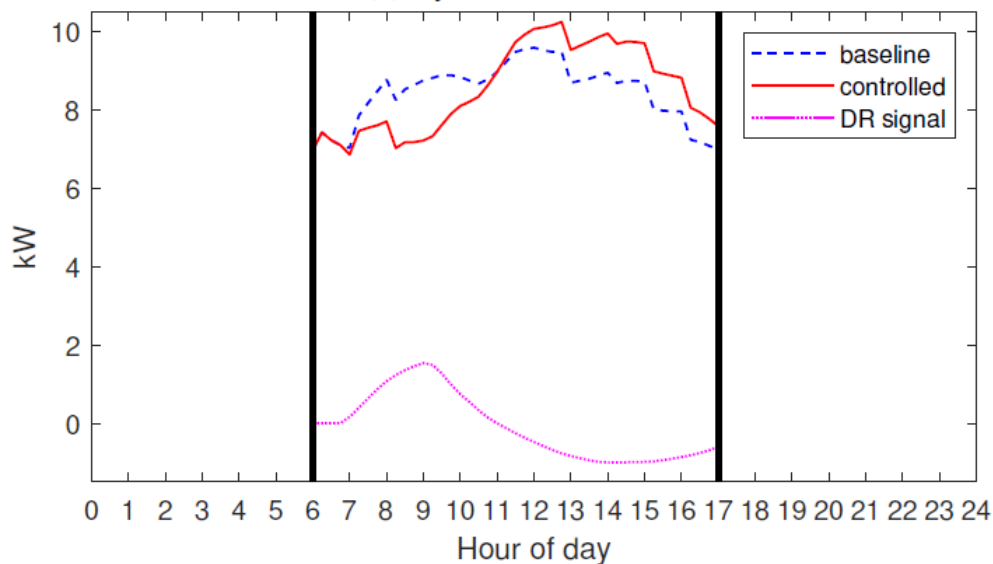
The output from solar power typically increases rapidly in the morning and decreases rapidly in the afternoon [90-94]. High penetration of solar generation results in a “duck curve”, presenting a significant challenge to grid operators for maintaining reliable operation [95], [96]. Commercial HVAC systems can help to offset the duck curve. In this case, a charging/discharging signal was generated to shift the energy consumption of the HVAC system and thereby help to smooth the duck curve in California [97]. A typical netload in California is plotted by the blue dashed line in Figure. 3.9 (a). Taking advantage of the energy storage capability in the thermal mass, the HVAC power consumption was controlled using the proposed method to follow this slow changing signal, and thereby help to fill the valley and decrease the ramping of the netload. The baseline power, controlled HVAC power, and charging/discharging signal are plotted in Figure. 3.9 (b). The energy shifting effect from this example building is scaled by 1.7 million (about a half of the number of commercial buildings in California) to demonstrate the flexibility potential from commercial HVAC systems. The obtained netload is compared with the original duck curve in Figure. 3.9 (a). Effectively offsetting the duck curve reduces the power system ramping requirement and operation cost as well as cycling of generators.

As an example, zonal temperature profiles on day 14 using the asymptotic allocation method are plotted in Figure. 3.10. Compared to the baseline following case in Figure. 3.8, zonal

temperatures are closer to the upper bound in the morning, because the building was “discharged” by reducing the cooling airflow, leading to increased temperatures. On the other hand, zonal temperatures are closer to the lower bound in the afternoon, because the building was “charged” by increasing the cooling airflow, leading to decreased temperatures. Similar results were obtained for the one-step allocation method, and the plot is omitted here to conserve space.



(a) System netload



(b) HVAC power and demand response signals

Figure. 3.9 Offsetting ‘duck curve’ in California

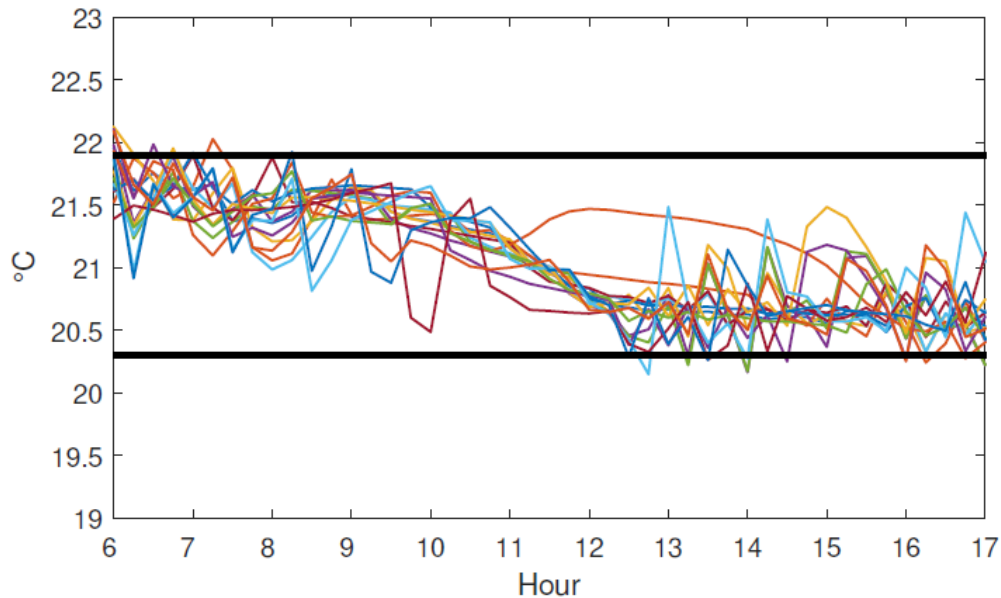


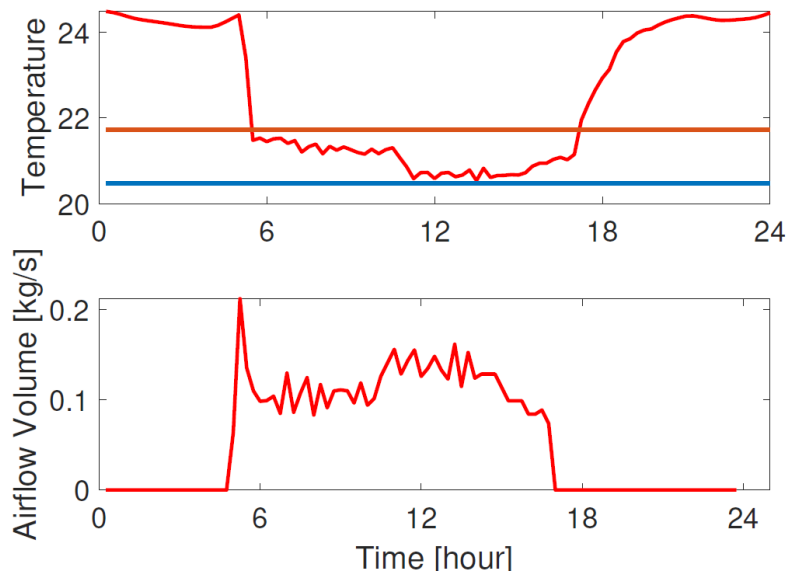
Figure. 3.10 Temperatures profiles for 17 zones using the asymptotic allocation on day 14 in the duck curve offsetting case

The control performance over the 23 testing days is summarized in Table 3.7. Similar to the baseline following results, the proposed method with both allocation algorithms is able to control the HVAC system to track the desired power consumption within reasonable accuracy: with an MAPE of less than 2% and for more than 93% of the time with a tracking error of less than 5%. While zonal temperatures are still maintained within the desired ranges most of the time, the frequency and magnitude of violations increase compared to the baseline following case. In this case, it is more obvious that the asymptotic allocation method provides better performance in zonal temperature control than the one-step allocation method.

Table 3.7 Duck curve offsetting performance

Performance Metric		One-step	Asymptotic
Power tracking	MAPE	1.93%	1.91%
	Time with <5% error (%)	93.82%	93.64%
Temp. control	Time with violation (%)	7.58%	3.88%
	Max violation (°C)	1.164	0.628

The daily temperature and airflow rate of one example thermal zone is shown in Figure. 3.11. It can be observed that during the day, the temperature change and airflow change is not very fast. This ensures that the operation of commercial HVAC system is like what it should be in the conventional control.

**Figure. 3.11** Daily temperature and airflow rate of one example thermal zone

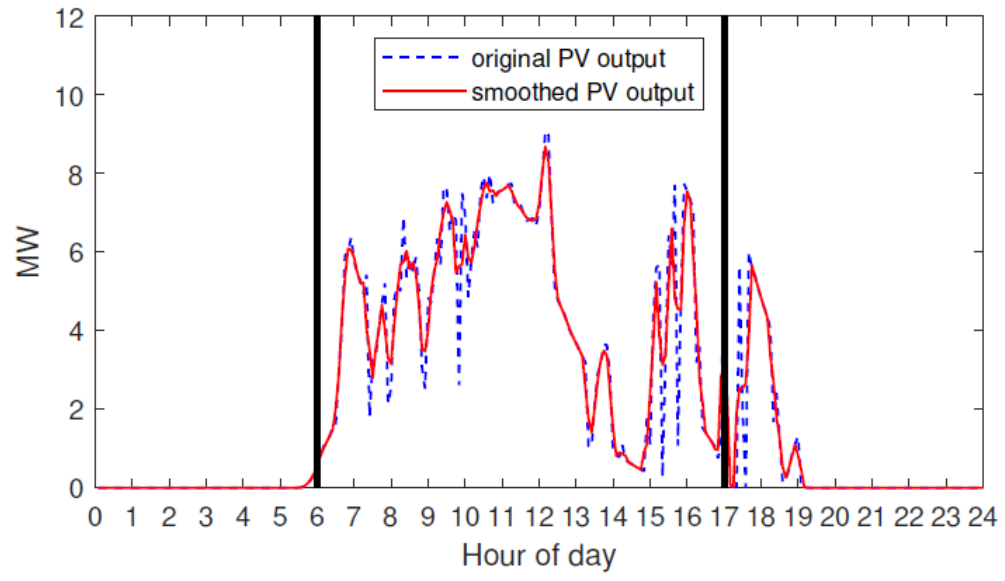
3.3.3 PV output smoothing

The proposed method can also be used to control the commercial HVAC system to smooth PV output [98-102]. Compared with the duck curve offsetting use case, PV smoothing represents

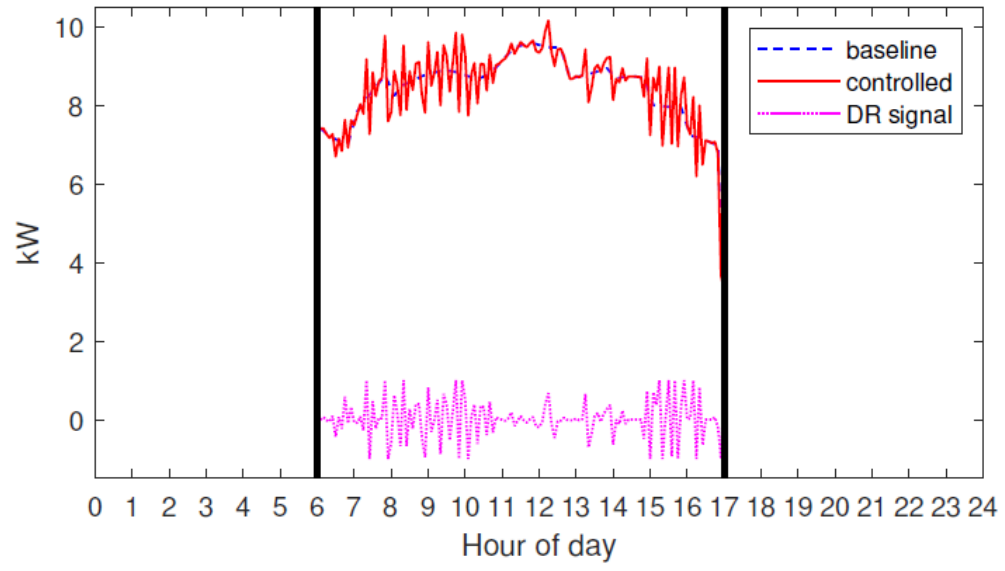
a service with faster changing signals [103-112]. To test the performance of the proposed control in tracking fast-change signals, the moving average over three-time steps was generated for a representative PV profile and compared with the original profile to determine the VB control signal [113-116]. The ML-based model for estimating zonal airflow rate limits was updated using 5-minute measurement data. The statistic performance of PV output smoothing case is shown in Table 3.8. The system netload and HVAC power results using the asymptotic allocation method are plotted in Figure. 3.12. On the other hand, as shown in Figure. 3.13, the duration of each violation in temperature is generally less compared to the energy shifting (duck curve offsetting) case. The mean duration is about 15 minutes, about half of the previous case. This is mainly because the signal for PV smoothing is more energy neutral and faster compared to duck curve offsetting case so that the building can be “charged” and “discharged” more frequently, which avoids consistently increasing or decreasing airflow rates over a long time period.

Table 3.8 PV smoothing performance

Performance Metric		One-step	Asymptotic
Power tracking	MAPE	2.01%	2.06%
	Time with <5% error (%)	92.95%	92.83%
Temp. control	Time with violation (%)	7.96%	4.02%
	Max violation (°C)	1.563	0.795



(a) System netload



(b) HVAC power and demand response signals

Figure. 3.12 Smoothing PV output

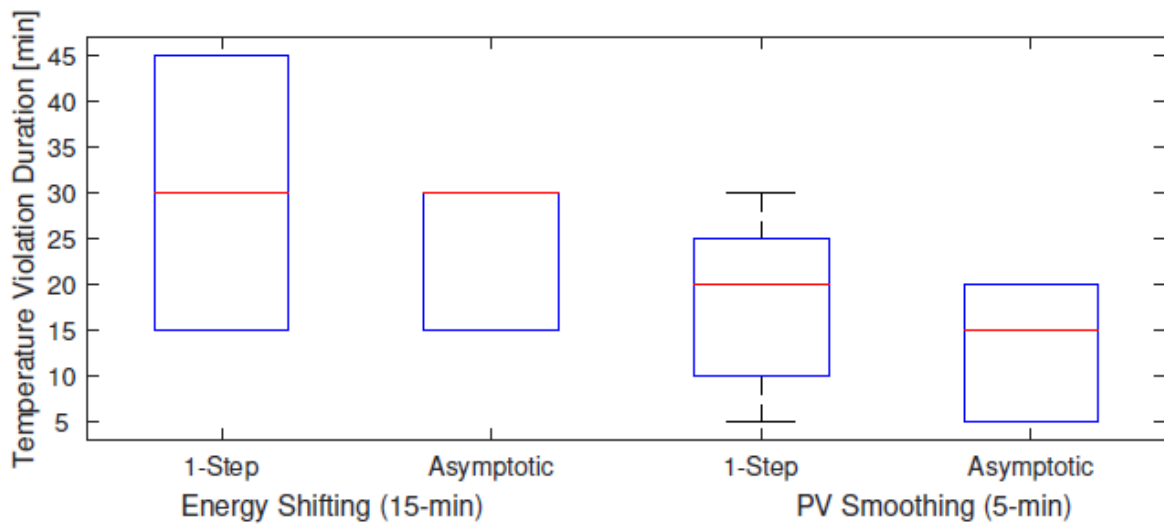


Figure. 3.13 Duration time distribution of each temperature violation for two methods

3.4 Conclusions

In this section, we use data-driven models to conduct the control algorithm of commercial virtual batteries. We use 15-minute interval data to regress these models and get the coefficients' value. A machine-learning based approach is also proposed as an alternative method to control the HVAC systems in commercial building. Random forest is selected as the machine-learning model and is trained by a monthly HVAC operation data that is simulated by using EnergyPlus. Based on the data-driven method and machine-learning method, we develop a centralized controller to control HVAC following the target power signal by adjusting the airflow rate in each thermal zone. Two different control strategies are proposed to achieve the different distribution requirement for the airflow rate in different HVAC zones. A platform built in EnergyPlus is used to test the performance of this algorithm. The simulation results show that the proposed control algorithm has effectively controlled the HVAC in commercial VB to follow the baseline power, the total power after the duck curve demand response signal is added and the total power after the PV smoothing signal is added. The two proposed control strategies are tested to prove their efficiency in controlling the HVAC

system in commercial buildings. The simulation results also show that it is necessary to consider the thermal interaction between thermal zones.

CHAPTER 4 SUMMARY AND FUTURE WORK

4.1 Summary of Previous and Current Research

Motivated by the large energy consumption and power flexibility in the thermal controlled loads in buildings, the research work on utilizing building loads to provide grid services has been developed in two sub-areas: modeling the load in distribution system that can be used for QSTS analysis, and the control of the HVAC system in commercial buildings. The work in each sub-area is abridged as follows:

4.1.1 Feeder Load Disaggregation Algorithm

This sub-area presents the feeder load disaggregation algorithm for conducting quasi-static time-series simulation on actual distribution feeder using realistic smart meter data and the substation feeder head load profiles or other available information. A feeder-head load profile is usually known to utility engineers but nodal load profiles on the feeder are not. Thus, in this dissertation, we present a pivot-point based, two-stage feeder load disaggregation algorithm using smart meter data. The two stages are load profile selection and load profile allocation.

In the LPS stage, a random load profile selection process is first executed to meet the load diversity requirement. Then, a few pairs of pivot points are selected as the matching targets. After that, a matching algorithm will run repetitively and select one load profile at a time to match the reference load profile at the pivot points while satisfying load composition requirements.

In the LPA stage, the LPS selected load profiles are allocated to each load node on the feeder considering distribution transformer loading limits, load composition, and square-footage. The proposed method is developed and validated using actual feeder and smart meter data from a North Carolina service area. Three performance criteria are used to measure the performance of the algorithm: accuracy of selecting the total number of load profiles, accuracy of matching load

shapes, and accuracy of meeting load composition and total nodal square footage requirements.

The simulation results demonstrated that the proposed pivot-point-based, two-stage FLDA not only ensures that the aggregated load profile of all generated nodal load profiles match the actual metered feeder-head load profile at the pivot points but also provides satisfactory matching results on the rest of the feeder-head load profile. In addition, modeling information such as the feeder and nodal load composition, the transformer loading ratio, the load diversity ratio, and the nodal supplied square footage requirements can be used as inputs of the load profile selection and allocation processes to give modeler flexibility for modeling different types of operation conditions. By applying this method, more realistic QSTS simulations can be conducted on different types of feeders with modeler defined settings using smart meter measurements, bridging the gap of using data collected by the advanced metering infrastructure for load allocation on distribution circuits.

4.1.2 Control of HVAC System in Commercial Building

Virtual battery is an innovative method to model flexibility of building loads and effectively coordinate them with other resources at a system level. Unlike a real battery with a dedicated power conversion system for charging control, methods are required for operating building loads to deviate from the baseline to respond to grid signals. This dissertation presents a VB control for a commercial heating, ventilation, and air conditioning system to follow the desired power consumption in real-time by adjusting zonal airflow rates.

The proposed method consists of two parts. At the system level, a mixed feedforward and feedback control is used to estimate the desired total airflow rate. At the zone level, two priority-based algorithms are then proposed to distribute the total airflow rate to individual zones. In particular, a zonal airflow limit estimation method is proposed using machine-learning techniques,

in contrast to physics-based thermal models in existing studies, to more accurately capture zonal thermal dynamics and improve temperature control performance.

An office building on the Pacific Northwest National Laboratory campus is implemented in EnergyPlus and used to illustrate and validate the proposed control. It was found that the proposed method can effectively control the HVAC system to track the desired power consumption in different use cases, while maintaining zonal temperatures within the desired range. The asymptotic allocation algorithm is more complicated but generally provides better performance in temperature control than the one-step allocation. The proposed ML-based airflow rate limit estimation outperforms popular physics-based thermal models in controlling zonal temperatures. One interesting future work is to study system impacts of controlling building loads as VBs at both distribution and transmission levels.

4.2 Vision and Plan of Future Work

The research work in the two sub-areas will be dug deeper and be advanced forward respectively. In the meantime, the feeder level study will be conducted to study when operating a number of commercial buildings in distribution feeder, how the feeder will be influenced. The synopsis of the future research plan for the sub-areas including the four existing ones and the new one is as follows:

4.2.1 Feeder Load Disaggregation Method

Previous study shows that the algorithm can model the feeder more realistic comparing with other existing strategies. The load cluster method will be researched on to allocate the houses have more similarity in one load node. The voltage comparison study when modeling the feeder with FLDA and other methods will be investigated in more detail as well. We will construct an actual case and get its time-series nodal voltage results. Then we use the feeder head load profile

of the actual case as an input, modeling the distribution system with OLSS, MLSS and FLDA. The corresponding voltage profiles will be simulated and compared with the actual case to see under each situation which method has the closest power flow result with the actual case. Our future work will also be focused on extending the load profile databases to more areas and validate the algorithm performance on more distribution systems.

4.2.2 Control of Commercial HVAC System

In the HVAC system of some commercial buildings, there will be more than one fan for each chiller, therefore, we will try to develop an updated algorithm that will work for the HVAC systems that have multiple fans. The additional fans will add complex to the existing work as the total power will be shared with different fans as well. The future work will also be focused on developing the algorithm for the heating mode of commercial HVAC system so that the grid services can be provided in winter as well. Another interesting future work is to study system impacts of controlling building loads as VBs at both distribution and transmission levels.

4.2.3 Feeder Impact of Building Demand Response

Currently, we can know which house locate at which load node in the feeder, and how to control the commercial HVAC system to consume desired power. However, at each time step which building in the feeder should provide service and the load changing of which building will benefits the feeder most have not been fully studied yet. These studies are necessary for the operation in realistic.

Therefore, the research will focus on how the feeder will be impacted when buildings in this feeder provide grid services by demand response. The method to select which building in the feeder should provide service at next time step will be studied. This will help the recruiting strategy

for electric utilities. The operation strategy for feeder in different climate zones will also be studied.

REFERENCES

- [1] J. L. Sawin, F. Sverrisson, K. Seyboth, R. Adib, H. E. Murdock, C. Lins, I. Edwards, M. Hullin, L. H. Nguyen, S. S. Prillianto et al., “Renewables 2017 global status report,” Renewable Energy Policy Network for the 21st Century, 2013.
- [2] F. Katiraei and J. R. Aguero, “Solar pv integration challenges,” *IEEE Power Energy Mag.*, vol. 9, no. 3, pp. 62–71, May 2011.
- [3] X. Zhu, J. Wang, D. Mulcahy, D. L. Lubkeman, N. Lu, N. Samaan, and R. Huang, “Voltage-load sensitivity matrix based demand response for voltage control in high solar penetration distribution feeders,” in *Proc. IEEE Power Energy Soc. Gen. Meet.*, Jul. 2017, pp. 1–5.
- [4] J. Wang, X. Zhu, D. Lubkeman, N. Lu and N. Samaan, "Continuation power flow analysis for PV integration studies at distribution feeders," 2017 IEEE Power & Energy Society Innovative Smart Grid Technologies Conference (ISGT), Washington, DC, 2017, pp. 1-5.
- [5] Wang, Jiyu. "Analysis of Voltage Problems for PV Integrated Distribution Feeder." (2016).
- [6] T. K. A. Brekken, A. Yokochi, A. von Jouanne, Z. Z. Yen, H. M. Hapke, and D. A. Halamay, “Optimal energy storage sizing and control for wind power applications,” *IEEE Trans. Sustain. Energy*, vol. 2, no. 1, pp. 69–77, Jan. 2011.
- [7] D. Wu, C. Jin, P. Balducci, and M. Kintner-Meyer, “An energy storage assessment: Using optimal control strategies to capture multiple services,” in *Proc. IEEE Power Energy Soc. Gen. Meet.*, Jul. 2015, pp. 1–5.
- [8] X. Ke, N. Lu, and C. Jin, “Control and size energy storage systems for managing energy imbalance of variable generation resources,” in *Proc. IEEE Power Energy Soc. Gen. Meet.*, Jul. 2015, pp. 1–1.

- [9] X. Zhu, J. Yan, and N. Lu, "A graphical performance-based energy storage capacity sizing method for high solar penetration residential feeders," *IEEE Trans. Smart Grid*, vol. 8, no. 1, pp. 3–12, Jan. 2017.
- [10] D. Wu, C. Jin, P. J. Balducci, and M. C. Kintner-Meyer, "Assessment of energy storage alternatives in the puget sound energy system volume 2: Energy storage evaluation tool," Pacific Northwest National Lab.(PNNL), Richland, WA (United States), Tech. Rep., 2013.
- [11] X. Ke, N. Lu, and C. Jin, "Control and size energy storage for managing energy balance of variable generation resources," in *Proc. IEEE Power Energy Soc. Gene. Meet.*, Jul. 2014, pp. 1–5.
- [12] D. Wu, M. Kintner-Meyer, T. Yang, and P. Balducci, "Economic analysis and optimal sizing for behind-the-meter battery storage," in *Proc. IEEE Power Energy Soc. Gene. Meet.*, Jul. 2016, pp. 1–5.
- [13] X. Ke, D. Wu, and N. Lu, "A real-time greedy-index dispatching policy for using pevs to provide frequency regulation service," *IEEE Trans. Smart Grid*, pp. 1–1, 2017.
- [14] "2011 Buildings Energy Data Book," <https://openei.org/doe-opendata/dataset/buildings-energy-data-book>, accessed: 2018-06-19.
- [15] U.S. Energy Information Administration. Annual energy review, 2010.
- [16] Vrettos, Evangelos, et al. "Experimental demonstration of frequency regulation by commercial buildings—Part I: Modeling and hierarchical control design." *IEEE Trans. Smart Grid*, vol. 9, no. 4, pp. 3213-3223, 2018
- [17] Oldewurtel, Frauke, et al. "Building control and storage management with dynamic tariffs for shaping demand response." In *Proc. IEEE Power Energy Soc. ISGT Europe*, 2011

- [18] IEEE P1547.7 D5.1 *Draft Guide to Conducting Distribution Impact Studies for Distributed Resource Interconnection*, IEEE Standard, Aug. 2011.
- [19] Q. Li, B. Mather, J. Deboever and M. J. Reno, "Fast QSTS for distributed PV impact studies using vector quantization and variable time-steps," *2018 IEEE Power & Energy Society Innovative Smart Grid Technologies Conference (ISGT)*, Washington, DC, 2018, pp. 1-5.
- [20] M. Kleinberg, J. Harrison, and N. Mirhosseini, "Using energy storage to mitigate PV impacts on distribution feeders," in *Proc. Power Energy Soc. Innovative Smart Grid Technologies Conference (ISGT)*, Washington, DC, USA, 2014, pp. 1-5
- [21] M.J. Reno, J. Deboever, and B. Mather, "Motivation and requirements for quasi-static time series (QSTS) for distribution system analysis," in *Proc. IEEE Power Energy Soc. Gen. Meeting*, Chicago, IL, USA, 2017 pp. 1-5.
- [22] X. Zhu, J. Wang, N. Lu, N. Samaan, R. Huang and X. Ke, "A Hierarchical VLSM-Based Demand Response Strategy for Coordinative Voltage Control Between Transmission and Distribution Systems," in *IEEE Trans. on Smart Grid*, vol. 10, no. 5, pp. 4838-4847, Sept. 2019.
- [23] Long, Qian, et al. "Volt-Var Optimization of Distribution Systems for Coordinating Utility Voltage Control with Smart Inverters." *2019 IEEE Power & Energy Society Innovative Smart Grid Technologies Conference (ISGT)*. IEEE, 2019.
- [24] Long, Qian, et al. "A New Distributed Voltage Controller for Enabling Volt-Var Support of Microgrids in Grid-Connected Operation." *2019 IEEE Power & Energy Society General Meeting (PESGM)*. IEEE, 2019.

- [25] Meng, Yao, Ming Liang, and Ning Lu. "A Cost Benefit Study of using Energy Storage to Provide Regulation Services." 2019 IEEE Power & Energy Society Innovative Smart Grid Technologies Conference (ISGT). IEEE, 2019.
- [26] McEntee, Catie, et al. "A VSM-Based DER Dispatch MINLP for Volt-VAR Control in Unbalanced Power Distribution Systems." 2019 IEEE Power & Energy Society General Meeting (PESGM). IEEE, 2019.
- [27] N. Samaan *et al.*, "Combined Transmission and Distribution Test System to Study High Penetration of Distributed Solar Generation," *2018 IEEE/PES Transmission and Distribution Conference and Exposition (T&D)*, Denver, CO, 2018, pp. 1-9.
- [28] M.J. Reno, and R.J. Broderick. "Predetermined time-step solver for rapid quasi-static time series (QSTS) of distribution systems," in Proc. IEEE Power Energy Soc. Innovative Smart Grid Technologies Conference (ISGT), Washington, DC, USA, 2017, pp. 1-5.
- [29] L. Sun, J. Thomas, S. Singh, D. Li, M. Baran, D. Lubkeman, J. DeCarolis, A. Queiroz, L. White, and S. Watts, "Cost-Benefit Assessment Challenges for a Smart Distribution System: A Case Study," in Proc. IEEE Power Energy Soc. Gen. Meeting, Chicago, IL, USA, 2017, pp. 1-5.
- [30] A. Arif, Z. Wang, J. Wang, B. Mather, H. Bashualdo and D. Zhao, "Load Modeling—A Review," in IEEE Trans. Smart Grid, vol. 9, no. 6, pp. 5986-5999, Nov. 2018.
- [31] B. Mather, "Quasi-static time-series test feeder for PV integration analysis on distribution systems," in Proc. IEEE Power Energy Soc. Gen. Meeting, San Diego, CA, USA, 2012, pp. 1-5.

- [32] X. Zhu, J. Yan, and N. Lu., "A probabilistic-based PV and energy storage sizing tool for residential loads," in Proc. IEEE Power Energy Soc. Trans. Distr. Conf., Dallas, TX, May. 2016, pp. 1-5.
- [33] N. S. Coleman and K. N. Miu, "Identification of Critical Times for Distribution System Time Series Analysis," in *IEEE Trans. Power Systems*, vol. 33, no. 2, pp. 1746-1754, March 2018.
- [34] M.H. Albadi, and E.F. El-Saadany. "Demand response in electricity markets: An overview," in Proc. IEEE Power Energy Soc. Gen. Meeting, Chicago, IL, USA, 2017 pp. 1-5.
- [35] K. Christakou, D.C. Tomozei, J.Y. Le Boudec, and M. Paolone, "GECN: Primary voltage control for active distribution networks via real-time demand-response." *IEEE Trans. Smart Grid*, vol.5, no. 2, pp. 622-631, Mar. 2014.
- [36] J. Wang, X. Zhu, D. Lubkeman, N. Lu, N. Samaan, and B. Werts, "Load aggregation methods for quasi-static power flow analysis on high PV penetration feeders," in Proc. IEEE Power Energy Soc. Trans. Distr. Conf., Denver, CO, Apr. 2018, pp. 1-5.
- [37] J. Wang, X. Zhu, D. Mulcahy, C. McEntee, D. Lubkeman, N. Lu, N. Samaan, B. Werts, and A. Kling. "A Two-Step Load Disaggregation Algorithm for Quasi-static Time-series Analysis on Actual Distribution Feeders," in Proc. IEEE Power Energy Soc. Gen. Meeting, Portland, OR, USA, 2018, pp. 1-5.
- [38] J. Yan, H. Zheng, and N. Lu. "Temperature-load sensitivity study for adjusting MISO day-ahead load forecast." 2016 IEEE Power and Energy Society General Meeting (PESGM). IEEE, 2016.
- [39] M. Liang, Y. Meng, N. Lu, D. Lubkeman and A. Kling, "HVAC load Disaggregation using Low-resolution Smart Meter Data," 2019 IEEE Power & Energy Society Innovative Smart Grid Technologies Conference (ISGT), Washington, DC, USA, 2019, pp. 1-5.

- [40] Lu, Jian, et al. "Short-term HVAC load forecasting algorithms for home energy management." 2016 IEEE Power and Energy Society General Meeting (PESGM). IEEE, 2016.
- [41] X. Ke, A. Jiang, and N. Lu. "Load profile analysis and short-term building load forecast for a university campus." 2016 IEEE Power and Energy Society General Meeting (PESGM). IEEE, 2016.
- [42] X. Zhu, and B. Mather. "Data-Driven Distribution System Load Modeling for Quasi-Static Time-Series Simulation." *IEEE Transactions on Smart Grid* (2019).
- [43] U.S. Department of Energy, "Grid energy storage," Available online at <https://www.energy.gov/sites/prod/files/2014/09/f18/Grid%20Energy%20Storage%20December%202013.pdf>, Dec. 2013, available.
- [44] F. Xie, H. Yu, Q. Long, W. Zeng and N. Lu, "Battery Model Parameterization using Manufacturer Datasheet and Field Measurement for Real-time HIL Applications," in *IEEE Transactions on Smart Grid*.
- [45] P. Mercier, R. Cherkaoui, and A. Oudalov, "Optimizing a battery energy storage system for frequency control application in an isolated power system," *IEEE Trans. Power Syst.*, vol. 24, no. 3, pp. 1469–1477, Aug.2009.
- [46] Meng, Yao, et al. "Design of Energy Storage Friendly Regulation Signals using Empirical Mode Decomposition." 2019 IEEE Power & Energy Society General Meeting (PESGM). IEEE, 2019.
- [47] S. X. Chen, H. B. Gooi, and M. Q. Wang, "Sizing of energy storage for microgrids," *IEEE Trans. Smart Grid*, vol. 3, no. 1, pp. 142–151, Mar. 2012.
- [48] G. Henri and N. Lu, "A Supervised Machine Learning Approach to Control Energy Storage Devices," in *IEEE Transactions on Smart Grid*, vol. 10, no. 6, pp. 5910-5919, Nov. 2019.

- [49] X. Ke, N. Lu, and C. Jin, "Control and size energy storage systems for managing energy imbalance of variable generation resources," *IEEE Trans. Sustain. Energy*, vol. 6, no. 1, pp. 70–78, Jan. 2015.
- [50] J. Dong, F. Gao, X. Guan, Q. Zhai and J. Wu, "Storage Sizing With Peak-Shaving Policy for Wind Farm Based on Cyclic Markov Chain Model," in *IEEE Transactions on Sustainable Energy*, vol. 8, no. 3, pp. 978-989, July 2017.
- [51] Mohammadi, Fazel, Gholam-Abbas Nazri, and Mehrdad Saif. "A Bidirectional Power Charging Control Strategy for Plug-in Hybrid Electric Vehicles." *Sustainability* 11.16 (2019): 4317.
- [52] D. Wu, N. Radhakrishnan, and S. Huang, "A hierarchical charging control of plug-in electric vehicles with simple flexibility model," *Appl. Energy*, vol. 253, p. 113490, Nov. 2019.
- [53] Huang, Sen, et al. "Transactive control design for commercial buildings to provide demand response." *IFAC-PapersOnLine* 51.34 (2019): 151-156.
- [54] Energy Information Administration, "Commercial buildings energy consumption survey," Dec. 2012.
- [55] M. Maasoumy, C. Rosenberg, A. Sangiovanni-Vincentelli, and D. S. Callaway, "Model predictive control approach to online computation of demand-side flexibility of commercial buildings HVAC systems for supply following," in *Proc. IEEE American Control Conf.*, 2014, pp. 1082–1089.
- [56] J. Ma, S. J. Qin, and T. Salsbury, "Application of economic MPC to the energy and demand minimization of a commercial building," *J Proc. Control*, vol. 24, no. 8, pp. 1282–1291, 2014.

- [57] S. C. Bengea, A. D. Kelman, F. Borrelli, R. Taylor, and S. Narayanan, "Implementation of model predictive control for an HVAC system in a mid-size commercial building," *HVAC&R Research*, vol. 20, no. 1, pp. 121–135, 2014.
- [58] G. S. Pavlak, G. P. Henze, and V. J. Cushing, "Optimizing commercial building participation in energy and ancillary service markets," *Energy Building*, vol. 81, pp. 115–126, 2014.
- [59] S. R. West, J. K. Ward, and J. Wall, "Trial results from a model predictive control and optimisation system for commercial building HVAC," *Energy Building*, vol. 72, pp. 271–279, 2014.
- [60] G. Mantovani and L. Ferrarini, "Temperature control of a commercial building with model predictive control techniques," *IEEE Trans. Ind. Electron.*, vol. 62, no. 4, pp. 2651–2660, Apr. 2015.
- [61] M. M. Olama, T. Kuruganti, J. Nutaro, and J. Dong, "Coordination and control of building HVAC systems to provide frequency regulation to the electric grid," *Energies*, vol. 11, no. 7, 2018.
- [62] H. Hao, B. M. Sanandaji, K. Poolla, and T. L. Vincent, "Aggregate flexibility of thermostatically controlled loads," *IEEE Trans. Power Syst.*, vol. 30, no. 1, pp. 189–198, Jan. 2015.
- [63] J. T. Hughes, A. D. Domínguez-García, and K. Poolla, "Virtual battery models for load flexibility from commercial buildings," in *Hawaii Int. Conf. Sys. Sci.*, Jan. 2015, pp. 2627–2635.
- [64] R. Yin, E. C. Kara, Y. Li, N. DeForest, K. Wang, T. Yong, and M. Stadler, "Quantifying flexibility of commercial and residential loads for demand response using setpoint changes," *Appl. Energy*, vol. 177, pp. 149–164, 2016.

- [65] K. Wang, R. Yin, L. Yao, J. Yao, T. Yong, and N. DeForest, "A two-layer framework for quantifying demand response flexibility at bulk supply points," *IEEE Trans. Smart Grid*, vol. 9, no. 4, pp. 3616–3627, Jul. 2018.
- [66] H. Hao, D. Wu, J. Lian, and T. Yang, "Optimal coordination of building loads and energy storage for power grid and end user services," *IEEE Trans. Smart Grid*, vol. 9, no. 5, pp. 4335–4345, Sep. 2018.
- [67] P. Zhao, G. P. Henze, S. Plamp, and V. J. Cushing, "Evaluation of commercial building HVAC systems as frequency regulation providers," *Energy Building*, vol. 67, pp. 225–235, 2013.
- [68] Y. Lin, P. Barooah, and S. P. Meyn, "Low-frequency power-grid ancillary services from commercial building HVAC systems," in *Proc. IEEE Int. Conf. Smart Grid Commun.*, Oct. 2013, pp. 169–174.
- [69] H. Hao, Y. Lin, A. Kowli, P. Barooah, and S. Meyn, "Ancillary service to the grid through control of fans in commercial building HVAC systems," *IEEE Trans. Smart Grid*, vol. 5, no. 4, pp. 2066–2074, 2014.
- [70] P. Zhao, G. P. Henze, M. J. Brandemuehl, V. J. Cushing, and S. Plamp, "Dynamic frequency regulation resources of commercial buildings through combined building system resources using a supervisory control methodology," *Energy Building*, vol. 86, pp. 137–150, Jan. 2015.
- [71] Y. Lin, P. Barooah, and J. L. Mathieu, "Ancillary services through demand scheduling and control of commercial buildings," *IEEE Trans. Power Syst.*, vol. 32, no. 1, pp. 186–197, Jan. 2017.

- [72] Y. Pan, Z. Huang, and G. Wu, "Calibrated building energy simulation and its application in a high-rise commercial building in Shanghai," *Energy Building*, vol. 39, no. 6, pp. 651–657, 2007.
- [73] Liang, Ming, et al. "Impacts of Zero Net Energy Buildings on Customer Energy Savings and Distribution System Planning." 2019 IEEE Innovative Smart Grid Technologies-Asia (ISGT Asia). IEEE, 2019.
- [74] PECANSTREET website: <https://www.pecanstreet.org/dataport/>
- [75] ASHRAE, "ASHRAE handbook fundamentals," 2017.
- [76] H. Hao, C. D. Corbin, K. Kalsi, and R. G. Pratt, "Transactive control of commercial buildings for demand response," *IEEE Trans. Power Syst.*, vol. 32, no. 1, pp. 774–783, Jan. 2017.
- [77] G. G. Moisen, "Classification and regression trees," *Encyclopedia of Ecology*, vol. 1, pp. 582–588, 2008.
- [78] Y. Ren, L. Zhang, and P. N. Suganthan, "Ensemble classification and regression-recent developments, applications and future directions [review article]," *IEEE Comput. Intell. Mag.*, vol. 11, no. 1, pp. 41–53, Feb. 2016.
- [79] X. Liang, T. Hong, and G. Q. Shen, "Occupancy data analytics and prediction: A case study," *Building Env*, vol. 102, pp. 179 – 192, 2016.
- [80] F. Mohammadi and C. Zheng, "A precise SVM classification model for predictions with missing data," in *Proc. 4th National Conf. Applied Research Elec. Mech. Comp. IT Eng.*, Tehran, Iran, 2018.
- [81] ———, "The ASHRAE handbook HVAC systems and equipment (SI Edition)," 2008.
- [82] Department of Energy, "EnergyPlus engineering reference," 2010. [Online]. Available: <https://energyplus.net/sites/default/files/pdfs v8.3. 0/EngineeringReference.pdf>

- [83] N. Radhakrishnan, Y. Su, R. Su, and K. Poolla, "Token based scheduling for energy management in building HVAC systems," *Appl. Energy*, vol. 173, pp. 67–79, 2016.
- [84] P. Li, Y. Li, and J. E. Seem, "Efficient operation of air-side economizer using extremum seeking control," *J. Dyn. Sys. Measure. Control*, vol. 132, no. 3, p. 031009, 2010.
- [85] T. Lu, X. Lu," and M. Viljanen, "A novel and dynamic demand-controlled ventilation strategy for CO₂ control and energy saving in buildings," *Energy Building*, vol. 43, no. 9, pp. 2499–2508, 2011.
- [86] M. Wetter, P. Haves, and B. Coffey, "Building controls virtual test bed," Lawrence Berkeley National Laboratory, Tech. Rep., 2008.
- [87] Jiyu Wang, Sen Huang, Di Wu and Ning Lu, "A Data-driven Control Method for Operating the Commercial HVAC Load as a Virtual Battery." 2019 IEEE Power & Energy Society General Meeting (PESGM). IEEE, 2019.
- [88] G. Gan, "Effective depth of fresh air distribution in rooms with single-sided natural ventilation," *ENERG. BUILDINGS*, vol. 31, no. 1, pp. 65–73, 2000. [Online]. Available: <http://www.sciencedirect.com/science/article/pii/S0378778899000067>
- [89] S. Huang, and D. Wu. "Validation on aggregate flexibility from residential air conditioning systems for building-to-grid integration." *Energy and Buildings* 200 (2019): 58-67.
- [90] H. O. R. Howlader, M. M. Sediqi, A. M. Ibrahim and T. Senjyu, "Optimal Thermal Unit Commitment for Solving Duck Curve Problem by Introducing CSP, PSH and Demand Response," *IEEE Access*, vol. 6, pp. 4834-4844, 2018.
- [91] Q. Hou, N. Zhang, E. Du, M. Miao, F. Peng and C. Kang, " Probabilistic duck curve in high PV penetration power system: Concept, modeling, and empirical analysis in China,," *Applied Energy*, vol. 242, pp. 205-215, 2019.

- [92] H. O. R. Howlader, M. Furukakoi, H. Matayoshi and T. Senjyu, "Duck curve problem solving strategies with thermal unit commitment by introducing pumped storage hydroelectricity & renewable energy," 2017 IEEE 12th International Conference on Power Electronics and Drive Systems (PEDS), Honolulu, HI, pp. 502-506, 2017 doi: 10.1109/PEDS.2017.8289132.
- [93] Q. Wang, P. Chang, R. Bai, W. Liu, J. Dai, and Y. Tang, "Mitigation Strategy for Duck Curve in High Photovoltaic Penetration Power System Using Concentrating Solar Power Station," *Energies*, 12(18), 3521, 2019.
- [94] R. Torabi, A. Gomes and F. Morgado-Dias, "The Duck Curve Characteristic and Storage Requirements for Greening the Island of Porto Santo," 2018 Energy and Sustainability for Small Developing Economies (ES2DE), Funchal, 2018, pp. 1-7, doi: 10.1109/ES2DE.2018.8494235.
- [95] Q. Nguyen, H. V. Padullaparti, K. Lao, S. Santoso, X. Ke and N. Samaan, "Exact Optimal Power Dispatch in Unbalanced Distribution Systems With High PV Penetration," in *IEEE Transactions on Power Systems*, vol. 34, no. 1, pp. 718-728, Jan. 2019.
- [96] X. Zhu, G. Henri, J. Yan and N. Lu, "A cost-benefit study of sizing residential PV and ES systems based on synthesized load profiles," 2017 IEEE Power & Energy Society General Meeting, Chicago, IL, 2017, pp. 1-5.
- [97] California ISO, "Fast facts," <https://www.caiso.com/Documents/FlexibleResourcesHelpRenewablesFastFacts.pdf>, 2018.
- [98] M. A. Ghasemi, H. M. Foroushani and M. Parniani, "Partial Shading Detection and Smooth Maximum Power Point Tracking of PV Arrays Under PSC," in *IEEE Transactions on Power Electronics*, vol. 31, no. 9, pp. 6281-6292, Sept. 2016, doi: 10.1109/TPEL.2015.2504515.

- [99] X. Li, Y. Li, X. Han and D. Hui, " Application of Fuzzy Wavelet Transform to Smooth Wind/PV Hybrid Power System Output with Battery Energy Storage System," in *Energy Procedia*, vol. 12, pp. 994-1001, 2011.
- [100] A. Mammoli, A. Ellis, A. Menicucci, S. Willard, T. Caudell and J. Simmins, "Low-cost solar micro-forecasts for PV smoothing," 2013 1st IEEE Conference on Technologies for Sustainability (SusTech), Portland, OR, 2013, pp. 238-243, doi: 10.1109/SusTech.2013.6617327.
- [101] A. Ellis, D. Schoenwald, J. Hawkins, S. Willard and B. Arellano, "PV output smoothing with energy storage," 2012 38th IEEE Photovoltaic Specialists Conference, Austin, TX, 2012, pp. 001523-001528, doi: 10.1109/PVSC.2012.6317885.
- [102] X. Li, D. Hui and X. Lai, "Battery Energy Storage Station (BESS)-Based Smoothing Control of Photovoltaic (PV) and Wind Power Generation Fluctuations," in *IEEE Transactions on Sustainable Energy*, vol. 4, no. 2, pp. 464-473, April 2013, doi: 10.1109/TSTE.2013.2247428.
- [103] G. Wang, M. Ciobotaru and V. G. Agelidis, "Power Smoothing of Large Solar PV Plant Using Hybrid Energy Storage," in *IEEE Transactions on Sustainable Energy*, vol. 5, no. 3, pp. 834-842, July 2014, doi: 10.1109/TSTE.2014.2305433.
- [104] R. K. Lam and Hen-Geul Yeh, "PV ramp limiting controls with adaptive smoothing filter through a battery energy storage system," 2014 IEEE Green Energy and Systems Conference (IGESC), Long Beach, CA, 2014, pp. 55-60, doi: 10.1109/IGESC.2014.7018640.
- [105] S. J. Hossain, B. D. Biswas, R. Bhattarai, M. Ahmed, S. Abdelrazek and S. Kamalasan, "Operational Value-Based Energy Storage Management for Photovoltaic (PV) Integrated Active Power Distribution Systems," in *IEEE Transactions on Industry Applications*, vol. 55, no. 5, pp. 5320-5330, Sept.-Oct. 2019, doi: 10.1109/TIA.2019.2920229.

- [106] M. Lei, Z. Yang, Y. Wang, H. Xu, L. Meng, J. Vasquez and J. Guerrero, "An MPC-Based ESS Control Method for PV Power Smoothing Applications," in *IEEE Transactions on Power Electronics*, vol. 33, no. 3, pp. 2136-2144, March 2018, doi: 10.1109/TPEL.2017.2694448.
- [107] P. Li, R. Dargaville, Y. Cao, D. Li and J. Xia, "Storage Aided System Property Enhancing and Hybrid Robust Smoothing for Large-Scale PV Systems," in *IEEE Transactions on Smart Grid*, vol. 8, no. 6, pp. 2871-2879, Nov. 2017, doi: 10.1109/TSG.2016.2611595.
- [108] S. G. Solanki, V. K. Ramachandaramurthy, N. Y. K. Shing, R. H. G. Tan, M. Tariq and S. B. Thanikanti, "Power smoothing techniques to mitigate solar intermittency," 2019 International Conference on Electrical, Electronics and Computer Engineering (UPCON), ALIGARH, India, 2019, pp. 1-6, doi: 10.1109/UPCON47278.2019.8980080.
- [109] L. Chen, J. Wang, Z. Sun, T. Huang and F. Wu, "Smoothing Photovoltaic Power Fluctuations for Cascade Hydro-PV-Pumped Storage Generation System Based on a Fuzzy CEEMDAN," in *IEEE Access*, vol. 7, pp. 172718-172727, 2019, doi: 10.1109/ACCESS.2019.2955569.
- [110] R. Kini, D. Raker, T. Stuart, R. Ellingson, M. Heben and R. Khanna, "Mitigation of PV Variability using Adaptive Moving Average Control," in *IEEE Transactions on Sustainable Energy*, doi: 10.1109/TSTE.2019.2953643.
- [111] W. Yu-fei, L. Meng-meng, X. Hua and L. Chang-shi, "PV power smoothing in regional grid based on self-adaption wavelet packet decomposition," 2017 IEEE Conference on Energy Internet and Energy System Integration (EI2), Beijing, 2017, pp. 1-6, doi: 10.1109/EI2.2017.8245250.

- [112] W. Kreeumporn and I. Ngamroo, "Optimal Superconducting Coil Integrated Into PV Generators for Smoothing Power and Regulating Voltage in Distribution System With PHEVs," in *IEEE Transactions on Applied Superconductivity*, vol. 26, no. 7, pp. 1-5, Oct. 2016, Art no. 5402805, doi: 10.1109/TASC.2016.2591981.
- [113] L. Yang, G. Song, S. Wenhui, H. Guoqing and W. ZhengPing, "Integrated control strategy for smooth switching of the PV and battery-storage micro-grid based on operation state tracking," in *The Journal of Engineering*, vol. 2019, no. 16, pp. 1062-1067, 3 2019, doi: 10.1049/joe.2018.8877.
- [114] D. Zhang, J. Guo and J. Li, "Coordinated control strategy of hybrid energy storage to improve accommodating ability of PV," in *The Journal of Engineering*, vol. 2017, no. 13, pp. 1555-1559, 2017, doi: 10.1049/joe.2017.0592.
- [115] M. J. Reno, M. Lave, J. E. Quiroz and R. J. Broderick, "PV ramp rate smoothing using energy storage to mitigate increased voltage regulator tapping," 2016 IEEE 43rd Photovoltaic Specialists Conference (PVSC), Portland, OR, 2016, pp. 2015-2020, doi: 10.1109/PVSC.2016.7749982.
- [116] J. Wang, S. Huang, D. Wu and N. Lu, "Operating a Commercial Building HVAC Load as a Virtual Battery through Airflow Control," in *IEEE Transactions on Sustainable Energy*, doi: 10.1109/TSTE.2020.2988513.